July 2018

ENGINEERING NEXT GENERATION ANISOTROPIC MATERIALS AND COMPOSITES

Nihal Kanbargi

ENGINEERING NEXT GENERATION ANISOTROPIC MATERIALS AND COMPOSITES

A Dissertation Presented

By

NIHAL KANBARGI

Submitted to the Graduate School of the
University of Massachusetts Amherst in partial fulfillment
of the requirements for the degree of

DOCTOR OF PHILOSOPHY

May 2018

Polymer Science & Engineering

ENGINEERING NEXT GENERATION ANISOTROPIC MATERIALS AND COMPOSITES

A Dissertation Presented
by
NIHAL KANBARGI

Approved as to style and content by:

_____
Alan J. Lesser, Chair

_____
David A. Hoagland, Member

_____
H. Henning Winter, Member

_____
Weiguo Hu, Member

_____

Bryan Coughlin, Department Head,
Polymer Science and Engineering

ACKNOWLEDGEMENTS

While looking up profiles of professors at UMass, Amherst, the one that struck me the most was Professor Alan Lesser's. Not only did he resemble Daniel Craig in appearance, he also worked on polymer composites and mechanics, a field I was very much interested in. On arriving here at UMass, my first interaction with him was when he came to class without any notes, equipped with only a chalk and wrote down all the tensorial continuum mechanics equations on the board. Since then, I had made up my mind on whom I wanted as my advisor. I am full of gratitude for all the help and advice I have received from him all through these years. There were times when he was tough, but I always knew that it was to bring out the best in me. Despite suffering from tremendous pain recently due to a health emergency, he was full of life and energy. I remember a time he corrected my paper in between two sessions of artificially induced coma, which is just one example of his magnificent work ethic. He embodies perfectly the Indian philosophy of Karma Yoga; perform your duty, without any attachment to the results. I am eternally grateful to him for molding me into a better scientist and a better person. Thank you, Professor Lesser!

Also, I am very grateful to my committee members Dr. Weiguo Hu, Dr. David Hoagland and Dr. Henning Winter. Weiguo has almost been like my second advisor, guiding me on the Solid-State NMR project. He would always encourage me to probe deeper and ask more questions, advice which not only applies to science but to life in general. Dr. David Hoagland's knowledge in polymer science is not only broad but also deep. I appreciate his prompt nature in addressing everything from scheduling to recommendation letters. Prof. Henning Winter's kind and supportive nature struck me as particularly helpful.

Group members past and present, everyone made me feel that I couldn't have chosen a better group. Angela, Henry, Ranadip, Brian, Polina, Connor, Silas, Madhura, Matt, Amy, Brendan, Daniel, Chinmay, and Liz were talented group mates. I am particularly grateful to my seniors Ranadip, Henry, Angela, Polina, Connor, and Brian for their support and advice through my early years of the Ph.D., when the sailing was not always smooth. I have enjoyed the company of many officemates through the years, all providing entertainment as well as being a sounding board for my ideas and complaints. I would like to mention Marco Van Erp, who I enjoyed mentoring and being a friend.

I am very thankful for the PSE Class of 2012; I have enjoyed a special connection with each one of you. I would like to also thank all our German students, who were helpful in softening the 'cultural shock' in the first few months of being in Amherst.

PSE Staff: Alex Ribbe, Sekar, Lisa, Maria, Jessica.

To my roommates Mike, Joel and Nakul, we have created bonds for a lifetime. Other friends who have been a great support throughout my Ph.D.: Satyan, Ishan, Ashutosh, Rohit Gupta, Adam Hauser and almost everyone from the class of 2011. Playing in a graduate student band was a dream come true for me. Friends from back home: Atul (both), Prabhat, Sriket, Pushkar, Sameer, Lokesh and friends from school: Ananth, Vijayendra, Girish, Shrinivas, Himanshu.

And lastly and most importantly, my parents whose annoying persistence made all this possible.

ABSTRACT

ENGINEERING NEXT GENERATION ANISOTROPIC MATERIALS AND COMPOSITES

MAY 2018

NIHAL KANBARGI,

INTEGRATED M. TECH, INDIAN INSTITUTE OF TECHNOLOGY ROORKEE

Ph.D., UNIVERSITY OF MASSACHUSETTS AMHERST

Directed by: Professor Alan J. Lesser

Polymer-based composite systems have been developed for a wide variety of applications ranging from aerospace to electronics. My work has focused on the structure-process-property relationships of anisotropic polymeric materials and composites, aimed primarily for structural applications. Anisotropic materials such as fibers have superior mechanical properties along the axial direction and this property can be exploited to engineer exceptionally strong and light materials. In the first chapter, we discuss the physics of degradation of Poly(p-phenylene-2,6-benzobisoxazole) (PBO) fibers. PBO, a fiber of extraordinary tensile modulus and strength has been found to degrade rapidly under moderate conditions of humidity and heat. Solid-state NMR was utilized as a screening tool to study the long-term aging performance of these fibers under systematic exposure to environmental conditions. Many studies have suggested that the likely mechanism of the degradation of the fibers is due to opening and cleaving of the oxazole bond due to the residual phosphoric acid entrapped within the fiber during the dry-jet wet spinning manufacturing process. However, there has been no direct study of the chemical structure

and physical state of the residual phosphorous (P) in the fiber. In this chapter, we investigate the chemical structure and physical state of the residual P in PBO fiber using solid-state 31P nuclear magnetic resonance (ssNMR) spectroscopy. The residual P is found to exist mainly in the form of phosphoric acid (PA) and it's various hydrated or dehydrated derivatives. Moisture was found to drive the reaction along the direction of phosphorous anhydride / polyphosphoric acid / PA / hydrated PA while increasing the temperature in the absence of moisture reverses this direction. Hydration increases the mobility of PA molecules and its ability to migrate, thus promoting hydrolytic degradation, while higher a temperature in the absence of moisture removes water and immobilizes PA. The residual P species likely reside on the surface of the nanovoids in the PBO fiber, easily accessed by gaseous water molecules but inaccessible to aqueous media. These studies provide direct evidence to confirm the proposed contribution of the residual P to the hydrolytic degradation mechanisms reported in the literature. Further, ssNMR may play a role in assessing future strategies mitigating this crippling problem for PBO fiber, which would otherwise be an excellent choice for soft body armor applications.

In the second chapter, we discuss new methods to improve composite strength by modifying the critical fiber-matrix interphase to improve fiber-matrix adhesion. The work described here is based on an aramid fiber (poly (paraphenylene terephthalamide))and natural rubber matrix system, however this approach is universal and should be applicable to any composite system. Fiber pre-treatments are applied to create new morphologies on the fiber surface to enable enhanced mechanical interlocking between the fiber and rubber matrix. The pretreated fibers are then exposed to treatments with coupling agents in the presence of supercritical carbon dioxide ($scCO_2$) in an attempt to permeate the fiber surface

and create an interphase region with a gradient in properties from the fiber to the matrix. Shear lag analysis using a Kelly Tyson approach is compared to more refined models to evaluate optimum test parameters for fiber pull-out adhesion tests. The results show that the adhesion increases by approximately 100% when compared to conventional composites. Failure analysis of the fiber surface reveals a suppression of interfacial failure. The effects of pretreatments on fiber properties are also characterized, and the optimization of fiber properties, fiber-matrix interface properties, and overall composite properties are discussed.

In the third chapter, a method to template kinetically trapped composite foams from anisotropic semi-crystalline media is presented. The semi-crystalline polymer templates are films (polyethylene terephthalate) and filaments (polyamide-12) that are respectively biaxially and uniaxially oriented. Supercritical carbon dioxide ($ScCO_2$) was used as a solvent to transport styrene monomer mixed with a radical initiator into the template. This phase was allowed to polymerize and foam to create a microcellular structure. Though the anisotropy in the template was found not to dictate the final morphology of cells, interesting cell structures such as a radial gradient and a sheet-like structure were observed due to the processing conditions. Initial mechanical tests showed an improvement in specific modulus and specific strength. This approach might be utilized to create composite foams with tunable macroscopic and microscopic features that could be potentially mimic balsa wood. Utilizing novel additives such as surfactants in synergy with $scCO_2$ to process polyolefins are also explored, which cannot be processed with superheated water due to their polarity. Finally, processing thin film elastomeric foams from polymers such as SBS block copolymers with $scCO_2$ is explored.

TABLE OF CONTENTS

Page

LIST OF TABLES

Table Page

LIST OF FIGURES

CHAPTER 1

INTRODUCTION

Anisotropic materials and composites are ubiquitous in nature and manufactured by man for a variety of applications such as automobiles, aerospace and load-bearing structures. A composite usually consists of at least two components, a stiffer load-bearing component and a matrix with lower stiffness. The stiffer component is often anisotropic in nature, such as fibers either in long or short form. For example, natural composites such as wood are made of anisotropic crystalline cellulose as the reinforcing component and the softer lignin as the binding matrix. In man-made systems, high-performance polymeric fibers are often incorporated as the reinforcing component for demanding applications such as aerospace. A critical but often ignored part of a composite system is the interphase region, a region that extends beyond the interface to include both fiber and matrix, but with differing properties from either. Optimum interphase properties are critical in deciding the strength of composites. This work broadly addressed the new routes to characterize and improve the performance of composites by addressing each major component i.e. the fiber, the fiber-matrix interphase, and the bulk matrix.

The first chapter deals with one of the strongest high-performance fibers known to man: poly(*p*-phenylene-2,6-benzobisoxazole) (PBO). High-performance fibers differ from commodity polymeric fibers in such that their tenacity and modulus exceed those of conventional fibers by at least an order of magnitude. A variety of attributes make a fiber 'high performance', such as the chemical structure, the extent of anisotropy and crystallinity. Fibers such as poly-paraphenylene terephthalamide (PPTA) or poly(*p*-phenylene-2,6-benzobisoxazole) (PBO) have a rigid chemical backbone with a highly

conjugated aromatic structure and crystallinity exceeding 95%, which result in a specific tenacity and modulus that much exceed that of steel fibers. First, we delve into the fundamental question of how the chemical structure and morphology of high-performance fibers such as PBO lead to its unique mechanical properties and an investigation into how the processing technique leads to a fundamental flaw in the fiber. PBO fibers freshly spun, are one of the strongest fibers known to man. However, the strength of these fibers is known to drop rapidly under moderate conditions of humidity and heat. PBO fibers are usually synthesized with polyphosphoric acid (PPA) as the solvent [1–5] using a technique known as dry-jet wet spinning (Figure 1). PPA plays multiple roles, as a solvent, a catalyst, and a dehydrating agent[6]. Since these polymer chains have a rigid rod character, they form oriented liquid crystalline structures in solution, which translates to high anisotropy when spun.

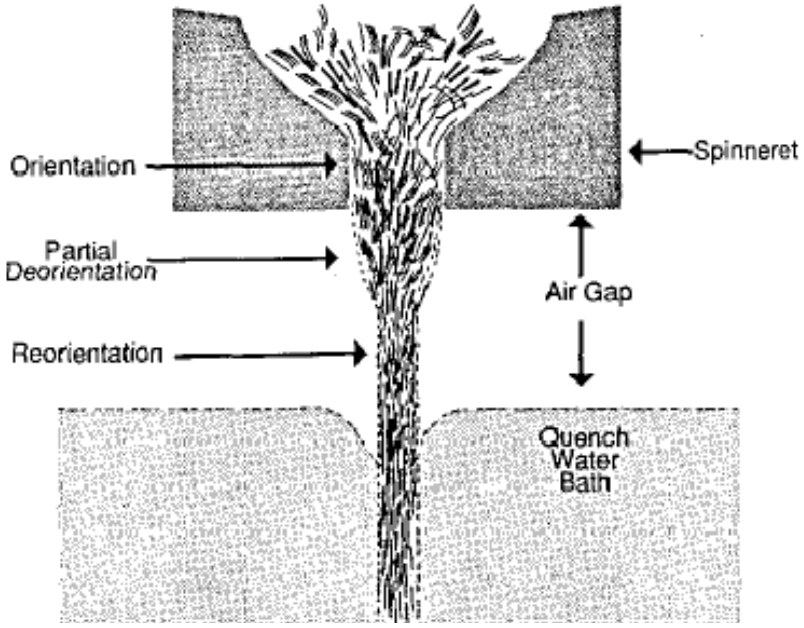

Figure 1. Dry Jet Wet Spinning method

The resulting fiber has a microfibrillar[7–10] structure with voids present between these fibrils. These voids can entrap phosphorus compounds that cannot be washed away during conventional processing of the fiber. It has been speculated that these entrapped compounds cause premature degradation of the fiber, especially in hot and humid conditions. Even conditions such as those experienced by human bodies in real-world service conditions were found to degrade the fibers quite rapidly. Our investigation examined the role of the entrapped phosphorus compounds in the rapid degradation of the fibers. Solid-state NMR was proposed as a novel technique to investigate the process of hydrolytic degradation of the fibers and propose a mechanism that could explain the rapid loss of tenacity under humid conditions. The study aimed to measure how the moisture changed the phase and chemical nature of the entrapped phosphorus compounds. Performing ^{31}P ssNMR has the added advantage of high sensitivity since the nuclei have 100% natural abundance. Also, the technique is nondestructive in nature. Finally, solutions to mitigate this problem were proposed based on the results obtained from this technique.

In the second chapter, we investigate if the presence of the aforementioned voids in aramid fibers could be exploited to improve the performance of long fiber composites by targeting the 'interphase region'. PPTA aramid fibers are known for their exceptionally high tensile strength and hence are found in a wide variety of high-performance applications ranging from military to aerospace and civil applications. The performance of such high-performance composites is not only governed by the strength of the reinforcing fiber but also the effectiveness of load transfer from matrix to the fiber. Fiber-matrix interfacial adhesion becomes critical here in deciding the strength of a composite. Studies have revealed that there is an *interphase*[11] region that governs properties of the composite.

This interphase not only includes the interface but extends some distance into the fiber and the matrix. The aim of this project was to find an effective way to improve composite properties by modifying the interphase region and improving the adhesion of the fiber to the matrix. In this chapter, we present new methods to improve the adhesion between PPTA fibers and a natural rubber matrix for tire reinforcement. Fiber pre-treatments that exploit the presence of sub-surface voids are presented to create new surface morphologies on the fiber that enable enhanced adhesion between the fiber and matrix. The pre-treated fibers are then subject to treatments with coupling agents in the presence of supercritical carbon dioxide ($scCO_2$) in an attempt to permeate the fiber surface. Shear lag analysis using a Kelly Tyson approach is compared to more refined models to evaluate optimum test parameters for fiber pull-out adhesion tests. Adhesion tests are carried out and results are discussed.

In the third chapter, we move to less crystalline films and fibers, which are anisotropic to a lesser extent. The motivation for this project was to create a synthetic replacement for a natural structural material, balsa wood. Natural cellular materials such as balsa wood have very high specific strength and modulus. The cells of balsa wood are

long, slender and highly elongated (Figure 2) in the axial direction of the wood, giving it anisotropic mechanical properties.

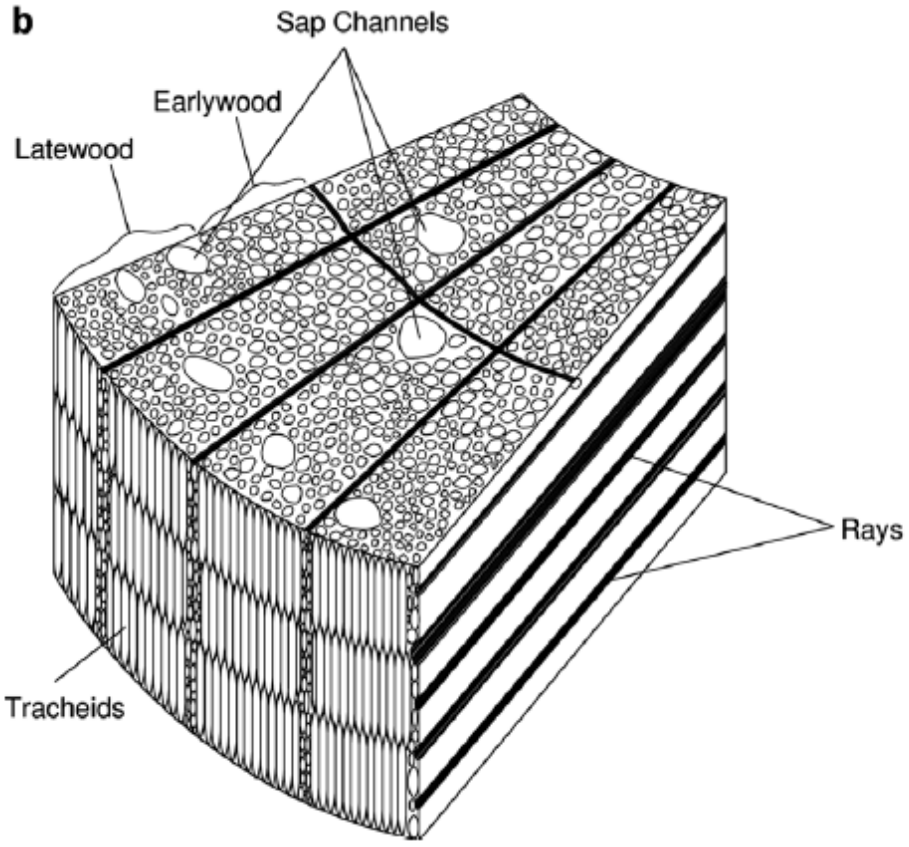

Figure 2. The microstructure of Balsa Wood. (Da Silva, Andre, and Stelios Kyriakides. "Compressive response and failure of balsa wood." International Journal of Solids and Structures (2007).

Also, the wood itself is a composite of semi-crystalline cellulose (primary strength provider), hemicellulose and amorphous lignin. To create a synthetic foam with comparable properties, one would have to incorporate crystalline materials in the foam in order to come close to achieving the high strength of balsa. However, most semi-crystalline materials are inherently difficult to foam[12–14]. The issue probed in this research was to ascertain if the inherent molecular anisotropy in a semi-crystalline substrate plays a role or

dictates the final morphology of cells in a composite foamed with that substrate. Using a semi-crystalline anisotropic component as a template to influence the cell nucleation and growth, the final morphology of cells in the amorphous component of a two-component system may be governed to some extent by the anisotropy of the film or filament system being used as the template. We attempted to synthesize anisotropic cellular materials that mimic balsa by using the inherent anisotropy of crystals in systems such as films and filaments. For this reason, two anisotropic templates were chosen, a uniaxially oriented polyamide-12 (PA12) filament and a biaxially oriented polyethylene terephthalate (PET) film. Kinetically trapped composites were created by this technique and their compositions and properties studied.

CHAPTER 2

DEGRADATION MECHANISM OF HIGH-PERFORMANCE POLY(P-PHENYLENE-2,6-BENZOBISOXAZOLE) (PBO) FIBERS USING SOLID STATE NUCLEAR MAGNETIC RESONANCE

2.1. Introduction

Poly(*p*-phenylene-2,6-benzobisoxazole) (PBO) is an engineering fiber of extraordinary properties. Freshly prepared PBO fibers have superior stiffness and strength[16] compared to poly (*p*-paraphenylene terephthalamide)(PPTA) fibers[17] and therefore have been sought as a major improvement for soft body armor applications. The highly aromatic nature and conjugated structure of the benzobisoxazole and phenyl rings in the backbone of the molecule contribute to a high level of electron delocalization, imparting high rigidity and rod-like character to the backbone[18–20]. This translates to exceptionally high modulus and tensile strength that exceed PPTA fibers. However, a rapid drop in tensile strength was observed when fibers were exposed to moderate levels of moisture and heat[21–23]. Even conditions such as those experienced by human bodies in real-world service conditions were found to degrade the fibers quite rapidly.

PBO fibers are usually synthesized from terephthalic acid and diaminodihydroxybenzene dihydrochloride (DADHB) or 2,5-diamino-1,3-benzenediol (DABDO) in polyphosphoric acid (PPA)[1–5]. A dry-jet wet spinning process is used where the polymer solution in PPA is passed through a spinneret into a coagulation bath (usually water). PPA plays multiple roles, as a solvent, a catalyst, and a dehydrating agent[6]. Since the polymer chains have a rigid rod character, they form oriented liquid crystalline structures in solution, which translates to high anisotropy when spun. An air gap is used to add further anisotropy into the system[24]. The resulting fiber has a microfibrillar[7–10]

structure with voids present between these fibrils. These voids can entrap phosphorus compounds that cannot be washed away during conventional processing of the fiber.

The mechanisms for this rapid degradation have been extensively studied. Work on fibers and model compounds have shown that PBO molecules are susceptible to hydrolytic degradation[25–28], especially in acidic conditions. Jackson and coworkers[26] studied model systems and observed that the peak rates for the hydrolysis of the benzoxazole bond were obtained at a pH of around 1. Attempts to access the residual compounds with bases like pyridine caused further degradation of fiber mechanical properties[29,30], indicating that hydrolytic degradation could occur under basic conditions as well. Chin and coworkers[23] reported findings with fibers extracted from bulletproof vests exposed to humidity and heat using FTIR and found that there was a decrease of the benzoxazole group signal and an increase of the carboxylic signal with time, indicating the onset of hydrolysis. Humidity seems to be playing a key role here since hot conditions in the absence of humidity have proved to be not as detrimental[23]. The exact physical state and chemical composition of the phosphorus (P) compounds have also been the subject of debate. The residual P could be phosphate groups that are chemically bound at the chain ends as shown by a model compound study[1,21] or residual phosphoric acid (PA) which might exist in the nanovoids of the fiber[31]. The acidic nature of the residual P compounds could be one of the reasons for the premature degradation of these fibers. However, there has been no direct study of the structure and behaviors of the residual P species, thus "there is little direct evidence that PA exists in PBO fibers" [21].

In this chapter, the chemical structure and physical state of the residual P species are studied using ^{31}P ssNMR and an attempt made to correlate them to the observed

hydrolytic degradation of the fiber. Using ^{31}P ssNMR to study the residual P has several unique advantages. First, like liquids NMR, ssNMR is capable of probing the chemical structure of the P species. Second, it can also detect their physical properties (e.g. liquid vs solid), which play a crucial role in their chemical activities. Third, the NMR-active isotope of P, ^{31}P, is at 100% natural abundance and has a high gyromagnetic ratio. These traits mean that the P species give high NMR signal strength, enabling detection of low levels of P in the fiber. Fourth, NMR is a non-invasive technique, so the P species do not need to be extracted to be studied. Finally, as the fiber matrix is free of phosphorous, the ^{31}P ssNMR spectra of the fiber contain only signals from the residual P species, without any complication from the much more populous fiber matrix. First, the presence of P and its relaxation behaviors are probed by conducting several simple ssNMR experiments, including ^{31}P DP/MAS, CP/MAS, and CP/T_1 experiments. Preliminary assignment of the signals was performed based on their chemical shifts and relaxation properties. Subsequently, aging of the fibers both in humidity and in a dry environment at elevated temperatures was carried out, and the chemical structure and physical mobility of the P compound under these conditions were studied. Next, kinetic studies were performed by studying the ^{31}P signal of the fibers exposed to humidity for various amounts of time. Finally, a possible route to mitigate this problem was suggested and its effect on the mechanical properties discussed.

2.2. Materials and Methods

PBO fiber yarn (1640 Dtex/1500 denier; 996 filaments) was purchased from C.S.R. Inc. (Sellersville, PA) and sealed in an ultraviolet radiation resistant bag. An airtight desiccator was used to store the bag and anhydrous calcium sulfate desiccant was placed on the bottom

of the desiccator to keep the environment free from moisture. Phosphoric acid (PA), phosphorus pentoxide, polyphosphoric acid (PPA), and ammonium dihydrogen phosphate ($NH_4H_2PO_4$, or ADP) were obtained from Sigma Aldrich and used as is. A saturated salt solution of potassium sulfate[32] was used to maintain an equilibrium humidity of 96% at a temperature of 40°C for the aging experiments. For this experiment, fibers were placed in an airtight desiccator with a beaker of salt solution placed in it. The large thermal mass of this system ensured minimal temperature fluctuations. This particular temperature of 40°C was chosen to mimic the temperature of the human body. For the dry heat treatment, fibers were placed in a dry furnace at elevated temperatures for varying durations of time. Anhydrous ammonia gas of 99.9% purity was obtained from Airgas and used as is. Immersion in ammonia gas was performed in custom-built high-pressure reactors. Fibers were placed in a test tube and inserted into high-pressure cylindrical reactor where they were treated with ammonia gas at pressures of 70 psi for varying durations. They were subsequently taken out and used immediately for testing.

The mechanical strength of the fibers was measured by fiber yarn tensile tests on an Instron 5500 tensile testing machine. Special pneumatic fiber grips were used for this purpose. The fiber yarn was carefully twisted to 150 turns per meter. The twisted yarns were cut into bundles of 50cm in length and placed between the pneumatic grips to give a gauge length of 30cm, particular care being taken to ensure the fiber yarns stay twisted. The fibers bundles were pulled at a rate of 5mm/min until failure. A minimum of four bundles were tested for each condition.

NMR experiments were performed using a Bruker 600MHz solid-state NMR spectrometer in a 4mm broadband-observe CP/MAS Probe. Small sections of cut PBO

fibers were crumbled into small balls and packed into 4mm rotors. Care was taken to place the sample in the center of the rotor, with both the bottom and top 4mm length filled with polytetrafluoroethylene (PTFE) tape. The %P calibration standard, ADP, was also packed in the same position in a 4mm rotor. Three NMR pulse sequences were used to probe the properties of the fiber: (1) Direct Polarization (DP/MAS), which directly excites ^{31}P signal. (2) Cross Polarization (CP/MAS), which excites ^{1}H signal first, then transfers to nearby ^{31}P through dipolar interaction. Recycle delay was 6 s. (3) CP/T_1 experiment[33], in which, after cross polarization, ^{31}P magnetization is transferred to the ±z axes alternately, followed by a duration τ which causes the magnetization to decay to zero at sufficiently long τ, and finally a read-out 90° pulse. The pulse sequences are shown in Figure 3. Recycle delay was 12 s. ^{31}P chemical shift was calibrated using 85% PA at 0 ppm or ADP at 1.07ppm.

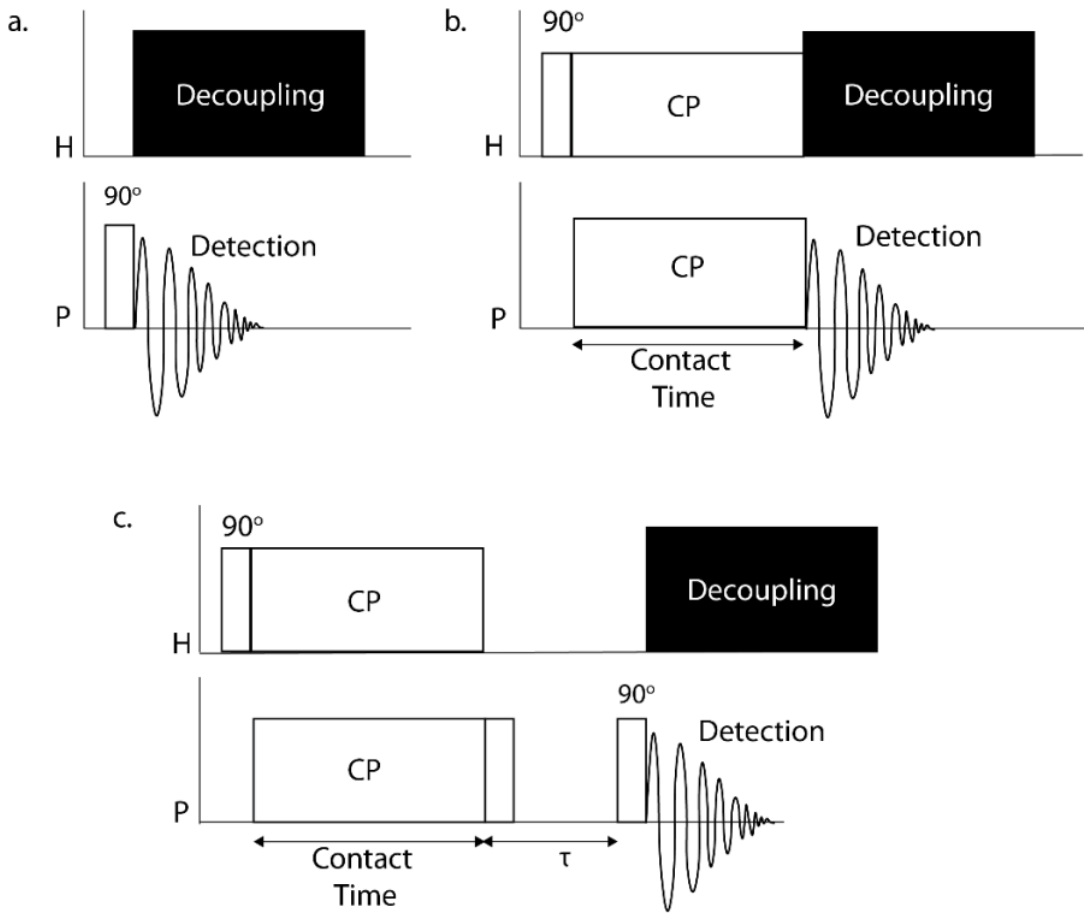

Figure 3. Pulse sequences used in the present report: a) DP/MAS experiment, b) CP/MAS experiment and c) CP/T_1 experiment with wait time τ.

2.3. Results and Discussion

2.3.1. 31P ssNMR of as-received PBO fibers.

In this section, the chemical structure and the magnetic relaxation properties of the P species in the fiber were investigated. A series of ^{31}P DP/MAS spectra of as-received PBO fiber were acquired with various recycle delays (RD) in order to probe the ^{31}P T_1 relaxation characteristics of the P species in the fiber. Figure 4 shows two of the spectra, with RD = 6 s and 300 s. Both spectra have a tall peak centered at ca. 3.0 ppm, along with several spinning sidebands (SSB). Assignment of SSBs in all the experiments in the present report was done by simply spinning the samples at different speeds and observing the shifting of the peaks with regard to each other.

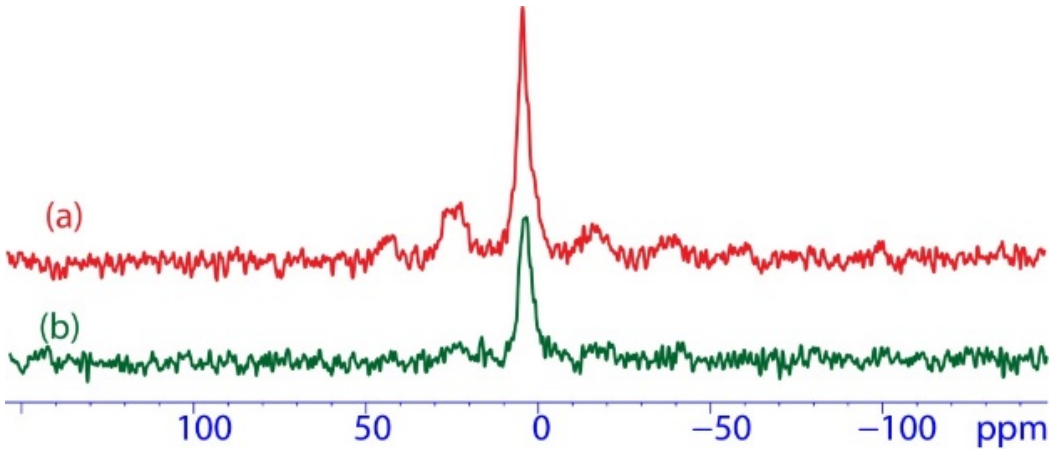

Figure 4. ^{31}P DP/MAS spectra of as-received PBO fiber at RD of (a) 300s and (b) 6 s.

The spectrum at RD = 6 s has very little SSB, while the spectrum at RD = 300 s has both a taller center band and much more intense SSBs. ^{31}P signals span a wide chemical shift range, from -180 ppm to 350 ppm for common P compounds. Peaks appearing between -5 and 5 ppm are usually PA or phosphates. Therefore, the signal for the P species inside the fiber is most likely PA or its phosphate derivatives. PA could be formed by moisture

hydrolysis of PPA, which is trapped inside the fiber during the spinning process. Model compound studies[1] indicated that phosphate may also exist as the end groups of the PBO chains. Upon exposure to moisture, the phosphate groups can also be hydrolyzed into PA.

The P center band is also much broader (with full-width-at-half-maximum (FWHM) of ca. 5 – 7 ppm) than those of crystalline solids such as ADP, which has a FWHM of ca. 0.25 ppm. This is likely because the PA molecules in the fiber sample reside on the surface of the fiber nanovoids, thus experiencing a much more heterogeneous neighborhood than the P in a bulk crystal. The broad peak feature prevents distinction of PA vs phosphate based on chemical shift information alone.

The total signal areas of ^{31}P DP/MAS signals as a function of RD are shown in Figure 3. The relaxation behavior is neither single-exponential nor can be well-fitted by a bi-exponential model. A model composed of three single-exponential components (Figure 5) provides a satisfactory fit. The parameters obtained from the fitting are shown in Table 1. The physical meaning of this model will be explored later in the report in correlation with other experimental results.

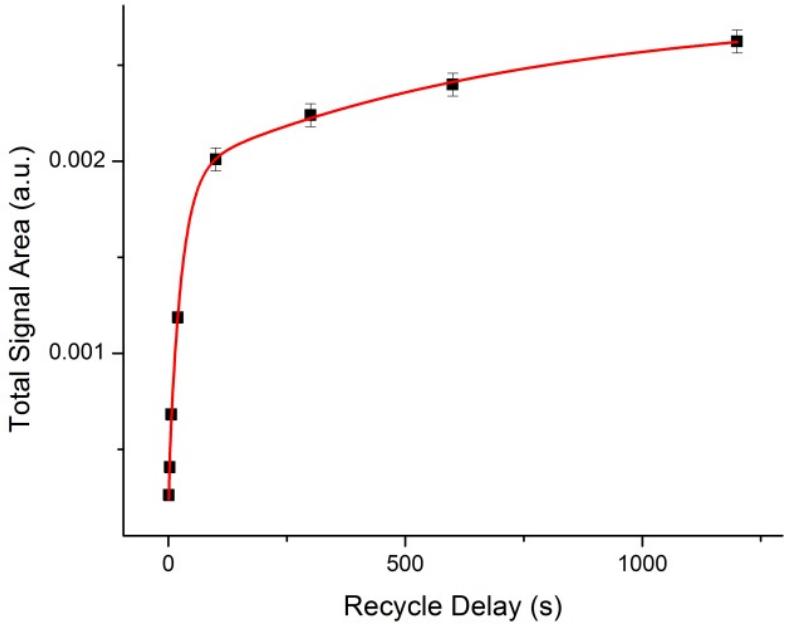

Figure 5. Total signal area of ^{31}P DP/MAS spectra of as-received PBO fiber as a function of RD (black squares), as well as a three-exponential fit (red curve). Error bars are estimated from S/N of the spectra.

Table 1. Parameters obtained from the three-exponential fitting of the 31P T1 relaxation data by DP/MAS experiments.

Component	^{31}P T_1 (s)	fraction
Fast	1.1	11%
Medium	26.7	59%
Slow	771.0	30%

T_1 relaxation is driven by molecular motion and reaches a minimum when the rate of the motion approaches the Larmor frequency (ω_L) of the probed nucleus (in the present report, the Larmor frequency of ^{31}P is ca. 243 MHz). Therefore, the species with low molecular mobility (such as the molecules in a rigid solid) would have long T_1, while those in a mobile

state would have a shorter T_1. So, the signals that have medium and long-T_1 relaxation times could be assigned to the PA molecules that are not plasticized by bound water molecules. The SSBs at RD = 300 s are much taller than at RD = 6 s, which confirms that the longer RD times correspond to both liquid and solid species, as solids are anisotropic while liquids species are mostly isotropic due to much higher mobility.

Although Figure 5 shows that the ^{31}P signal may still not be fully relaxed at 1200 s since P is a minor component in the sample, collecting data of enough signal-to-noise ratio (S/N) at RD > 1200s would be challenging.

The proton environment of the residual P could be probed by CP/MAS experiments. CP/MAS spectra of good signal intensities can be collected, with peak signatures similar to those in Figure 4(a). For the P species in the fiber, the enhancement factor, which is the total peak area ratio for CP vs DP at full relaxation (in the case of DP, at RD = 1200 s) and with the same number of scans, is about 80% of that can be achieved for ammonium phosphate at the same experimental conditions. Although the proton environments for the P species in the fiber and in ammonia phosphate are not the same, we may qualitatively state that at least a large portion of the P species in fiber has protons in the immediate surrounding. ^1H T_1 relaxation behavior was probed by recording CP/MAS signal area as a function of RD. The relaxation is approximately single-exponential, with a T_1 value of ca. 3.6 s.

The content of P can be quantified by measuring the signal area on the DP/MAS spectra and comparing with an external standard. Ammonium dihydrogen phosphate (ADP) was chosen as the external standard. As it has a long ^{31}P T_1, a combination of two techniques was used to calibrate its ^{31}P signal area: (1) a partially relaxed DP/MAS spectrum with RD

= 300 s, and (2) correction of the partial relaxation with a determination of its ^{31}P relaxation curve by CP/T_1 experiments[33] which found that the ^{31}P signal is ca. 87% relaxed at 300 s. For the spectrum at RD = 1200 s, the total ^{31}P content in the fiber was calculated to be 0.42% by weight, which is similar to the 0.3 – 0.4 wt% that was reported in the literature by elemental analysis[29]. Comparison with the elemental analysis result also suggests that the ^{31}P signals are nearly fully relaxed at 1200 s.

Complementary information about ^{31}P T_1 relaxation could be provided by CP/T_1 experiments.

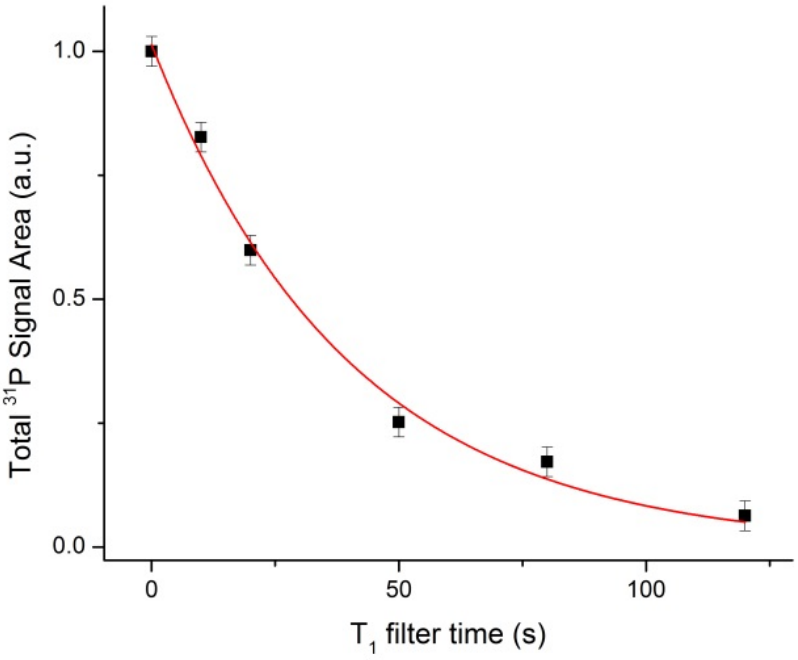

Figure 6. 31P T1 relaxation obtained by CP/T1 experiment with error bars representing standard deviation, estimated from S/N of the spectra.

As CP uses protons as the signal source and requires low segmental mobility for strong ^{1}H-^{31}P dipolar coupling to ensure CP efficiency, neither the liquid-like populations nor P

anhydrides contribute to CP signal intensity. If certain P species have protons nearby, but the protons have long T_1 due to either immobility or low proton density, or both, this population also would not contribute to the CP signal (Figure 6) shows the ^{31}P T_1 relaxation data obtained from the CP/T_1 experiment, as well as a single-exponential fit.

The ^{31}P T_1 relaxation time in the CP/T_1 data is similar to that of the intermediate component in the DP/MAS data fitting result (39.9 s for the former vs. 26.7 s for the latter), thus can be assigned to the same population. This population has limited mobility that results in a relatively long ^{31}P T_1. On the other hand, its good CP efficiency implies that it has proton neighbors within 0.5 nm. These clues would lead to the tentative assignment of this population to immobile PA. The low mobility is likely due to a low degree of hydration, as it is well known that anhydrous PA is a solid and becomes liquid upon hydration. The immobile P population could also include phosphates at the chain ends of the PBO molecules that are tightly bound within the bulk of the fiber.

The fast component (T_1 = 1.1 s) in DP/MAS data, which is missing in CP/T_1 data, is the liquid-like fraction that has low CP efficiency. It could be tentatively assigned to hydrated PA. The slow component (T_1 = 771 s) in DP/MAS data is missing in CP/T_1 experiment, which is likely due to the lack of protons in the immediate neighborhood, leading to low CP efficiency. This component could thus be tentatively assigned to phosphorous anhydrides.

In summary, the residual P in PBO fiber comprises P species with a broad range of protonation, or degree of hydrolyzation, which result in a broad range of molecular mobility, as indicated by ^{31}P and ^{1}H relaxation data.

2.3.2. 31P ssNMR of Treated Fibers

Next, the responses of these P species to moisture and temperature are examined. Figure 7(a) (red) shows the spectrum of PBO fiber that has been exposed to 40°C and 96% relative humidity (RH) for 6 weeks. The as-received fiber is also shown (Figure 7 (b); green) for comparison. Both spectra were acquired with RD = 6 s, thus both approximately represent liquid-like P species. As discussed in the previous section, the rigid P species are mostly invisible on the spectra at this experimental condition. Comparison of the two spectra shows that exposure to moisture significantly increases the liquid PA content. The signal area, expressed in terms of weight percentage of P in the fiber (with calibration by ADP), increases from 0.13% for the as-received fiber to 0.24% after 6 weeks of moisture exposure. Note that these numbers are only approximations of liquid-like populations, as the partially-relaxed solid-like population also contributes to the signal area to a small extent.

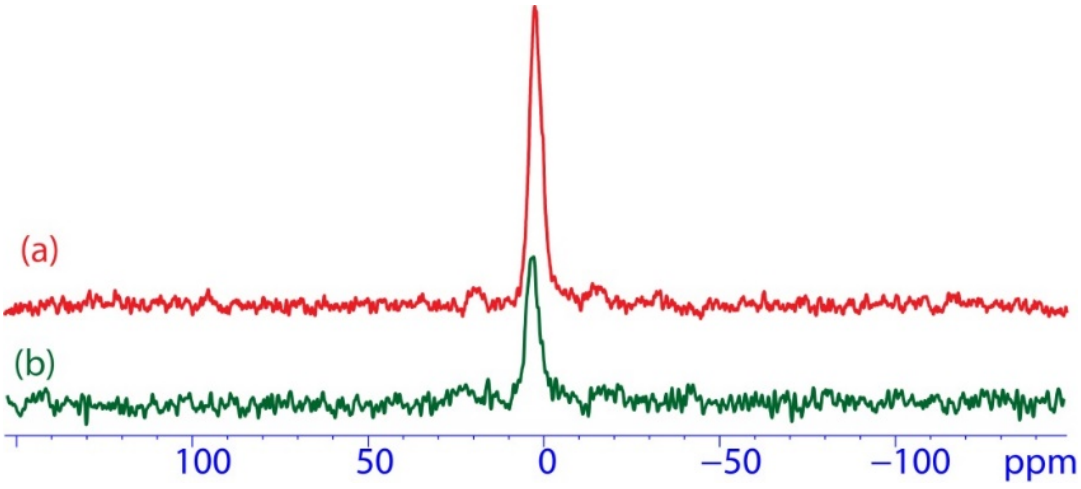

Figure 7. ^{31}P DP/MAS spectra of PBO fiber exposed in 40°C and 96% relative humidity for 6 weeks (a) and as-received fiber (b). RD = 6 s.

Such an increase is likely because the rigid species that are invisible in this experimental condition, upon exposing in moisture, converts to hydrated (and thus plasticized) PA and

becomes observable on the spectra. Notably, SSBs are mostly non-existent in both cases, supporting the assignment of these peaks to liquid-like species.

Conversely, heat treatment converts liquid PA back to solids. Figure 8 shows the spectra of PBO fiber exposed in 40°C and 96% RH for 1 week (condition A; red) and the fiber with condition-A treatment followed by 2 days of exposure at 90°C and zero humidity. Both spectra were acquired with RD = 6 s, at which condition the observable signal is composed of mostly liquid-like species while the rigid species are invisible. The heat treatment converts most of the liquid-like signal to solids, which is consistent with the well-known behavior of PA[29], which, at higher temperatures, would lose water and turn into less hydrated structures such as PPA, metaphosphoric acid (HPO_3), and anhydrides. The melting points of these structures increase at increasing level of dehydration.

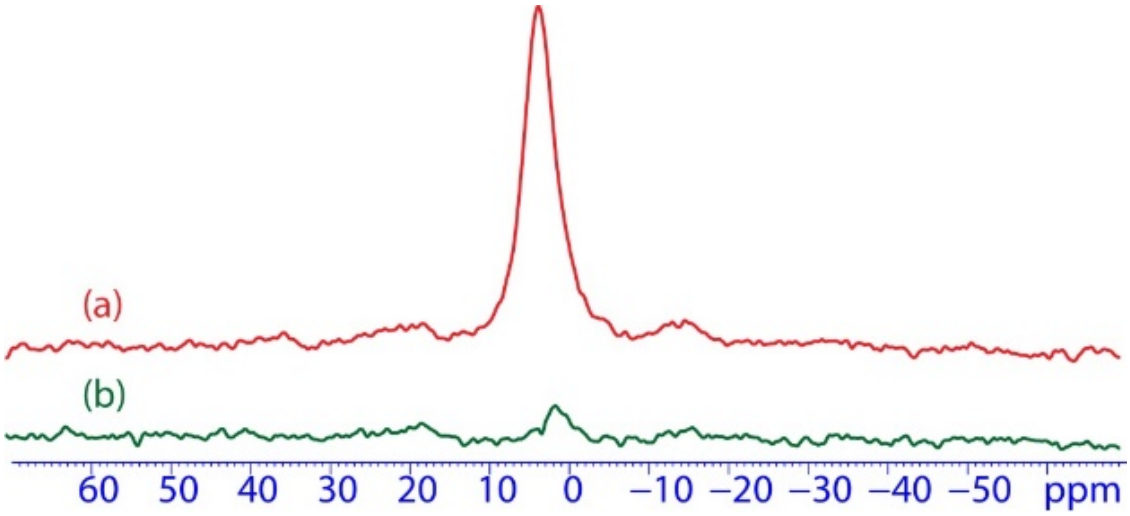

Figure 8. ^{31}P DP/MAS spectra of PBO fiber exposed at 40°C and 96% relative humidity for 1 week ("treatment A")(a; red) and treatment A followed by 2 days exposure at 90°C and zero humidity (b; green). RD = 6 s.

The potential of the various P species to react with the polymer matrix depend on their physical states. Liquid-like P molecules are more acidic, can maintain intimate contact with the fiber surface and easily migrate, thus have a greater potential to cause damage. On the

other hand, solid-like P molecules have limited contact with the fiber matrix and lack the ability to migrate, and thus have very limited capability to cause damage. Therefore, the ^{31}P NMR observations are consistent with the results reported in the literature that while high humidity degrades the fibers quickly[21,29] hot and dry environment do not[23].

More severe heat treatments continue to drive the P species to more dehydrated structures. Figure 9 shows the ^{31}P CP/MAS spectrum of PBO fiber exposed in 200°C and zero humidity for 24 hours. In contrast to DP/MAS with short RD, which detects mainly liquid-like species, CP/MAS detects mainly rigid species, with the exception of the P species that do not have protons in the neighborhood (anhydrides).

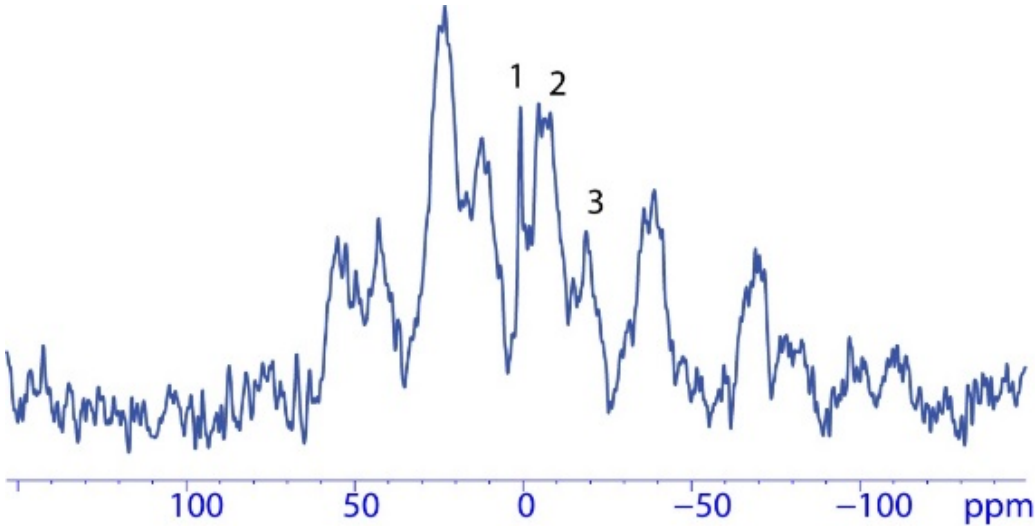

Figure 9. ^{31}P CP/MAS spectrum of PBO fiber exposed in 200°C and zero humidity for 24 hours. Three center bands are observed (indicated by numbers), and all other peaks are SSBs. Spinning speed was 7.5 kHz.

In Figure 9, three center bands are observed: peaks 1 (1 ppm), 2 (-7 ppm) and 3 (-19 ppm). Other peaks are SSBs (assigned by varying the spinning speed and observe the movement of the peaks). These three peaks appear at similar positions as those in bulk PPA, at 0, -12, and -25 ppm, corresponding to P monomers, P that has one P neighbor (end units of oligomer), and P that has two P neighbors (middle units of oligomer), respectively. PPA is

a mixture of oligomers of PA of various lengths. It easily reacts with water[34] and produces PA (monomer) and other smaller oligomers. Conversely, elevated temperatures cause PA to lose water and polymerize into PPA. Therefore, we can reasonably assign the CP/MAS signals to PPA that is immobile due to the low level of hydration. The somewhat different chemical shifts between the residual P peaks and the bulk PPA peaks could be due to a variety of factors, including different hydration environments, different bond conformations, different physical neighborhoods (adsorbed onto fiber surface vs. in bulk liquid), etc. It is also possible to generate P anhydrides under this heat treatment, but CP/MAS would not be able to generate signals for this population due to the lack of protons in the structure.

2.3.3. Accessibility of Residual P by Moisture

The kinetics of moisture diffusing into the fiber and hydrating the P species can be observed by exposing the heat-treated fibers, which shows no liquid-like P species, to moisture and watch the increase of the liquid P peaks. Figure 10 shows the DP/MAS spectra of PBO fiber treated at 200°C and zero humidity for 24 hours followed by various exposure time in 40°C and 96% RH. The recycle delay was 6s for all the spectra, which mostly detects liquid-like species. At zero exposure time, there is no observable liquid-like signal, indicating the heat treatment has effectively immobilized all the P species. At moisture exposure of only 2 hours, the solid P species already begin to mobilize, as seen from the increased signal intensity in Figure 10. The three peaks appear at similar positions to that of PPA, thus could be assigned to monomeric PA (ca. 3 ppm), end-units of PPA (ca. -7 ppm), and middle-units of PPA (ca. -19 ppm), respectively. At short exposure times (<= 4 hours), the major hydrolysis products are oligomers, as indicated by a very small peak at 3

ppm and larger peaks at -7 ppm and -19 ppm. At longer exposure time, the monomeric peak begins to increase in intensity. This is consistent with the well-known hydration pathway of phosphorous as depicted in Scheme 1. The peak shapes and positions slightly vary at each exposure time, which is likely due to the structural and physical heterogeneity of the residual P in the fiber, as different fiber sample was used at each exposure time.

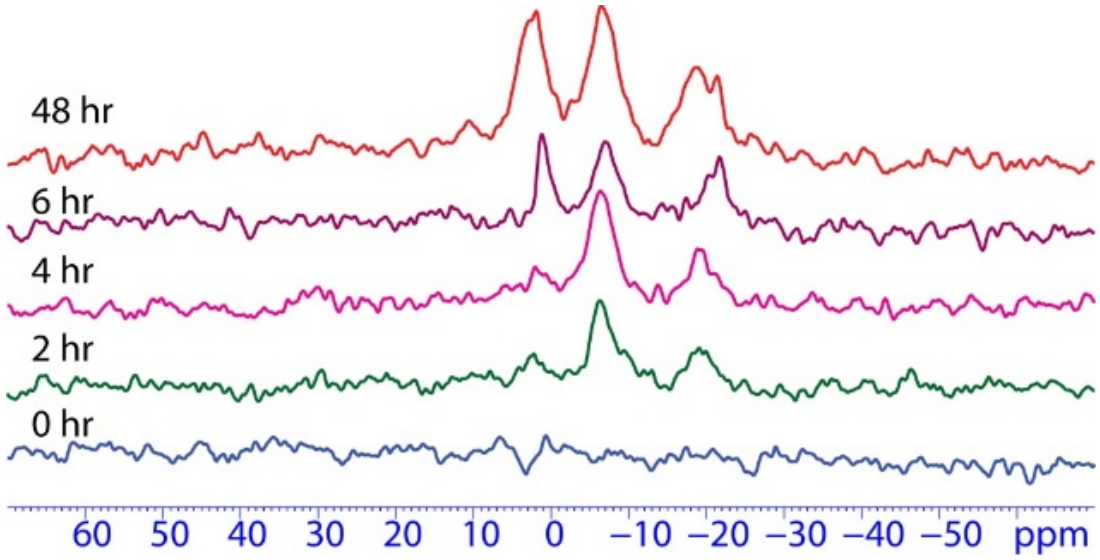

Figure 10. ^{31}P DP/MAS spectrum of PBO fiber treated at 200°C and zero humidity for 24 hours followed by various exposure time at 40°C and 96% RH. RD = 6 s.

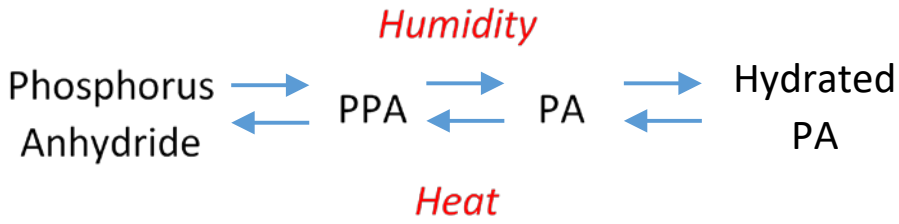

Scheme 1. Evolution of phosphorous species under the influence of heat and humidity

The kinetics of the reactions between the residual P species and water would be determined by two processes: permeation of the water molecules into the fiber nanovoids, and the subsequent reactions between the water and the P species. It is well known that the reaction between highly dehydrated P species such as P_2O_5 and water is extremely fast. On the other hand, less dehydrated P species such as PPA oligomers would react much more slowly with water, especially at lower temperatures. This explains the experimental observation that the mechanical degradation proceeds much faster at a higher temperature, given similar high-humidity conditions[16].

2.4. Preliminary Exploration of Treatment Strategies

While the above results show that the nanovoids in the PBO fiber can be easily accessed by gaseous water molecules, most of the residual P is inaccessible to aqueous media. Soxhlet extraction[21] and supercritical CO_2[30]were only able to extract a small fraction of P, and treatment with a base in the liquid state not only failed to neutralize the acid, but caused further degradation of the fiber[30]. This could be because the residual P in the nanovoids is inaccessible to aqueous media due to the large surface tension that must be overcome. Therefore, one possibility of mitigating the PBO fiber environmental stability problem is to treat with gas molecules that can diffuse into the nanovoids, react with the residual P species, and change the chemical identity of the P species. One of the gaseous candidates that could interact with the residual P is ammonia, which could react with and increase the pH values of the P species and thus slow down the rate of hydrolytic degradation due to acid-catalyzed benzoxazole bond scission. Figure 11(a) (red) shows the DP/MAS spectrum of a PBO fiber that has been exposed to saturated vapor pressure (ca. 70 psi) of ammonia

at room temperature for one week. The experiment was acquired with RD = 6 s, under which condition the spectrum mostly detects liquid-like P species. The spectrum of the as-received fiber acquired under the same condition (Figure 11(b); green) is also shown for comparison. The ammonia-treated sample shows a spectrum that is mainly between 0 and 10 ppm and notably broadened as compared to the original fiber. The different peak signatures indicate that ammonia may have accessed the nanovoids and reacted with the P species. The most likely reaction product would be ammonium dihydrogen phosphate, $NH_4H_2PO_4$. It should be noted that the above NMR experimental condition only probed the liquid-like P population, while the reactivity and accessibility of solid-like P species with ammonia are unknown and would be the subject of future studies.

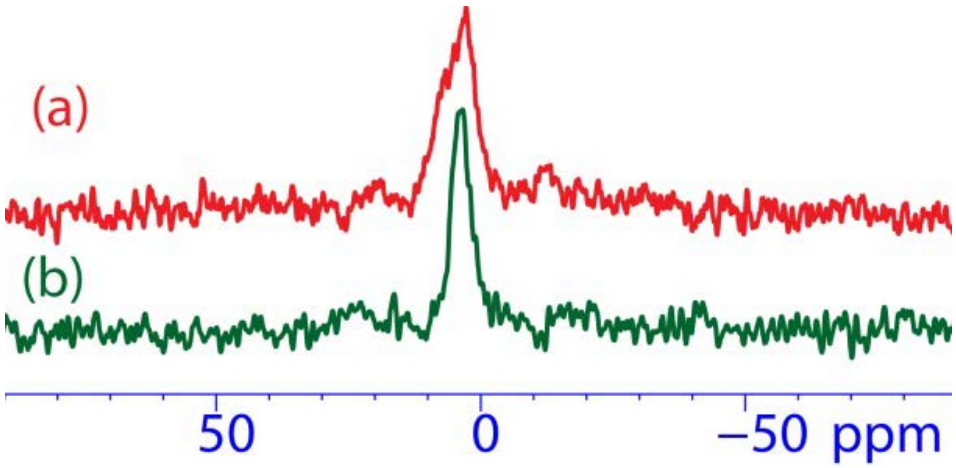

Figure 11. ^{31}P DP/MAS spectrum of PBO fiber exposed to ammonia (ca. 70 psi and 20°C) for one week (a) and as-received fiber (b).

However, our preliminary mechanical measurements indicate that the ammonia treatment itself caused a loss of tensile strength (Figure 12). For the fiber that was exposed in ammonia for one-week, further exposure in 40°C and 96% RH environment seems to lose strength slower than the as-received fiber, though more data and longer aging periods are

needed to further confirm this trend. The loss of mechanical properties with ammonia treatment is consistent with previous works on the effect of bases on PBO fibers [29,30].

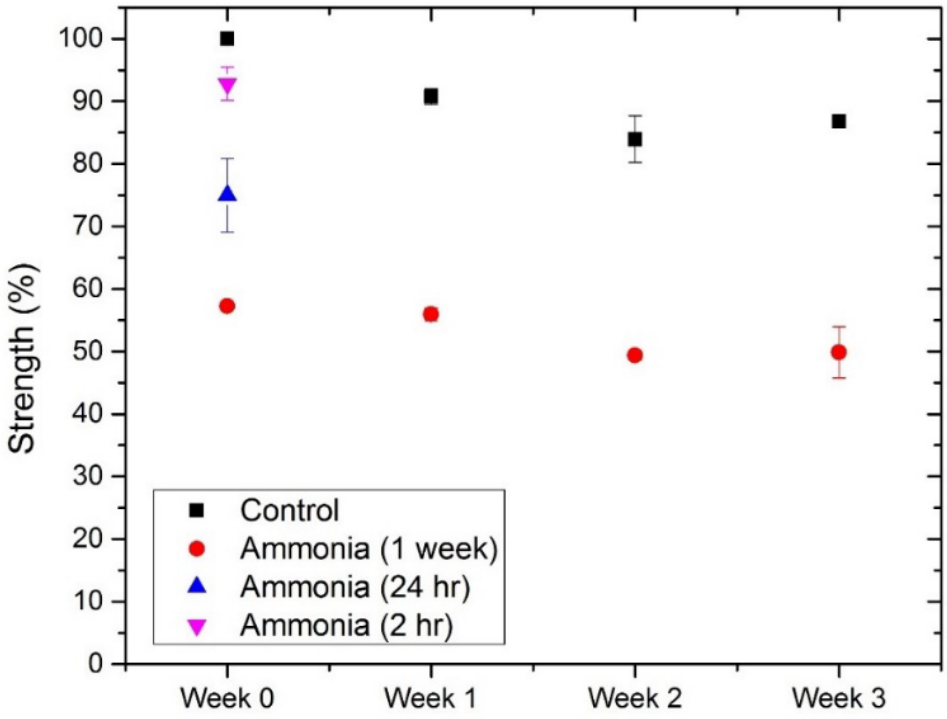

Figure 12. Tensile strength retention of ammonia-treated (red circle as well as triangles) and as-received (black square) PBO fiber as a function of exposure time at 40°C and 96% RH. Error bars are indicated (several points have error bars that are within the symbols).

2.5. Conclusions

The chemical structure and physical state of residual P, speculated to cause rapid degradation of PBO fiber strength in the presence of humidity, were studied using ^{31}P ssNMR. It was found that that the residual P was mainly in the form of PA and it's various hydrated or dehydrated forms. Humidity hydrolyzes the residual P to PA, whose acidic nature and ability to migrate are highly effective in hydrolyzing the oxazole bonds. Exposing the fibers in hot conditions in the absence of humidity causes the reverse to happen, i.e. the mobile PA dehydrates and becomes rigid. Kinetic studies of 200°C heat-

treated fibers exposed to humidity show that the rigid species first convert to PPA in as quickly as two hours. This PPA then converts to PA upon further exposure to moisture. These results support the proposed mechanism in the literature that the residual P catalyzes the hydrolytic degradation of PBO fibers. Treatment of the fibers with a basic gas such as ammonia was able to change the chemical nature of the residual P species. However, the treatment reduced the mechanical strength of the fibers. The results demonstrate that ssNMR is not only a useful tool to study the environmental stability of high performance fibers, it is a useful guide for the development of mitigation strategies.

CHAPTER 3

IMPROVING MECHANICAL PERFORMANCE OF KEVLAR® FIBER-REINFORCED COMPOSITES

3.1.Introduction

Poly-paraphenylene terephthalamide (PPTA) reinforced long fiber composites are employed in a variety of areas including aerospace, automobiles, and personal protection in soft body armors for ballistic protection. First introduced by Dupont in 1971 as Kevlar®, or PPTA fibers (also known as Twaron® or Technora®) have gained widespread importance due to their extraordinary high modulus and tensile strength[17]. These properties are attributed to its molecular structure and fiber microstructure[36–40]. However, the strength of composites prepared from PPTA fibers is limited by poor interfacial adhesion between the fiber and the matrix[41–43]. Inadequate adhesion constrains the overall performance since the high potential of the fiber is not realized due to premature interfacial failure.

PPTA fibers are also processed using the dry-jet wet spinning process similar to PBO fibers, the only difference that the solvent is sulfuric acid. PPTA in solution forms a liquid crystalline phase, and thus the solution has high anisotropy even before the fiber is spun. In addition, the high extensional forces in the dry-jet wet spinning process impart additional anisotropy when spun. One can compare anisotropy of aramid fibers to conventional melt processed polyamide fibers using wide angle X-ray scattering and calculating an orientation parameter, a value of 0 indicating complete isotropy while a value of 1 indicating complete anisotropy. Figure 13 compares the wide-angle X-ray scattering patterns of Polyamide 12 and PPTA fibers. Both show patterns that are typical of anisotropic systems like fibers. An orientation parameter can be calculated from these scattering results, using a Cinader and Burghardt approach, where a value of 0 indicates

isotropy, whereas a value of 1 indicates perfect anisotropy[44]. The calculated value for orientation was 0.5 for Polyamide 12 fibers and 0.8 for PPTA, indicating the much higher molecular anisotropy in PPTA as compared to conventional polyamide fibers. Various approaches have been studied to improve the adhesion of PPTA fibers to various matrices with little or no improvement. Most of them have involved functionalizing the surface[45–52] to generate chemical interaction with the corresponding matrix. Some treatments also introduce fiber roughness[46,53]. Additional techniques have also involved dip-coating the fibers in adhesives[54]. However, the aromatic nature of the backbone and the physical microstructure of the PPTA fiber make it more difficult to form fiber-matrix covalent bonds as compared to glass or carbon fibers[55] thereby limiting the potential performance of composites using this class of fiber.

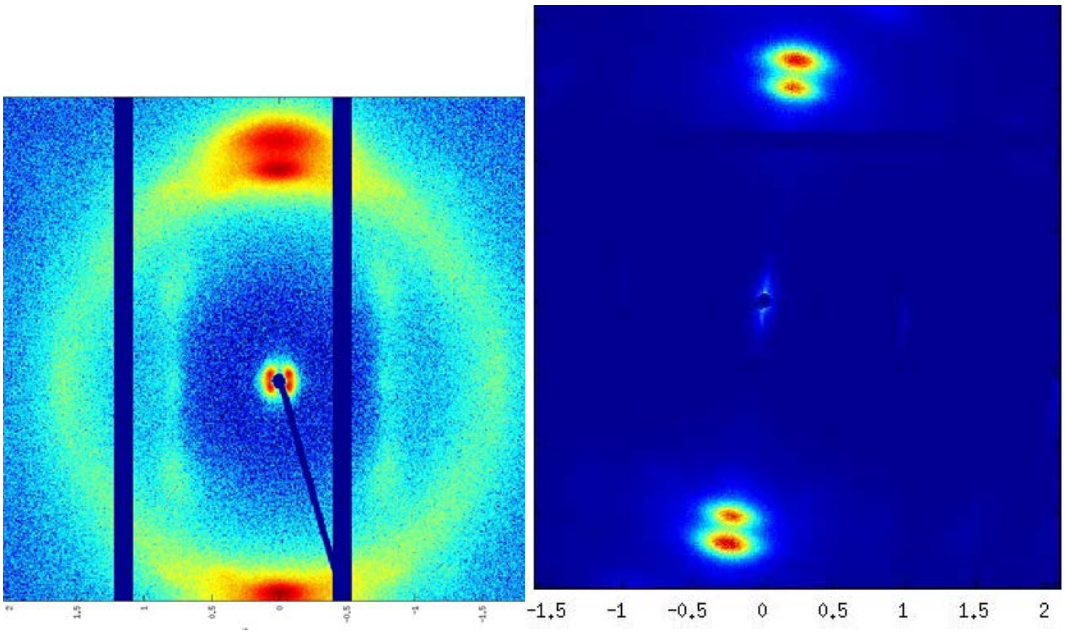

Figure 13. Wide angle X-Ray scattering of Polyamide 12 vs PPTA fibers. Polyamide 12 showed an orientation parameter of 0.5, whereas PPTA showed a value of 0.81

Herein we report a new strategy to improve composite performance by first, altering the fiber surface morphology to allow for penetration of reactive monomers into the fiber subsurface, and second, treatment of these reactive monomers to enable covalent bonding to occur on the fiber surface and within its subsurface when the rubber matrix is cured (vulcanized). A necessary part of our strategy is to compromise some of the PPTA fiber properties from the applied pre-treatments to allow for significantly increased load transfer from the rubber matrix, thereby enhancing the composite performance. It should be noted that the specific methods employed herein are tailored for this composite system, but the concept of modification of the interphase region is quite general and can be applied to other composite systems. These treatments have been patented by Bridgestone, America[56] and the supporting research is described in this chapter.

3.2. Approach

PPTA fibers (840 denier, 534 filaments) were obtained from Dupont Chemicals Co and used as is. Uncross-linked natural rubber (poly cis-isoprene) latex with sulfur premixed as cross-linker was provided by Bridgestone America and used as the matrix.

The fiber pre-treatments are selected to promote enhanced surface area and sub-surface area in the fiber itself to allow for better transfer of coupling agents into the fiber interphase regions using supercritical carbon dioxide $scCO_2$. Two pre-treatment methods that change the surface morphology of the fibers were selected. The first pre-treatment was chosen to exploit the sub-surface nano-voids present in these fibers while the other takes advantage of the relatively weak compressive properties of the fiber[57]. It is acknowledged that a drop in fiber strength due these treatments is expected, but ultimately this is acceptable because

the treatments enhance the interfacial adhesion between the fiber and matrix and improve overall composite performance.

After the pre-treatment step, fibers are treated with reactive monomers to chemically bind the fiber surface and subsurface to the rubber matrix. The reactive monomers reported herein are selected based on their ability to take part in the cross-linking mechanism and potentially increase the cross-linking density of the rubber matrix in the fiber interphase region. Finally, test samples were fabricated by curing the rubber matrix in the presence of the fibers to create test specimens necessary for evaluation of adhesion.

3.2.1. Fiber Pre-Treatments

Multiple pre-treatments were considered and two were shortlisted; a mechanical pre-treatment and a microwave pre-treatment. These treatments were selected to take advantage of the inherent properties or flaws of the fiber. The mechanical pre-treatment was designed to exploit the relatively weak compressive properties of PPTA[57,58]. Compressive elastica[59] tests performed on the fibers have shown they deform in a non-Hookean manner at very low bending strains and this deformation is plastic in nature.

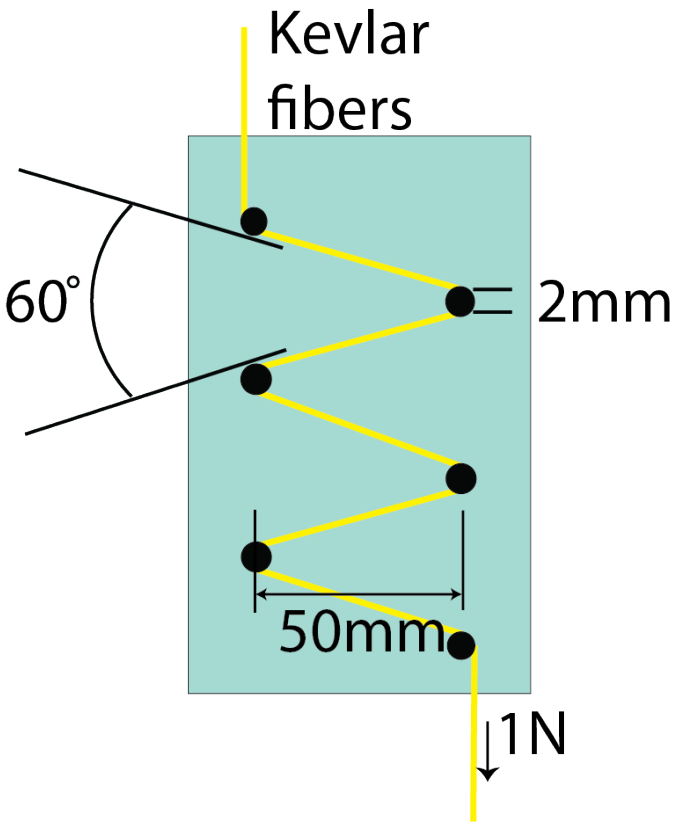

Figure 14. Mechanical treatment setup

To exploit this property and introduce buckling on the fiber surface, a simple setup is used on the Instron 5500R tensile testing machine to induce compression (see Figure 14). Metal cylinders of diameter 2mm were embedded in a wooden frame in a zig-zag fashion as shown in the figure. One end of the fiber bundle was tied to a weight of 0.1kg, weaved over the metal cylinders and the other end secured to the Instron tensile testing machine. The Instron was the programmed to pull the fiber bundle at a crosshead speed of 500mm/min and introduce compression.

The second pre-treatment was chosen to expoit the sub-surface voids of the fiber. Microwave radiation has been used to create finely divided graphite with sulfuric acid[60] acting as an intercalating agent. In this process, graphite is first soaked in sulfuric acid.

Next, the soaked graphite is exposed to microwaves, volatilizing the acid and forcing rapid expansion and exfoliation of graphite platelets. A similar approach is devised here to open up the sub-surface voids of PPTA fibers since trace levels of sulfuric acid are already known to be present within them(a consequence of the dry-jet wet-spinning process). Since there is an affinity of sulfuric acid to the voids for PPTA fibers, a soak in 50% sulfuric acid for a period of 1 hour at room temperature is carried out prior to subjecting the fibers to microwaves. The fibers are immersed in water and treated with microwaves in a CEM Discover SP microwave synthesizer to volatilize and exfoliate the fiber surface. The microwave conditions were fixed at 100W for 2 minutes. The fibers were then washed and dried. The effect of these pre-treatments on the properties of the fiber was studied using single fiber tests and small angle X-ray scattering. Fiber morphology was studied using Scanning Electron Microscopy. Scanning electron microscopy was performed either using an FEI Magellan 400 FESEM or a JEOL JCM-5000 SEM. Small Angle X-ray scattering was performed using a Ganesha SAX-LAB instrument.

Tensile tests on the single fibers were performed using an Instron Tensile testing machine equipped with a 50N load cell. Prior to testing, single fibers were mounted using a 3M general purpose commercial grade epoxy on a rectangular cardboard frame with a smaller rectangular hole having a gauge length of 50mm. The frame containing the fiber was then mounted onto the test machine grips. Next, the frame was cut on both sides at appropriate

places. The fiber was then tested in tension at a crosshead speed of 1mm/min until failure. A minimum of 10 fibers were tested for each condition.

3.2.2. Reactive Monomer Infusion

The pre-treated fibers are then soaked in reactive monomers. The soak was carried out both in the presence of $scCO_2$ and in ambient conditions at room temperature and pressure. Carbon dioxide of purity grade>99% was obtained from Airgas and used as is. The effect of $scCO_2$ on such high performance fiber's strength has been studied and shown to have no detrimental effect[29,30]. The reactive monomers that were considered are; Divinyl Benzene (DVB) (80%) and tetramethyl-tetravinyl-cyclotetrasiloxane (D4V) (90%), both of which were obtained from Sigma Aldrich and used without dilution. These monomers where chosen for their ability to act as a coupling agent, discussed in more detail in the results and discussion section. After pre-treatments, PPTA fiber bundles were placed in test tubes filled with coupling agents. Ambient condition soak was performed wherein fiber bundles were soaked in coupling agents at room temperature(~20°C) and pressure (15psi) for a duration of one hour. The test tubes were placed in high-pressure reactors for the soak in $scCO_2$. Carbon dioxide was pumped into the reactors to a pressure of 5000 psi using a Thar Designs P200 high-pressure pump. The reactor was then heated to 50°C and

maintained for 1 hour. Afterward, depressurization was carried out in 1-2 seconds. To measure adhesion, test specimens were fabricated as shown in Figure 15.

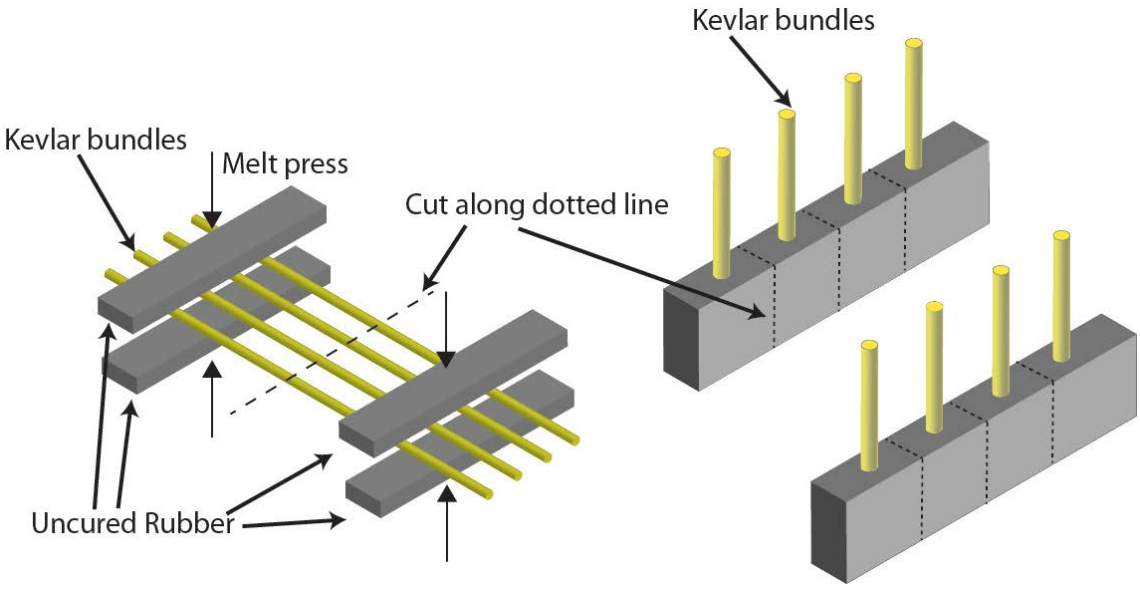

Figure 15. Fabrication of composites for adhesion tests

It should be noted that the embedded length L used in the adhesion test geometry shown in Figure 16, was determined from shear lag analyses (discussed later).

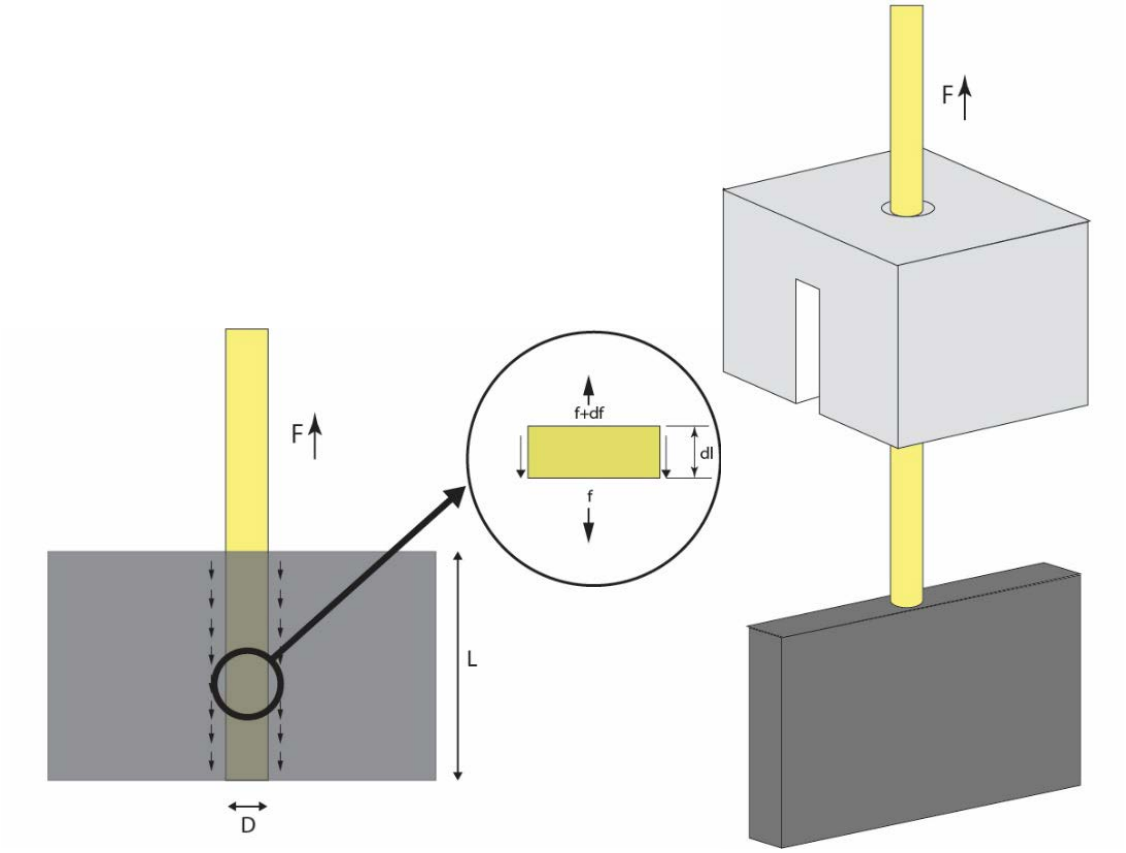

Figure 16. Restrained top loading condition

The shear lag model analyses ensure that the stress distribution is uniform for the chosen fiber length. The fabrication process involved placing treated fiber bundles between strips of uncured rubber in a custom mold, followed by curing of the rubber together with reactive monomers in a compression molding setup under pressure and temperature. Fiber bundles were first subject to a fixed amount of twist (150 turns/m) to present a uniform surface area to the matrix. Curing was performed for 20 minutes at a temperature of 160ºC.

The fiber composite test specimens were then secured using a setup on the Instron 5500R Tensile testing machine with a 10kN load cell. The setup ensured a restrained top loading

condition on the rubber matrix. The fiber bundle was then pulled until failure, i.e. the fiber bundle was completely pulled out of the rubber matrix. Adhesion tests were performed on various combinations of pre-treatments and coupling agents. A minimum of five samples were used for each type of treatment. Fracture surfaces from the pull-out tests were observed under the SEM to determine the mode of failure.

3.3.Results and Discussion

3.3.1. Effect of Pre-Treatments

PPTA fibers are processed using a dry-jet wet spinning process, which leads to extremely high molecular anisotropy. Detailed studies have shown that PPTA fibers have a pleated structure where lamellae are stacked in a radially oriented fashion[36,37]. Inter-lamellar hydrogen bonding and high crystallinity are found to be contributors to the fiber's strength[61]. An important characteristic of the dry-jet wet-spinning process is that it leads to the presence of sub-surface nano-voids[62] caused due to the entrapment of traces of sulfuric acid (solvent). Our approach was to harness these voids to develop fiber texture using microwave radiation.

As detailed in the experimental section, PPTA fibers that are initially soaked in sulfuric acid followed by exposure to microwave radiation produce interesting surface blisters (see Figure 17). This suggests that the sulfuric acid present in the fiber volatilizes and escapes, causing the formation of blisters during this process. These blisters were not observed when the process was carried out only with water, suggesting that the acid had a role to play in

permeation of water into the fiber, however more detailed tests are required to decouple the exact role of acid in this process.

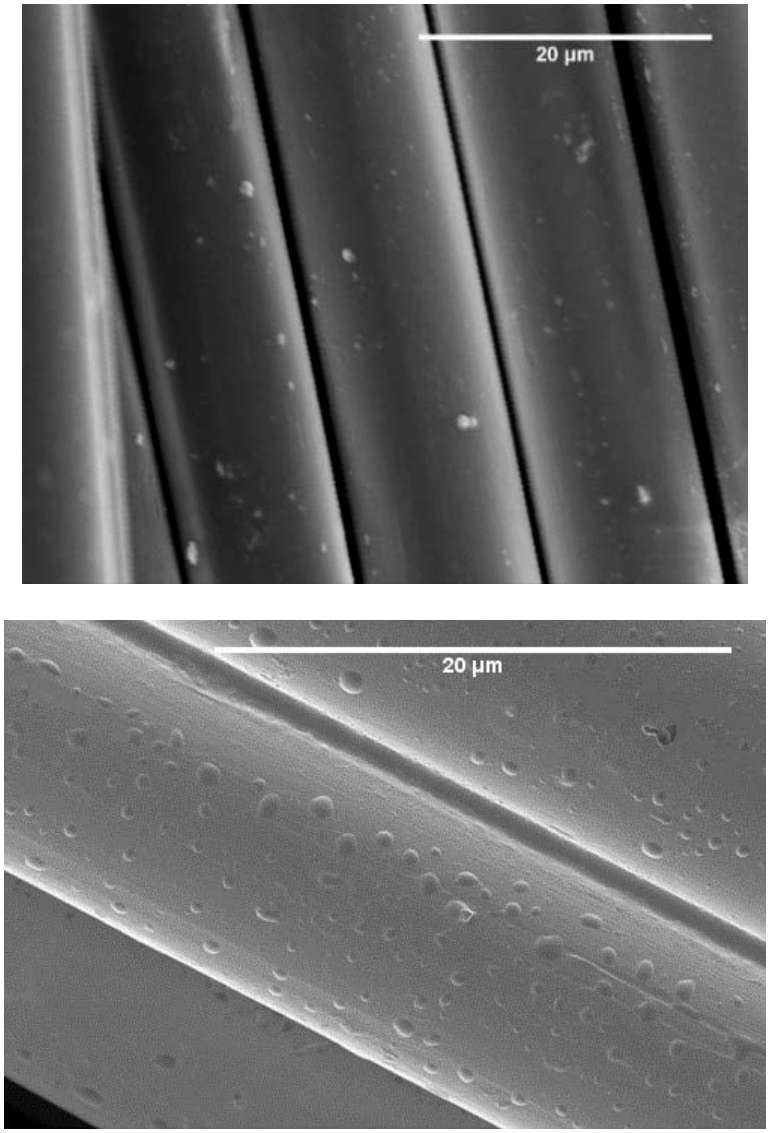

Figure 17. Scanning electron micrographs of untreated fibers (top), compared to the microwave treated fiber (bottom). Note the subsurface blister pattern produced on the fiber resulting from the treatment.

The mechanical pre-treatment, also detailed in the experimental section, is designed to take advantage of the relatively weak compressive properties of the fiber and promote increased surface area resulting from the formation of kink bands and delamination of fiber. It is

acknowledged that both these pre-treatments cause a loss of strength and modulus, as is quantified later, but is ultimately acceptable to improve overall mechanical properties of the composite. Optical microscope and SEM images show, typical evidence for buckling under compression, i.e. ‘v’ notches or kink bands and fibrillation (Figure 18).

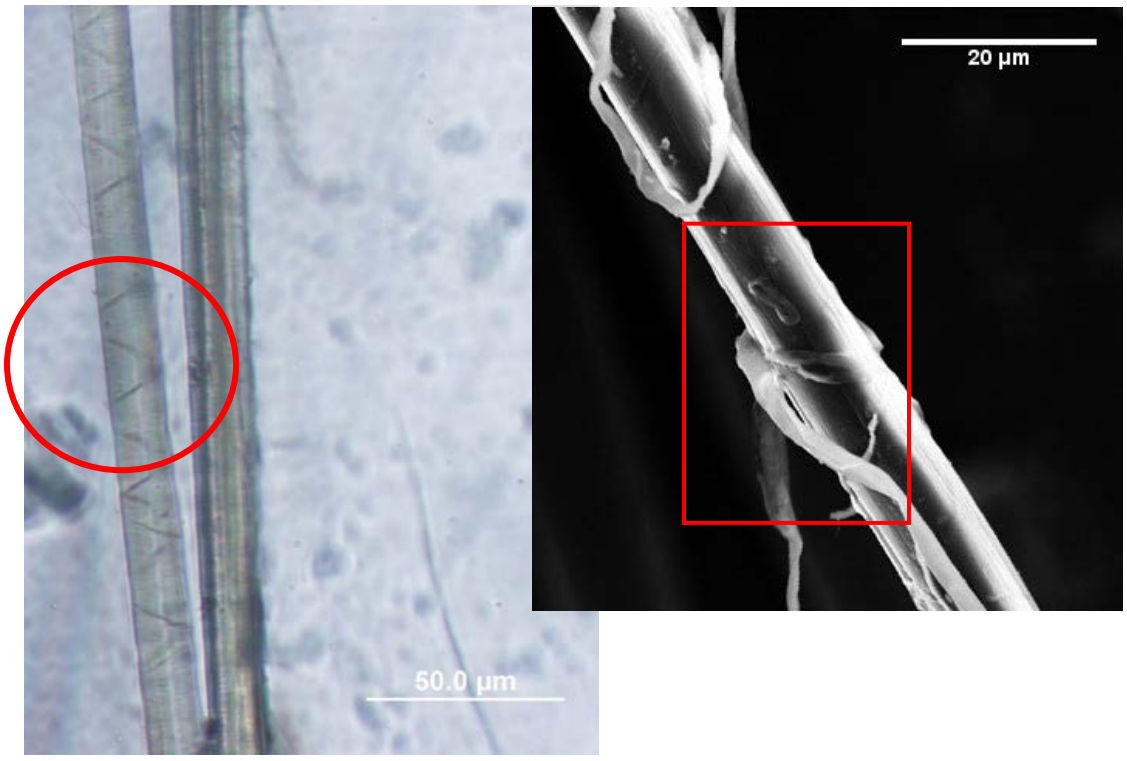

Figure 18. Optical(left) and Scanning Electron Microscopy (right) images of mechanically treated fibers show ‘v’ shaped kink bands (encircled) and fibrillation (boxed).

Small angle X-Ray analysis was conducted on fibers after both pre-treatments were applied to identify if any subsurface area was created at the nanometer length scale. Voids provide the highest intensity in the small angle regime since they provide the greatest electron density difference for scattering in relation to the bulk. The voids in PPTA fibers are known to be mostly located on the periphery and have a very high aspect ratio, oriented in the axial direction. A simple Guinier approximation[62] was performed to determine void widths.

For this approximation, the voids are assumed to be elliptical, with the major axes oriented in the axial direction, and having a circular cross section. Figure 21 shows the SAXS patterns of control and treated fibers. Fitting equation 7 to the slope of the normalized log(intensity) vs q^2 to (Figure 19) at *q=0 (q is the scattering vector)*, we can get the value of a, the void width from the relation $a = 0.54 * (slope)^{\frac{1}{2}}$. We get void widths of *54, 56 and 46 nm* for control, mechanical and microwave pre-treated fibers respectively which are the same order as values reported by Dobb et al.

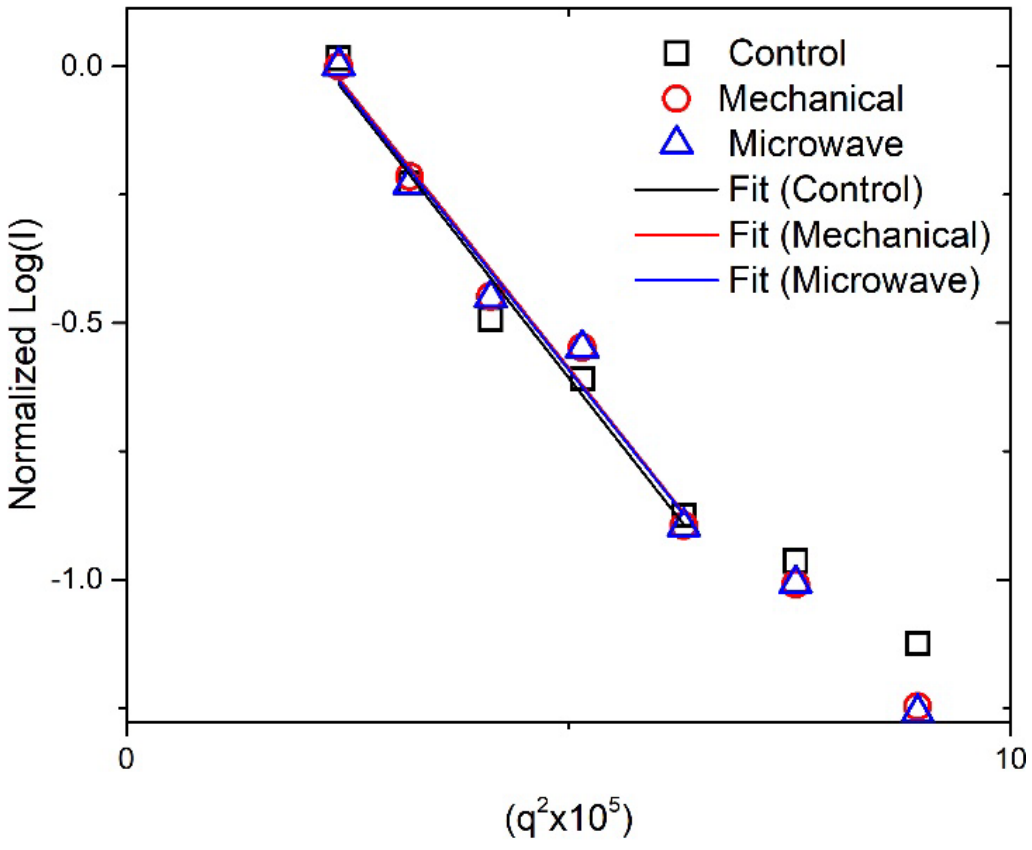

Figure 19. Guinier Analysis and fit

$$\log_{10} I(q) = -\frac{4\pi^2 q^2}{5}(a)^2 \log_{10} e + constant \quad (7)$$

Table 2. Void Widths from Guinier Analysis

Treatment	Void width (nm)	R^2
Control	54	0.97
Mechanical	56	0.97
Microwave	46	0.96

Since this Guinier approximation in equation 7 has been derived for a monodisperse system of ellipsoidal particles of width a[63], these values should be treated cautiously, and not compared with values obtained from other techniques. The void width values indicate that the sub-surface voids have not changed in size (Table 2). Therefore, it seems that the pre-treatments do not affect the voids in a measurable way but serve to change the surface morphology or texture significantly.

Single fiber fragmentation tests were also performed as described in the experimental section. The results are in shown in Figure 20.

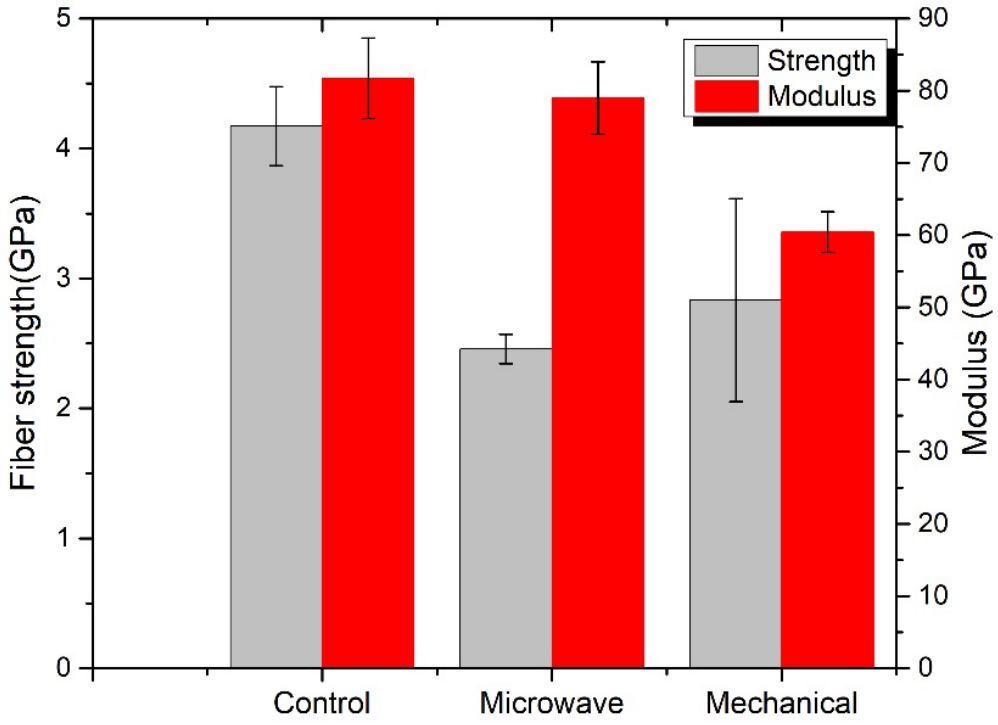

Figure 20. Effect of pre-treatment on the fiber stiffness and strength.

Table 3. Effect of pre-treatments on Fiber Properties

	Tensile Strength(%)	Modulus(%)
Microwave	59	97
Mechanical	68	75

For the treatment parameters chosen, tensile strength and modulus for the treated fibers are quantified in terms of values of control fibers in Table 3. The treatment conditions have not been optimized, so further fine tuning of these treatments can be done to minimize the damage and maximize surface texture. Note that the mechanical treatment has a more significant effect on the modulus rather than the strength when compared to the microwave treatment process. This arises from the fact that the mechanical treatment primarily causes in increase in the internal surface area that results primarily in softening of the fiber. In contrast, the microwave treatment can cause significant degradation through chain scission, which in turn, results in losses to fiber strength whereas the modulus is relatively insensitive[29,30].

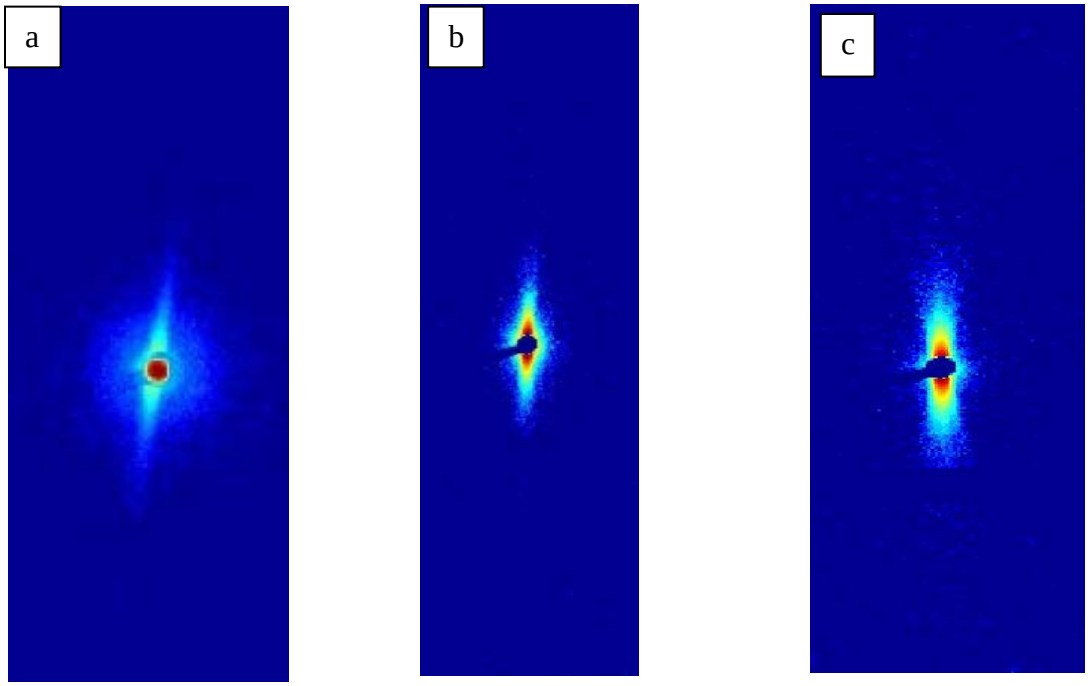

Figure 21. SAXS images of a) Control, b) Mechanical and c) Microwave pre-treated fibers

3.3.2. Effect of Coupling Agents

Two reactive monomers were selected for this study; a low molecular weight silicone tetramethyl-tetravinyl-cyclotetrasiloxane (D4V), and Divinyl Benzene (DVB). Their basic structures and molecular weights are shown in Table 4. These monomers were selected based on their high vinyl functionality (4 and 2 respectively) and relatively low molecular weight. The vinyl functionality is necessary to crosslink with the rubber (poly cis-isoprene) during the vulcanization process currently used in the fabrication of commercial tires by Bridgestone, America.

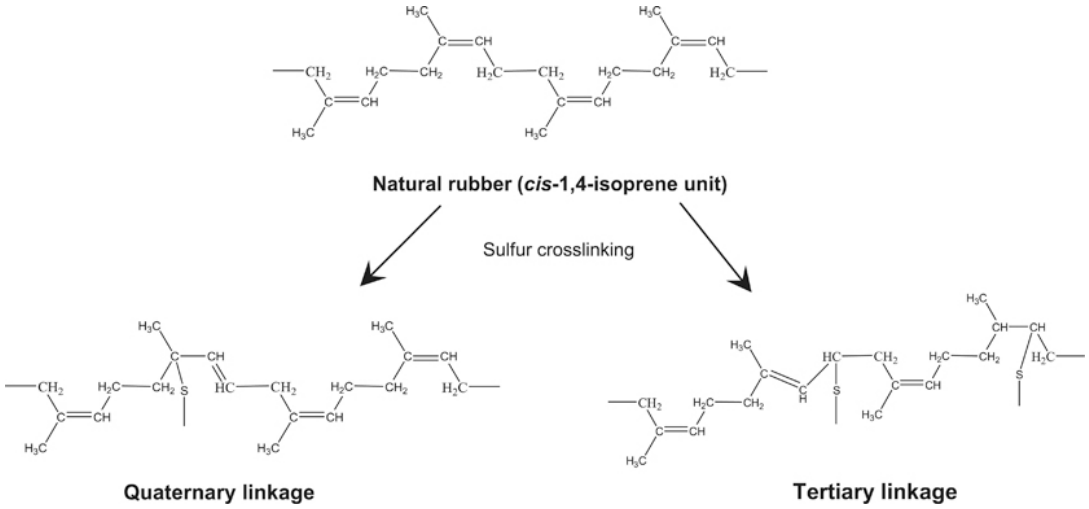

Figure 22. Mechanism of crosslinking of natural rubber

The mechanism of crosslinking of natural rubber with sulfur is well-known and involves a hydride abstraction step and also an addition to a double bond in the backbone chain[64,65] to create cross-links or bridges between adjacent polymer chains. Both DVB and D4V are known to polymerize to form solids[66,67]. DVB can be polymerized thermally or with the presence of radical initiators to form a crosslinked solid, whereas D4V undergoes cationic or thermally induced ring-opening polymerization to form a linear polymer[68,69]. Therefore,

one can expect these compounds to participate in the cross-linking of rubber, aided by the initiators already present within the rubber and the curing process, and increase crosslink density. The curing exotherm of the natural rubber provided is shown in Figure 23.

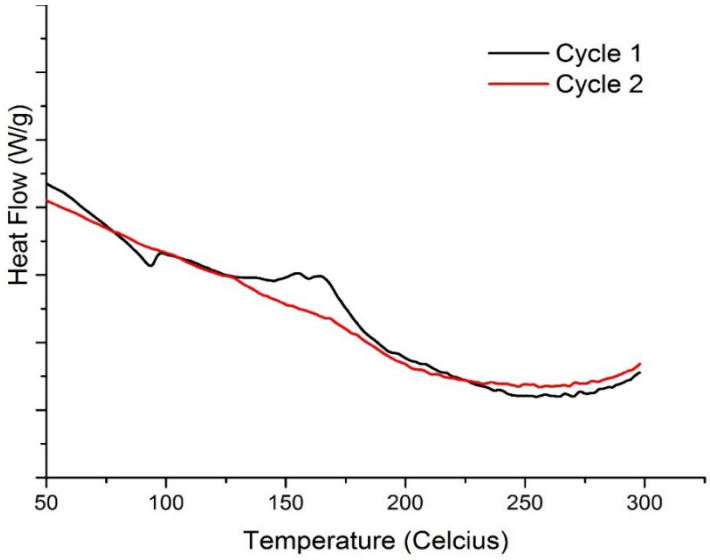

Figure 23. Curing exotherm of natural rubber

Table 4. Coupling Agents

	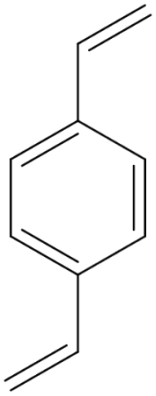	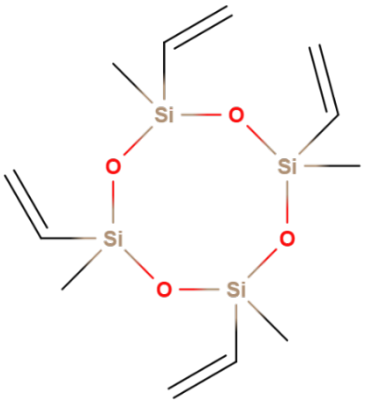	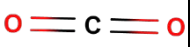
Mol. Wt.(g/mol)	130	345	44
Size (nm)	0.9	1	0.24

Further, the low molecular weight of these compounds enhances their solubility in $scCO_2$ for monomer transport into the subsurface voids created by the pre-treatment processes[70,71]. Thus, the pre-treatments enhance fiber surface and sub-surface area, and the soaks saturate the surface and sub-surface with the reactive monomers. Once the uncured rubber is brought in contact with this surface rich in reactive monomer, a higher crosslink density is expected in this region, producing an interphase. This interphase, showing a gradient in modulus from the interface to the bulk would provide mechanical interlocking (Figure 25), rather than a direct covalent bonding between fiber and matrix.

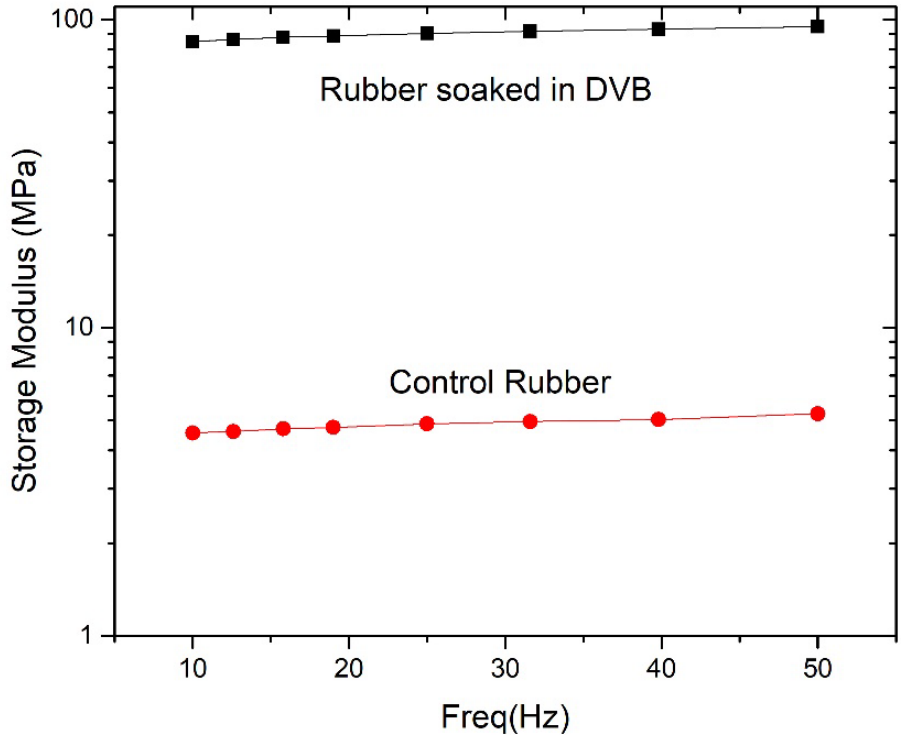

Figure 24. DMA on control rubber and rubber crosslinked with DVB

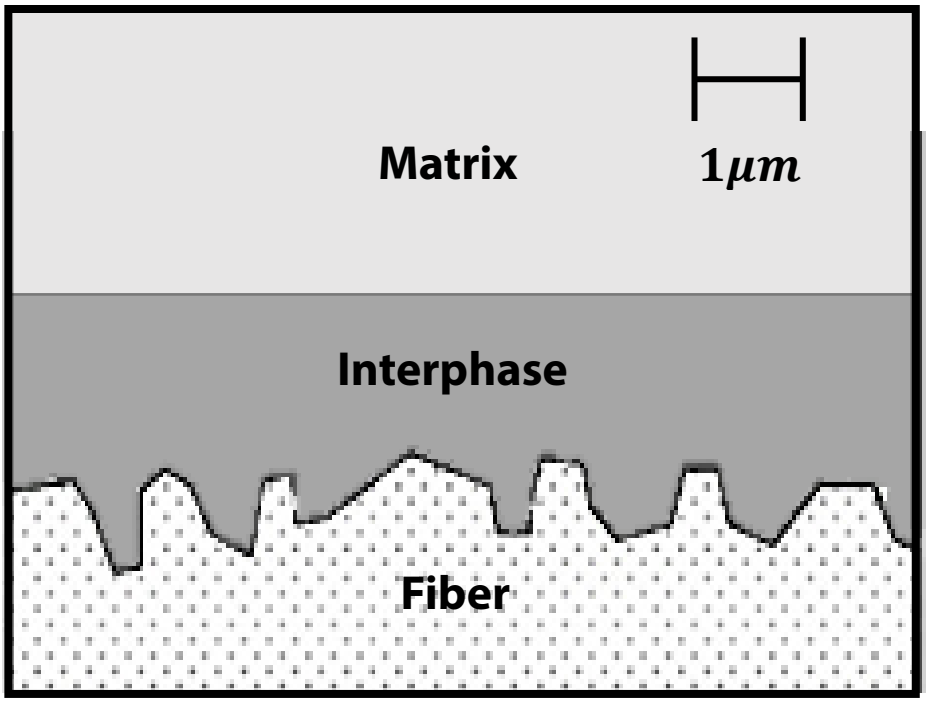

Figure 25. Schematic of a stiffer interphase, providing mechanical interlocking

To study the effect of the addition of reactive monomers on the properties of the matrix, a sample of rubber was first soaked in excess of DVB for a period of one hour over which significant swelling of the rubber was observed. This swollen rubber was subsequently cured using conditions similar to the that for making the composites and dynamical mechanical analysis (DMA) was done to study the effect of the coupling agent on the mechanical properties of the rubber. Comparative plots of the storage modulus obtained by dynamic mechanical analysis are shown in Figure 24. Note that a significant increase in both storage modulus and stiffness indicates that DVB most likely acts in an analogous way to sulfur and creates links between adjacent polymer chains to increases the crosslink density. More detailed chemical analysis like FTIR or NMR may be required to ascertain that.

Adhesion test design

A fiber bundle pull-out test was deemed the most direct way to evaluate the interfacial adhesion between the fiber and matrix. In order to ensure an appropriate embedded length necessary to generate a uniform shear stress at the interface, modeling of the fiber bundle pull-out test was done. A simple analysis of the shear forces acting on the interface can be done using a Kelly Tyson[72] approach (Figure 26). However, a fundamental assumption in the Kelly Tyson model is that the shear stress is uniform and constant along its length which is a factor that needs to be verified.

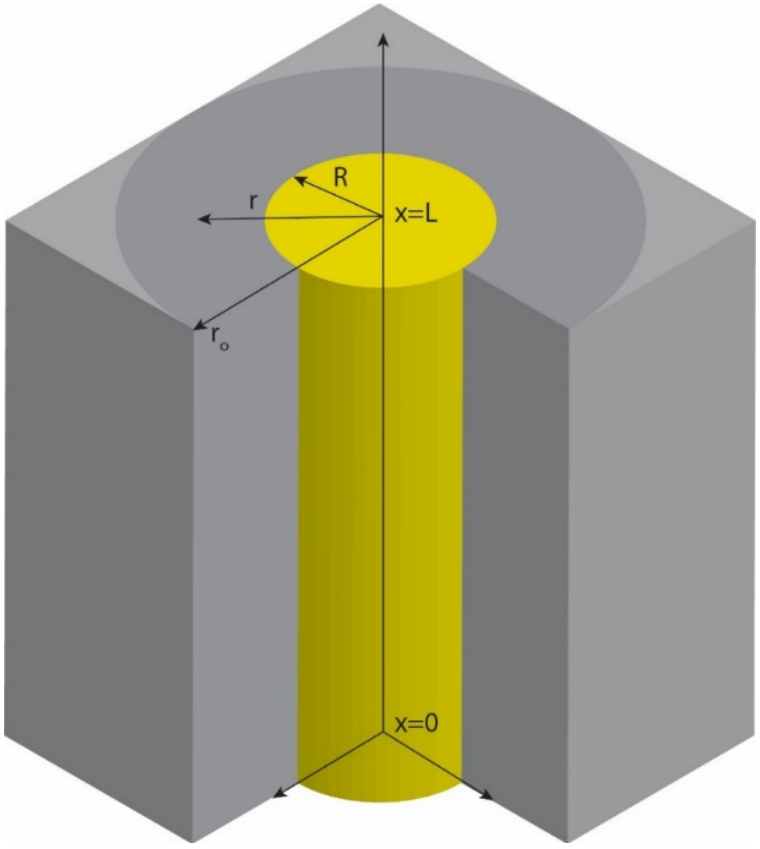

Figure 26. Cylindrical co-ordinate system for shear lag models showing fiber(yellow) embedded in rubber matrix

For simplicity, we approximate the fiber bundle as a single fiber of equivalent diameter and consider a more refined shear lag model similar to that introduced by *Cox et al*[73] and later developed by others[74–80]. These models take into consideration the moduli of the matrix and the fiber along with other geometric and boundary conditions to determine what the shear stress distribution is along the fiber bundle interface.

Table 5. Notation

F	Maximum pull out force
R	Radius of fiber/bundle
σ_0	Maximum tensile stress in fiber
$\sigma(x)$	Tensile stress in the fiber as a function of x
L	Embedded length
$\tau(x)$	Interfacial shear stress as a function of x
r	Arbitrary radius
r_1	Radius of Interphase region
r_o	Distance from fiber axis to tab surface
E_f	Young's Modulus of fiber
G_{m1}	Shear Modulus of interphase
G_{m2}	Shear Modulus of matrix
u_r	Displacement in x direction at radius r

First, we define a cylindrical co-ordinate system as in Figure 26. The notations are described in Table 5. A force balance on an annular region surrounding the fiber gives,

$$\tau_R . 2\pi R dx = \tau_r . 2\pi r dx$$

$$\tau_r = \frac{R}{r}.\tau_R$$

$$\frac{\delta u}{\delta r} = \gamma = \frac{\tau_r}{G_m} = \frac{\tau_R}{G_m}\left(\frac{R}{r}\right)$$

$$\int_{u_R}^{u_r} \delta u = \frac{\tau_R R}{G_m}\int_R^r \frac{1}{r}\delta r$$

$$u_r - u_R = \frac{\tau_R R}{G_m}\ln\frac{r}{R} \qquad (1)$$

Equation 1 describes the kinematic relation between displacement in the x direction as a function of the shear modulus of the matrix.

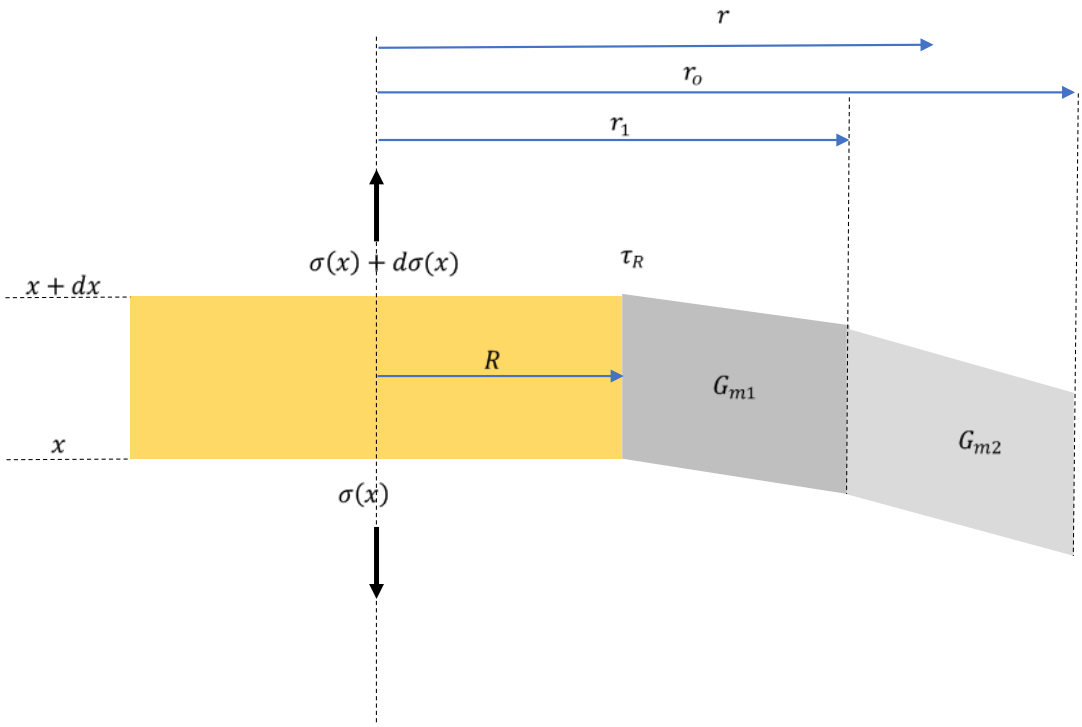

Figure 27. Fiber element of length dx

Applying a force balance on a fiber element of length dx as shown in Figure 27,

$$2\pi R\tau_R dx = -\pi R^2 d\sigma(x)$$

$$-\frac{2\tau_R}{R} = \frac{d\sigma(x)}{dx}$$

Substituting from Equation 1, we get,

$$\frac{d\sigma(x)}{dx} = \frac{2G_m(u_r - u_R)}{R^2 \ln\left(\frac{r}{R}\right)} \tag{2}$$

Differentiating Equation 2, we get a 2nd order ODE as in Equation 3,

$$\frac{d^2\sigma(x)}{dx^2} + \frac{n^2}{R^2}\sigma(x) = 0 \tag{3}$$

where

$$\frac{du_R}{dx} = \frac{\sigma(x)}{E_f}$$

and

$$n = \sqrt{\frac{2G_m}{E_f \ln\left(\frac{r_o}{R}\right)}}$$

Solving Equation 3, we get the distribution tensile and shear stresses as Equation 4 and Equation 5 respectively

$$\sigma(x) = \frac{\sigma_o \sinh\left(\frac{nx}{R}\right)}{\sinh\left(\frac{nL}{R}\right)} \tag{4}$$

$$\tau(x) = \frac{n\sigma_o}{2}\cosh\left(\frac{nx}{R}\right) cosech\left(\frac{nL}{R}\right) \tag{5}$$

For the two-stage shear lag model, displacement is alternatively defined as in Equation 6,

$$\int_{u_R}^{u_r} \delta u = \frac{\tau_R R}{G_m}\left(\int_R^{r_1} \frac{1}{r}\delta r + \int_{r_1}^{r} \frac{1}{r}\delta r\right) \tag{6}$$

Thus, we get an equivalent shear modulus defined in Equation 7,

$$G_{m_{eq}} = \frac{\ln\left(\frac{r}{R}\right)}{\left[\frac{\ln\left(\frac{r_1}{R}\right)}{G_{m1}} + \frac{\ln\left(\frac{r}{r_1}\right)}{G_{m2}}\right]} \quad (7)$$

This can be substituted in place of G_m to find the value of n which can then be used with Equation 3.

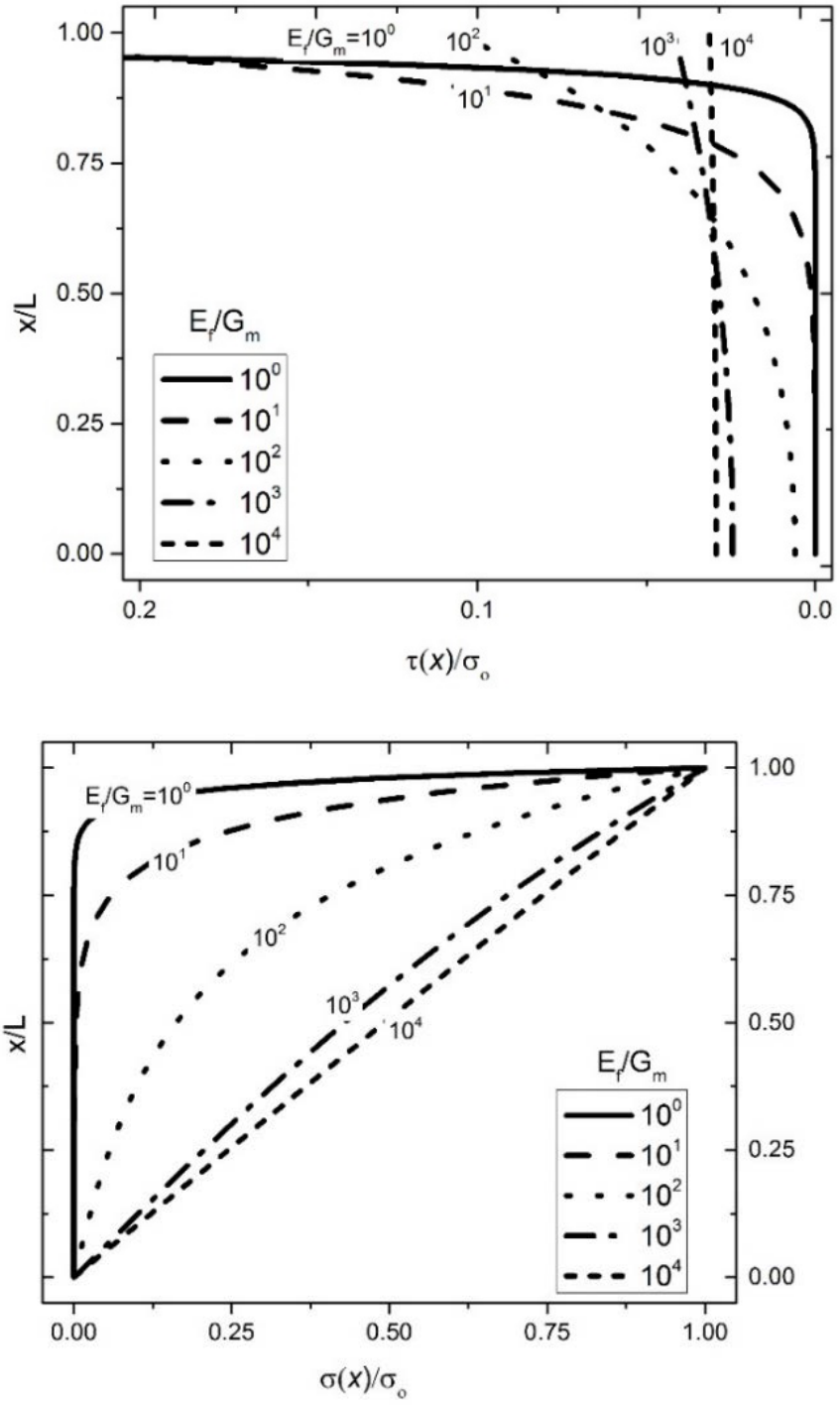

Figure 28. Tensile and shear stresses on the fiber plotted for various values of E_f/G_m over the normalized embedded length.

The predictions of the tensile stress and shear stress distributions as a function of embedded distance normalized by embedded length (*x/L),* and ratio of the fiber tensile modulus to matrix shear modulus are plotted for various values of $(\frac{E_f}{G_m})$ in

Figure 28. The results show that as the modulus of the matrix drops in comparison to the fiber, the stress distributions move from a hyperbolic to a more linear behavior. That is, the predictions of the more advanced shear lag model and that of the Kelly-Tyson model converge and the modulus mismatch increases. More importantly, for our case, the shear modulus of the rubber in our system is at least four orders of magnitude smaller than the tensile modulus of PPTA fibers. Consequently, we can be assured that the shear stress distribution is uniform for our embedded length of 10 mm and can be calculated from the following relation.

$$\tau(x) = \frac{\sigma_o R}{2L}$$

3.3.3. Adhesion Tests

Fiber matrix adhesion tests were performed on control and treated fibers with an embedded fiber bundle length of 10mm. Figure 29 shows the results for control fibers (without any pre-treatment) conditioned with each reactive monomer that was infused using $scCO_2$ and under ambient conditions.

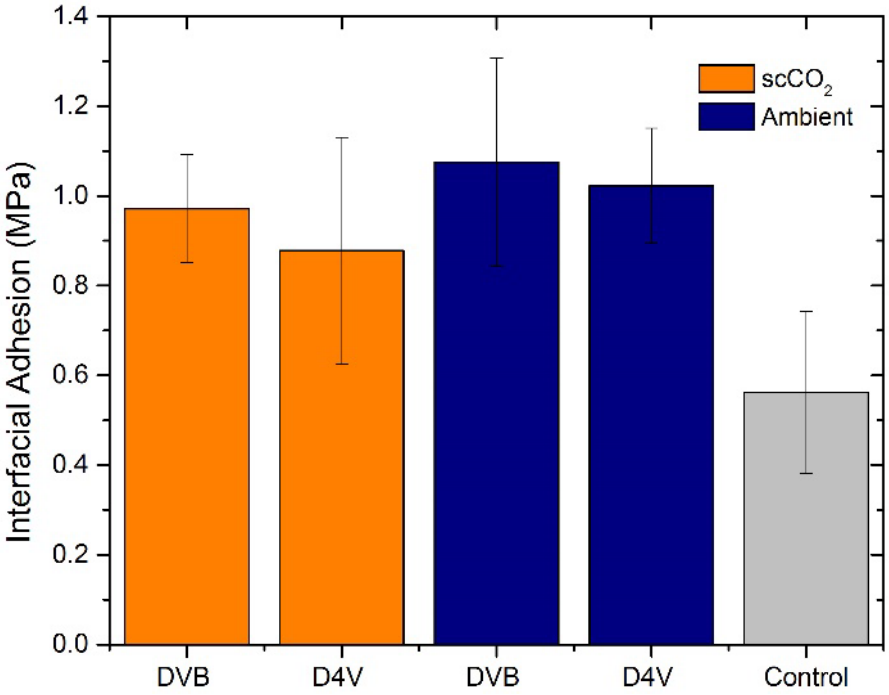

Figure 29. Adhesion of control fibers treated with different reactive monomers.

The results indicate that both DVB and D4V improve the adhesion by about a 100%. DVB in general seems to provide better adhesion that D4V. However, the impact of $scCO_2$ on the adhesion cannot be ascertained from these tests. Further studies would be needed to get a better understanding of this.

Additional adhesion tests were performed on the fibers that were first subjected to either the microwave or mechanical pre-treatment. For these tests, the fibers were subsequently treated with DVB as the reactive monomer since it showed the best results. The results from these adhesion tests are shown in Figure 30, with the error bars representing the standard deviation of measured adhesion. The results suggest that both pre-treatments enhance adhesion of the fibers to the matrix, however more detailed tests are required to isolate the effects of each pre-treatment.

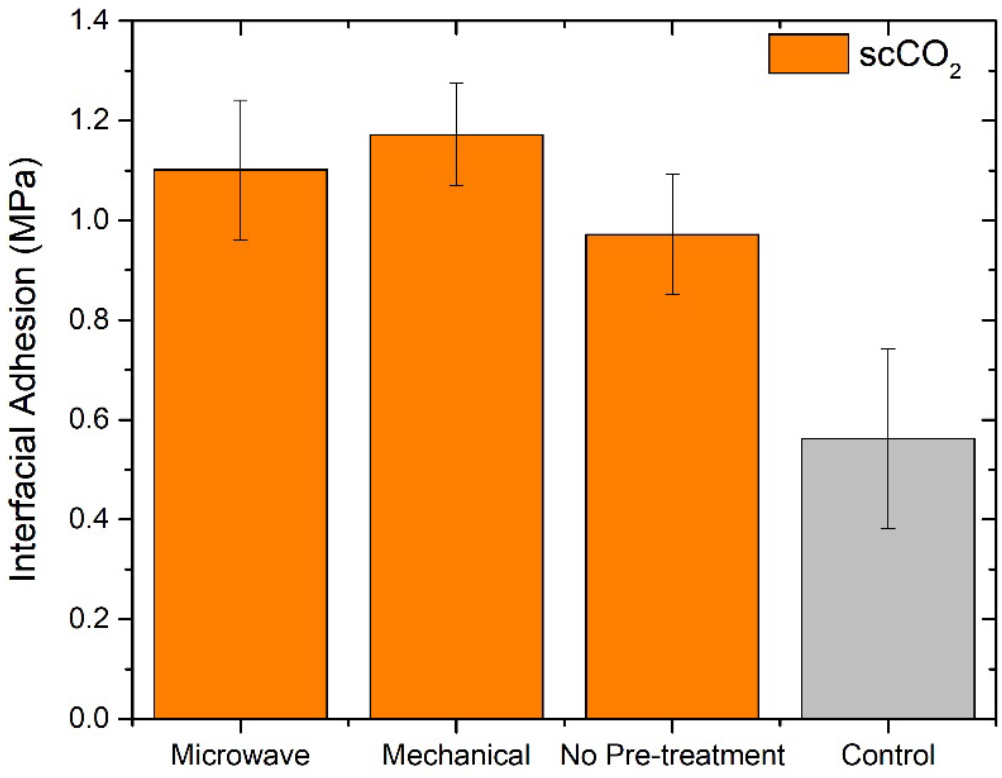

Figure 30. Effect of pre-treatments on adhesion. (Coupling agent: DVB)

After the adhesion tests were completed, the fiber bundles were examined using a Scanning Electron Microscope (SEM) to evaluate the mode of failure. Results from this investigation are shown in Figure 31.

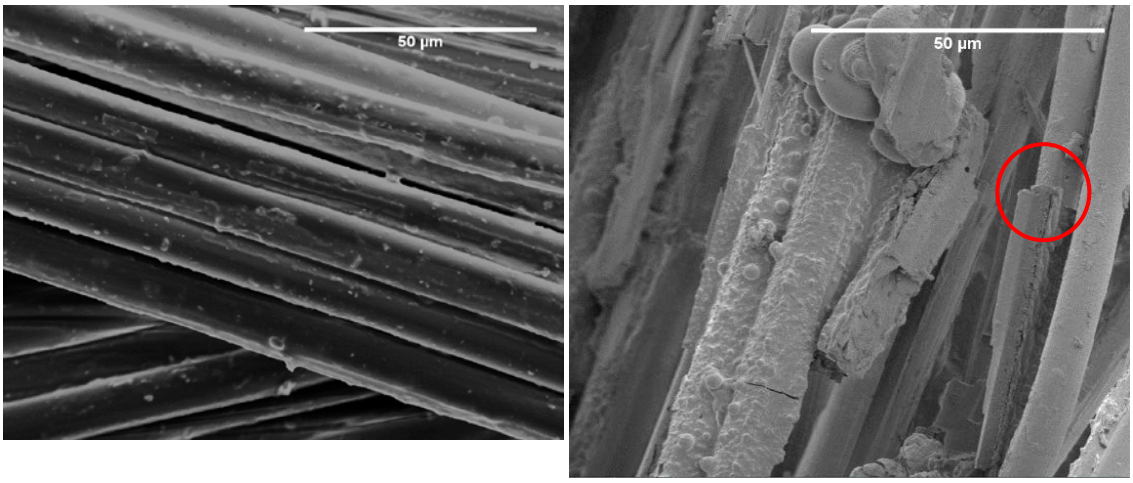

Figure 31. Failure interface of control (left) vs treated fiber indicate a suppression of interfacial failure after treatment. (fractured fiber encircled)

Note in Figure 31 that the control fibers are bare, with very little or no rubber adhering to the fiber surface, indicative of poor adhesion. In contrast, the fibers treated with DVB (no pre-treatment) in the presence of $scCO_2$ show rubber adhering to the fiber, indicating a departure from interfacial failure to fracture of the rubber matrix. In addition, some fractured fibers are also visible, indicating that the strength of the fibers is being utilized to a greater extent to improve composite strength. This image provides evidence for the creation of the interphase region that may have a higher local crosslink density than that of the rubber away from the fiber. This interphase region with increased crosslink density is obtained from the reactive monomers infused into the fibers.

3.3.4. Two-Stage Modification for Interphase Region

Although more detailed studies beyond the scope of the current investigation would be required to characterize this interphase region, the Cox shear-lag model can be easily extended to accommodate this stiffer interphase region. For this analysis, we consider an annular interphase region beginning at the fiber interface to an intermediate radius r_1

between the fiber radius R and the distance between fiber axis to tab surface r_o having a modulus higher than that of the bulk. Assuming the interphase to have a modulus of G_{m1} and the bulk to have a modulus of G_{m2}, an equivalent shear modulus can be defined as in Equation 7.

For an interphase region having an E_f/G_{m1}=10^1 and a bulk having an E_f/G_{m2}=10^2, the predictions are plotted in Figure 32. The results are compared to single stage models with bulk moduli having the ratio E_f/G_{m1}=10^1 and E_f/G_{m2}=10^2.

The two-stage model predicts that the decay of shear stresses with embedded length are more severe as compared to a system with no stiffer interphase region. This modification is highly simplified as it assumes a step change in modulus from the interphase to the bulk. This can be extended to include more than two phases to better explain systems that have a more gradual change in properties from the interface to bulk.

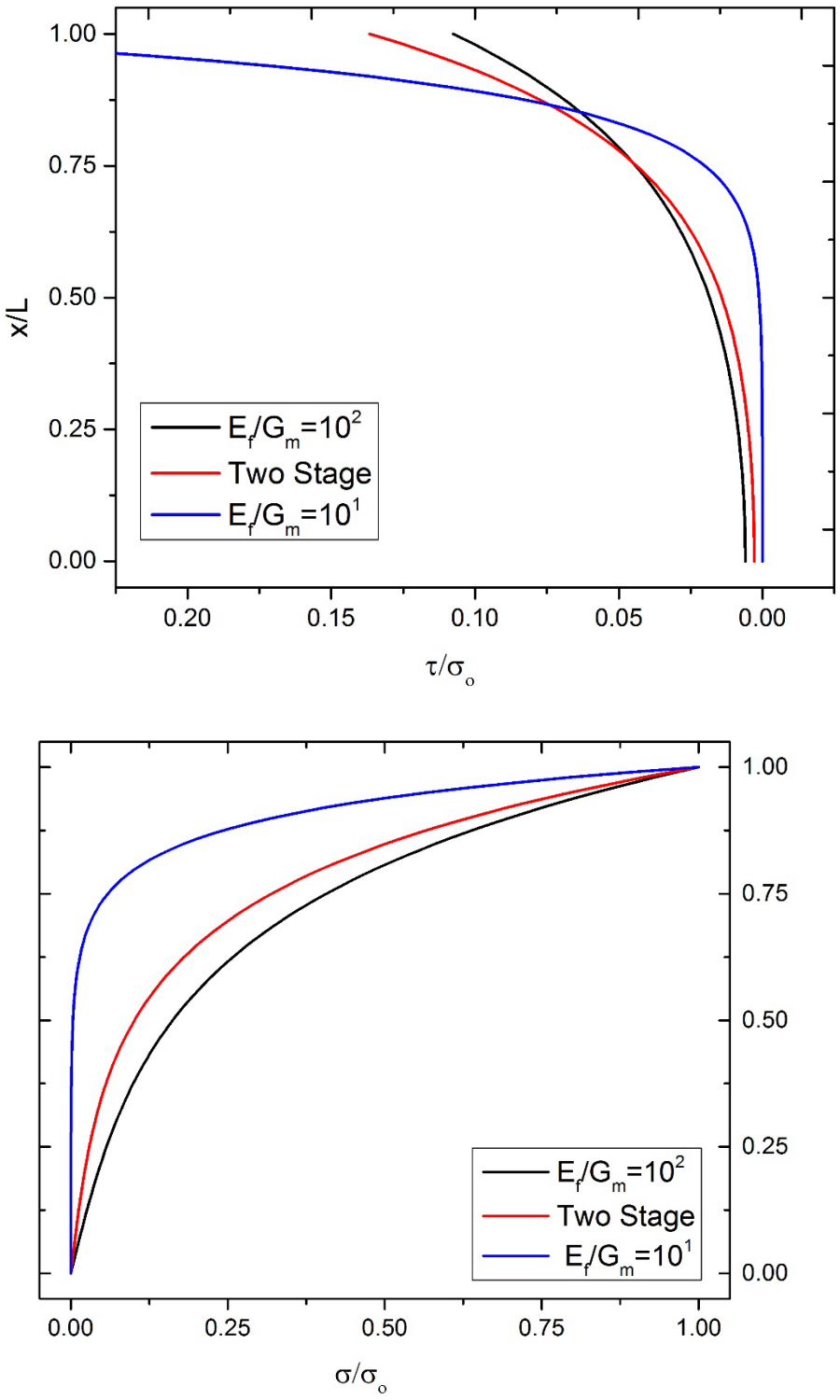

Figure 32. Two stage model predictions of shear(top) and tensile stresses

Model System to Study Two Stage shear lag Predictions:

To correlate the predictions of the two-stage system with experimental data, we used an epoxy-based system as a model to simulate a fiber pull-out test in a composite with a stiffer interphase. To simulate the hard phase, an aromatic epoxy system with 4-aminophenyl sulphone as the amine and bisphenol A diglycidyl ether DGEBA as the epoxy was used, whereas to simulate the softer phase, a polyetheramine and a polydimethyl siloxane-based epoxy, both with aliphatic backbones were used. A galvanized carbon steel wire was used as the fiber to be pulled out of the matrix system (Figure 33). The method for fabricating the fiber pull-out test specimen is shown in more detail in

Figure 34.

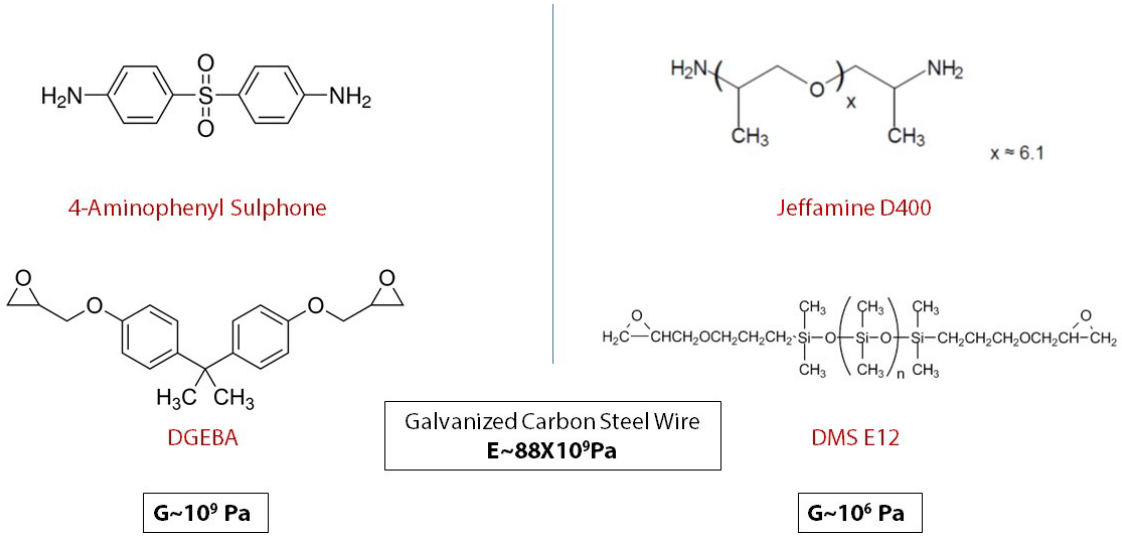

Figure 33. Epoxies with higher and lower modulus at room temperature, along with the galvanized steel wire, shown with their respective moduli.

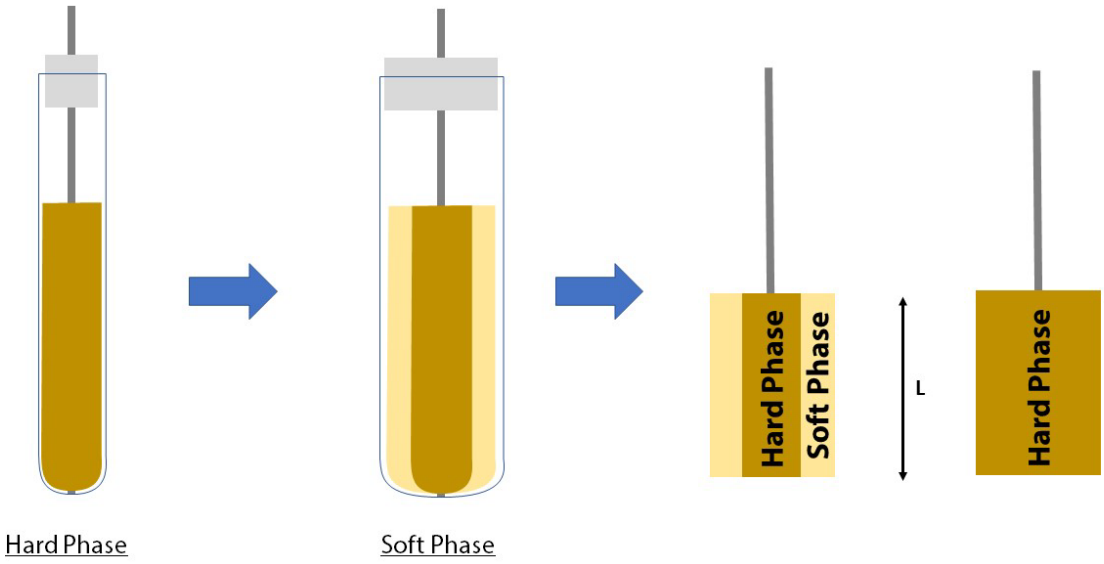

Figure 34. Fiber pull-out test specimen fabrication

The shear stress predictions of the two-stage model as compared to a single-stage model fabricated from the hard phase is shown in Figure 35.

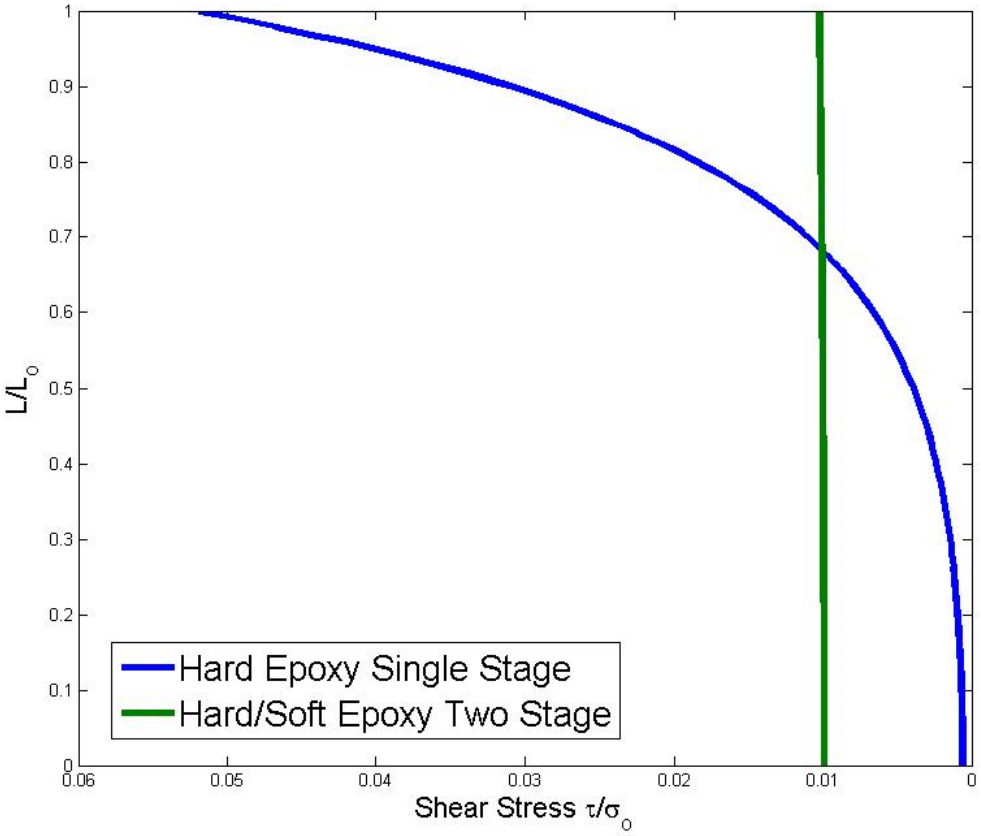

Figure 35. Predictions of single and two stage models

The model for the hard epoxy phase predicts that the shear stresses are parabolic, with maximum stresses at the top where the fiber enters the matrix, gradually dropping down to zero towards the bottom. The predictions for the specimen with the interphase shows that the shear stresses are uniform through the embedded length. From this, one would expect that the pull-out force for the hard epoxy system would initially increase with embedded length, and then gradually level-off as the shear stresses approach zero. Whereas for the two-stage system, since the shear stresses are uniform through the embedded length, one

would expect the pull-out force to increase linearly with embedded length. The pull-out force vs embedded length for both the single stage and two-stage follow these expected trends as shown in Figure 36 and Figure 37.

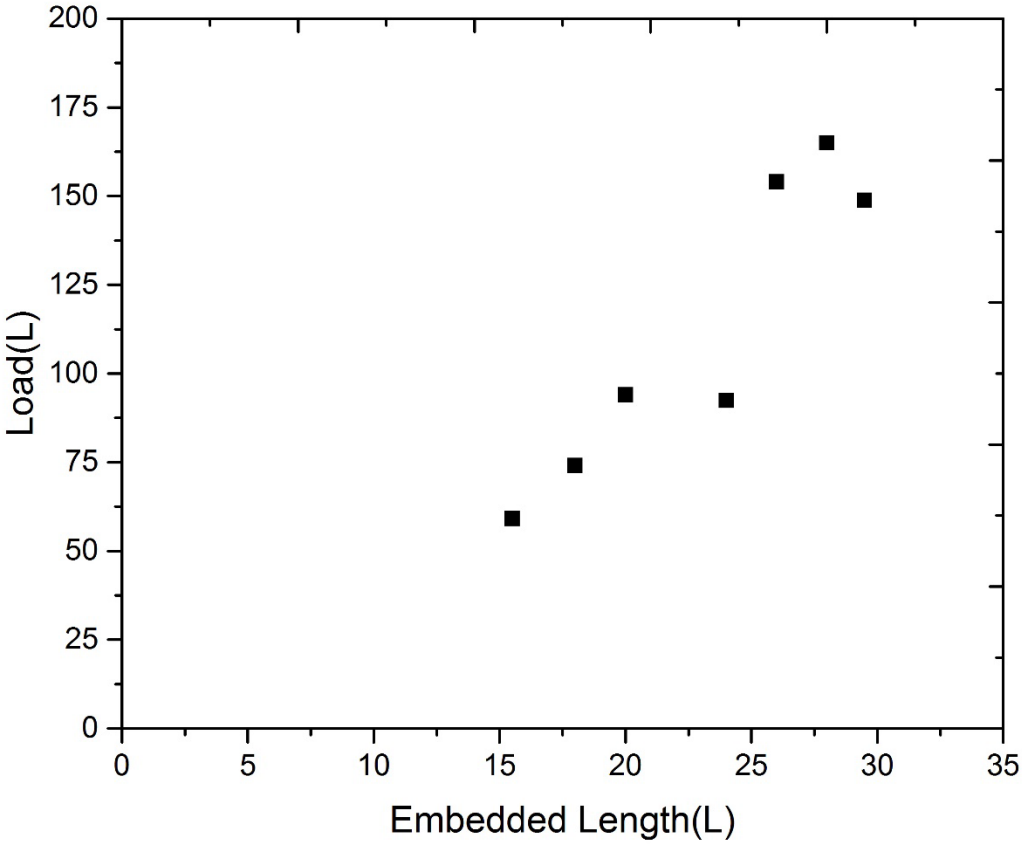

Figure 36. Load vs Embedded length for two stage system with interphase

Figure 36 shows the results for the two-stage system, with the pull-out force showing an increasing linear trend with embedded length. The hard epoxy single-stage system shows

a hyperbolic trend, where the load increases initially but then seems to remain constant with increasing embedded length.

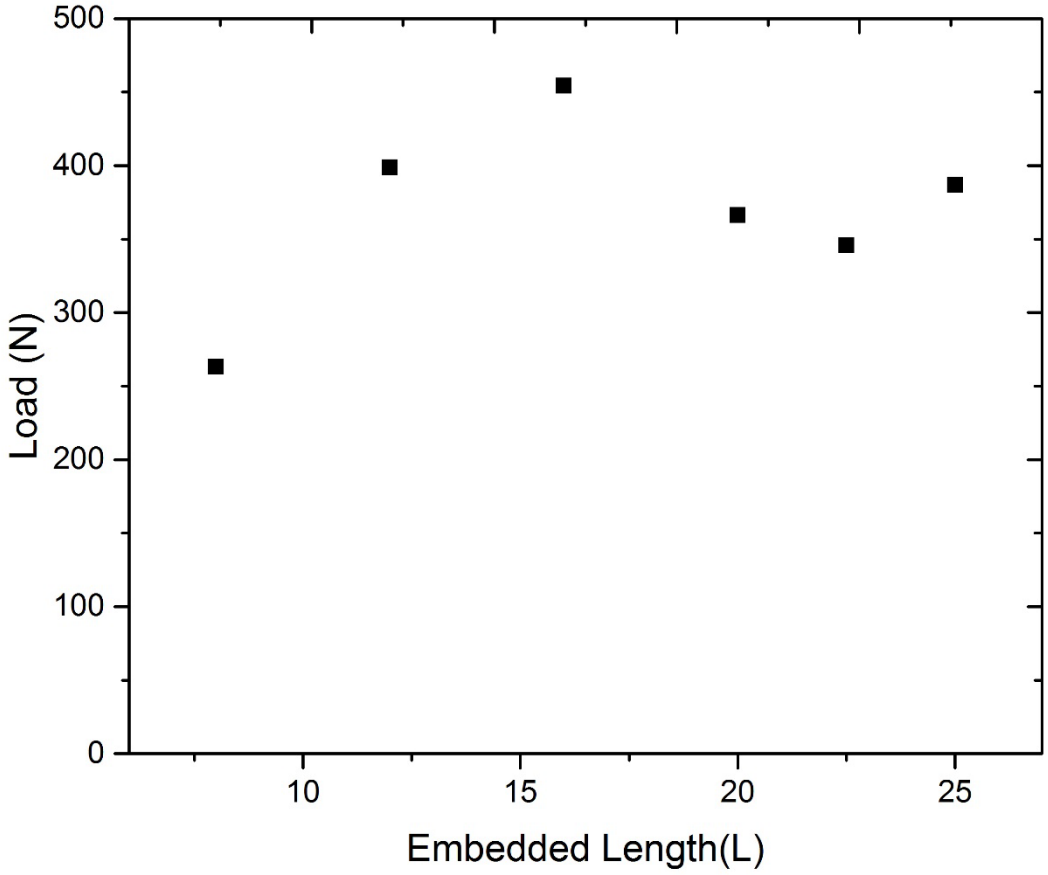

Figure 37. Single stage hard epoxy system

These studies to verify the two-stage model were performed on epoxy systems with known dimensions and moduli instead of the PPTA-rubber system, since determining the interphase dimensions and properties of our current system is complicated and time consuming. Further detailed studies would be to directly or indirectly evaluate the stiffness and strength profile radially outward from the fiber center through the interphase region

and into the matrix. This may involve a range of advanced experimental techniques and modeling studies.

3.4. Conclusions

This research has shown that the adhesion between PPTA fibers and natural rubber can be effectively doubled through a combination of fiber pre-treatments and infusion of reactive monomers. New fiber pre-treatments including a microwave and mechanical treatment are introduced with each showing unique alteration in the fiber morphology that enhances monomer permeation and fiber-matrix adhesion. These pre-treatments are followed with an infusion of the fibers with two reactive monomers D4V and DVB to provide superior adhesion. Immersion or soaking of the fibers with monomers in the presence of $scCO_2$ to enhance transport was found to have a negligible effect. Shear lag analysis was used to evaluate the test method and the geometrical parameters of the fiber-pull out adhesion test. The results of the adhesion tests show that the coupling agents are the major contributor to the improvement in adhesion, leading to an almost 100% improvement in adhesion. Microwave and mechanical pre-treatments are found to be secondary contributors to adhesion leading to a 10% and 20% improvement in adhesion respectively. Failure analysis indicates a shift of failure mechanism and a suppression of interfacial failure. There is also an indication of the formation of an interphase region surrounding the fiber. Finally, a two-stage modification for the shear lag model is proposed to take into account the presence of the interphase region.

Acknowledgement and Copyrights

The above research was funded by Bridgestone of America and is part of a patent[56]*. (https://patentscope.wipo.int/search/en/detail.jsf?docId=WO2017031308)*

Passages and figures have been republished with permission from Wiley 2017[81]

doi.wiley.com/10.1002/app.45520

CHAPTER 4

CELLULAR STRUCTURES FROM ANISOTROPIC SEMI-CRYSTALLINE POLYMER TEMPLATES

4.1. Introduction

Synthetic polymer-based cellular materials are widely sought today as alternatives to natural cellular materials such as balsa wood. Balsa wood is extensively employed for a variety of structural applications such as sandwich panels in the cores of the blades of wind turbines. It is one of the strongest cellular material found in nature with high specific strength and energy absorption characteristics[82]. This has been partly attributed to the morphology of its cellular structure[83]. The cells of balsa wood are highly anisotropic; they are long, slender and elongated in the axial direction of the wood, giving it anisotropic mechanical properties. Also, the material of the wood itself is a composite of semi-crystalline cellulose (primary strength provider), hemicellulose and amorphous lignin. A synthetic foam with comparable properties would need two characteristics: a high semi-crystalline component and an anisotropic cellular structure.

Most semi-crystalline materials are inherently difficult to foam[12–14]. One approach to overcome this problem is to combine a semi-crystalline and amorphous polymer to create a blend, to improve its foamability[84–86]. Conventional methods like melt mixing have been used for this purpose. However, this can lead to uneven foaming and poor mechanical properties if miscibility is poor between the two phases. Much finer blending on a molecular level can be achieved with supercritical carbon dioxide ($scCO_2$) to create kinetically trapped composites[87,88]. $ScCO_2$ is an excellent solvent for small molecules and this property has been exploited to create composites with improved mechanical properties[87,88]. The solvent properties of $scCO_2$ are a function of temperature and pressure;

thus these parameters can be tuned to achieve desired solvent strength. Semi-crystalline and amorphous polymers are used as substrates, and a monomer (such as styrene) and free radical initiator are allowed to diffuse into the substrate assisted by $scCO_2$, and subsequently allowed to polymerize. Polymerization leads to partition and phase separation since $scCO_2$ is a weak solvent for most polymers[89–94] (except for certain fluoropolymers and silicones) leading to the formation of the kinetically trapped composites. $ScCO_2$ has also been extensively used as a foaming agent to create microcellular polymer foams[95–97]. It has relatively mild supercritical conditions (T_c=31.1ºC, P_c=1070 psi) and is also nonflammable, nontoxic and relatively inexpensive.

These properties have been exploited in conjunction with high Tg amorphous polymers as templates to create hierarchical foam structures.

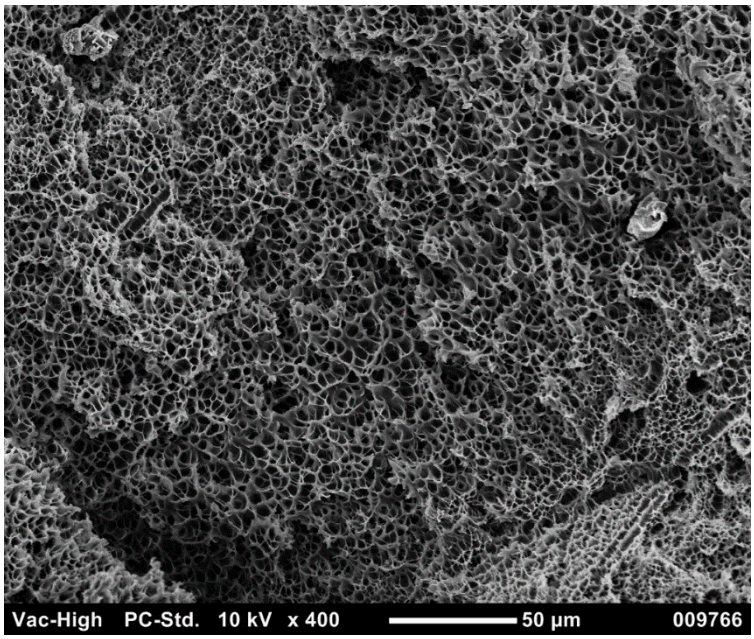

Figure 38. Polyether sulfone foamed above its Tg

For example, using a high Tg polymer such as poly ether sulfone, we can create a conventional foamed structure by saturating it with $ScCO_2$, taking it above the glass

transition temperature and subsequently depressurizing. One can also use this PES foam as a template to polymerize and foam a second phase (in this case polystyrene) within it to create a cellular structure with a hierarchical distribution of cell sizes, with nanometer sized cells within the larger micron sized cells.

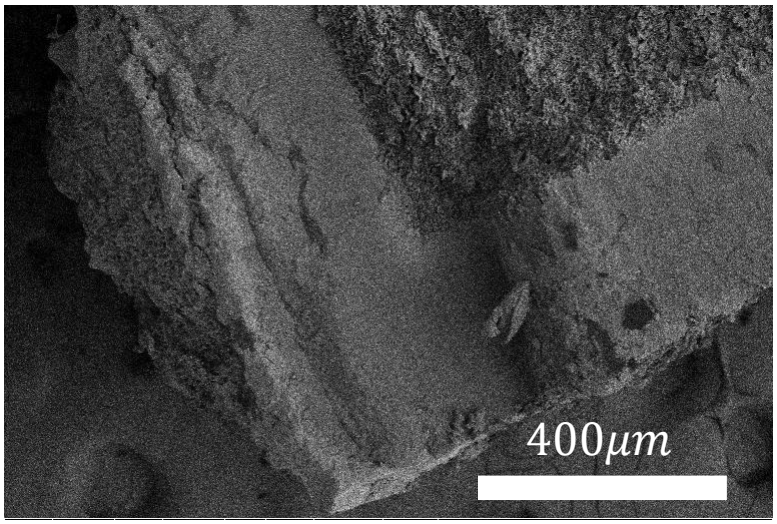

Figure 39. Distinct boundary region is seen on the corner of the cross section of a square sample

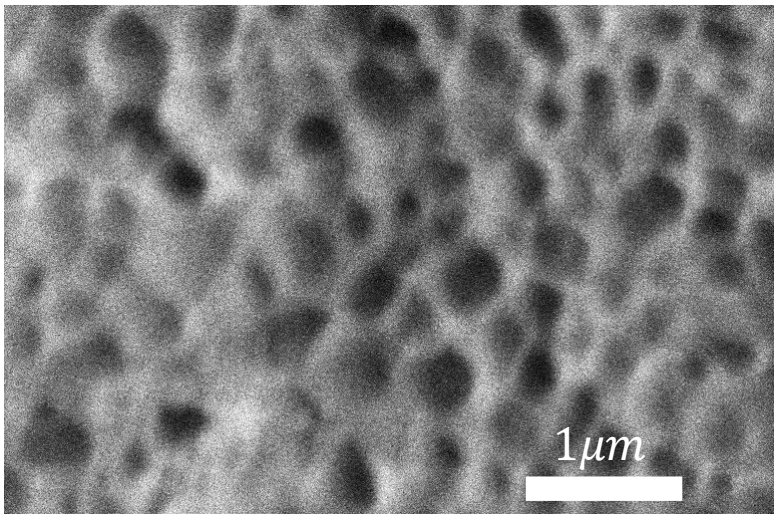

Figure 40. Nanometer sized cells in the outer periphery

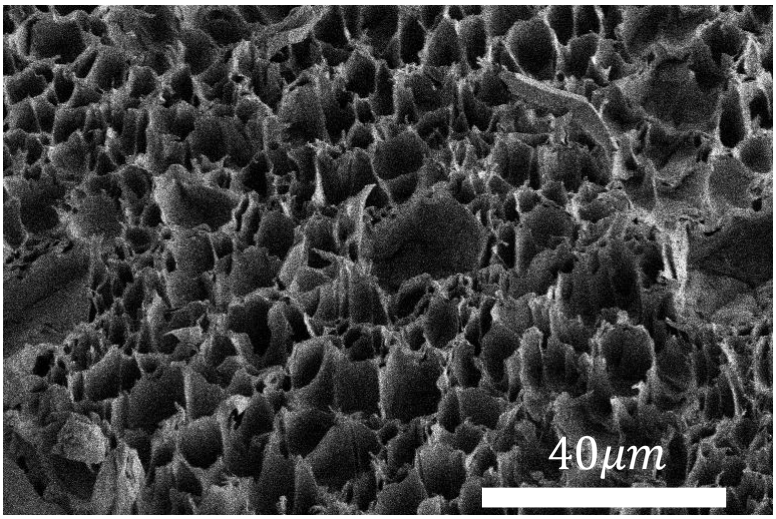

Figure 41. Micron sized cells in the core.

This suggests that the confinement effect of the larger cells during depressurization led to the formation of smaller nanometer sized cells in the polystyrene phase.

The issue probed in this research was to ascertain whether the inherent molecular anisotropy in a semi-crystalline substrate can play a role or dictate the final morphology of cells in a composite foamed with that substrate. Traditional methods use confinement to control the direction of expansion[97] and introduce anisotropy in foams. This investigation aimed to devise a facile, in-situ process or method to achieve anisotropic cells without the use of external confinement. The final morphology of cells in the amorphous component of a blend may be governed to some extent by the anisotropy of the crystalline component of the template. Anisotropic cellular materials that mimic balsa wood can potentially be created by using the inherent anisotropy of crystals in systems such as films and filaments. For this reason, two anisotropic templates were chosen, a uniaxially oriented polyamide-12 (PA12) filament and a biaxially oriented polyethylene terephthalate (PET) film. Kinetically trapped composites were created using the process described above and their compositions determined. These composites were subsequently foamed, and the cell

morphologies were studied. Typical relaxation mechanisms of polymer chains are expected to occur above the T_g that could prevent the cellular structure from being templated by the crystals of the anisotropic templates. Mechanical tests were performed on certain composites to gauge the strength and modulus. Finally, alternative methods to introduce anisotropy were suggested that combine the templating phenomena observed and confinement to give highly anisotropic cell morphologies.

4.2. Experimental

Polyamide 12(PA12) filaments of a diameter of 500 microns and polyethylene terephthalate (PET) film with a thickness of 200 microns were obtained from McMaster Carr and used without any modifications. The PET film had a density of 1.25 g/cm^3, melting temperature of 250°C and a crystallinity of 33%, assuming the enthalpy of melting of a PET crystal to be 125.6J/g.[13]. The PA-12 filament had a density of approximately 1g/cc and a melting temperature of 190°C and a crystallinity of around 33% assuming the melting enthalpy of a 100% PA-12 crystal to be 209.2J/g [98]. Carbon dioxide of Coleman grade purity was obtained from Airgas and used as is. Styrene monomer and thermal initiator tert-butyl peroxybenzoate (TBPB) were obtained from Sigma Aldrich. Styrene was passed through a column of aluminum oxide for purification before use.

4.2.1. Composite Synthesis and foaming

Strips of PET film were cut into rectangles having dimensions of approximately 7 X 70 mm. PA12 filaments were cut to a length of 70 mm. A *soak-polymerize* procedure was performed on the PA-12 filaments and PET films to create the respective composites with polystyrene. The schematic of the setup is shown in Figure 42.

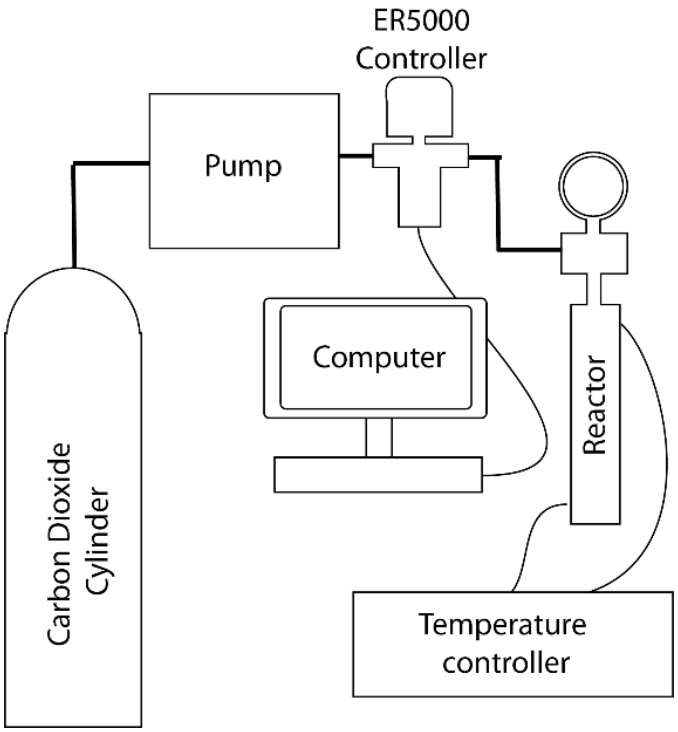

Figure 42. Schematic of the foaming setup

Test tubes were filled with an excess of styrene mixed with the initiator. These test tubes were then placed in specially designed high-pressure reactors. A high-pressure pump (Supercritical Fluid Technologies) was used to pump carbon dioxide to pressures of 5000 psi. For the *soak* step, the temperature was initially set to 60ºC by wrapping the reactors in heating tape (Omega engineering) with a thermocouple placed inside the reactor to accurately monitor temperature conditions. The TBPB initiator which was used to polymerize styrene is a thermal radical initiator, its reactivity growing with temperature which depends on the half-life of the initiator.

The half-life $t_{1/2}$ can be calculated using the Arrhenius equation[99,100].

$$K_d = Ae^{-\frac{E_a}{RT}} \quad (8)$$

$$t_{\frac{1}{2}} = \frac{\ln(2)}{K_d} \tag{9}$$

with K_d the rate constant for the initiator dissociation[1/s], A the Arrhenius frequency factor [1/s], E_a the activation energy [J/mol], R the universal gas constant [J/mol K] and T the temperature [K]. For TBPB, $A = 2.23 \cdot 10^{16}/s$ and E_a = 151.59 kJ/mol. At 60ºC the polymerization is negligible with a half-life of 216 days, while still being above the critical temperature for CO_2. Soak was performed at this temperature for 24 hours with the aim of swelling the substrate with monomer and initiator. This temperature was found to be above the Tg of PA12 (41°C) but below the Tg of PET(81°C). However, swelling was observed in both cases, suggesting that there might be a drop in the glass transition temperature in the presence of $scCO_2$, a phenomena that is well documented[101]. After this stage, the temperature was raised to 100ºC and the polymerization process was initialized, since the half-life at this temperature is approximately 15 hours. Since $scCO_2$ is a weak solvent for polymers, styrene polymerizing to polystyrene undergoes phase separation and crashes out of the solution to get deposited within the template, opening the path for more styrene to diffuse into the system. To obtain a large enough molecular weight of polystyrene, a 0.3-99.7 mole % TBPB-styrene ratio was taken. Polymerization was carried out for a period of 24 hours as well. Once this was done, foaming was initiated by depressurization leading to nucleation and growth of cells. A TESCOM sourced computer controlled ER5000 pressure regulator was used for precise depressurization. Instantaneous depressurizations were carried out to induce foaming, while slower depressurizations were carried out to suppress it. Optimum foaming temperatures were found to be 190°C in the case of polyamide composites and 100ºC in the case of PET composites.

4.2.2. Characterization

Various characterizations were performed on the composite foams to determine their properties. The density was calculated by the volume displacement method using a pycnometer. Differential scanning calorimetry (DSC) was done using a TA Instruments Q200 to measure the glass transition temperatures and melting endotherms, the latter of which was used to calculate the weight percentage PET in the foams. A heat/cool/heat cycle was performed done over the range of 0°C to 300ºC. Thermogravimetric analysis was performed on TA Instruments Q50 TGA. For measuring the complete thermal degradation, the foams were heated up to 600°C. Qualitative characterization of the composite foams was done by infrared spectroscopy on a Perkin-Elmer 2000 FTIR by comparing the absorption peaks in the templates as well as the final composites. The microcellular structure of the foams was also observed by fracturing the sample after immersing in liquid nitrogen (to maintain the cell structure) and using Scanning Electron Microscopy (SEM), an FEI Magellan XHR 400L FE-SEM at 1kV. Wide angle X-Ray scattering was performed by a Ganesha SAXS-LAB instrument. Mechanical behavior was studied on certain specimens by doing four-point bending tests on an Instron 5500R tensile testing machine.

4.3.Results and Discussion

4.3.1. Foaming of templates

Processing conditions play a crucial role in dictating the cell size and structure[95,96,102,103]. One of the most direct ways to control cell size is by controlling the processing temperature. Initially, control PA-12 filaments were subject to a conventional foaming procedure at

190ºC. Semi-crystalline polymers must be foamed at temperatures above their melting temperatures to get foams since the crystallites are too rigid below this temperature. Above the melting temperature, foaming is usually homogenous and much like an amorphous polymer above its glass transition temperature. However, one cannot go much higher above the melting since this will lead to uncontrolled growth and a subsequent collapse of the cell structure. The foaming temperature was thus chosen carefully such that it was above the melting temperature of the crystallites, but low enough that the filament maintained its structural integrity, and uncontrolled expansion and foaming are not initiated[12]. The filaments were allowed to saturate for a period of 1 hour and thereafter a quick depressurization was initiated to create a foam. The filaments were fractured after immersing in liquid nitrogen; a diagonal cross section was obtained and imaged as shown in Figure 43.

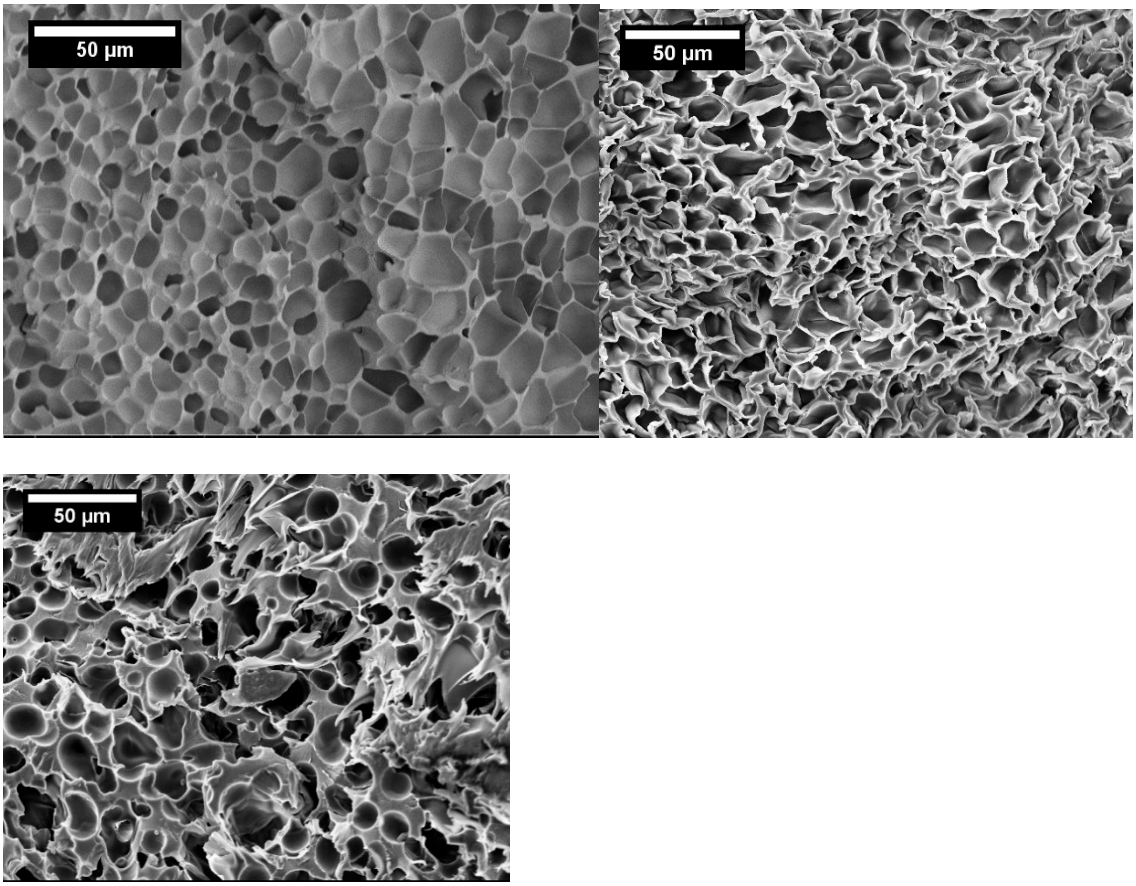

Figure 43. a) Diagonal and b) transverse cross sections of foamed PA12 and c) transverse cross section of PET foam showing isotropic cell structure

The images point to a close celled structure and the cells are uniform in size, structure, and distribution with an average cell size of 25 microns. The diagonal section in Figure 43 indicates that the cell structures are isotropic in nature and not oriented in the direction of the filament axis. Additionally, a skin layer was observed on the surface of the filament. The diameter of the filament increased to around 1200 microns, while the length decreased to around 40% of the original length. This indicates that at these elevated temperatures, the filament loses its anisotropy and relaxes back to an isotropic state. Foaming of PET films at a temperature of 250°C leads to complete melting and collapse of the film structure, giving isotropic cells (Figure 43.c).

4.3.2. Synthesis and Foaming of blends

Both templates were subjected to the soak polymerize procedure wherein styrene monomer and initiator were allowed to diffuse into and swell the substrate, as explained in the experimental section. After this procedure, the diameter of the PA12 filament increased to 1700 microns from an initial diameter of 500 microns (Figure 44).

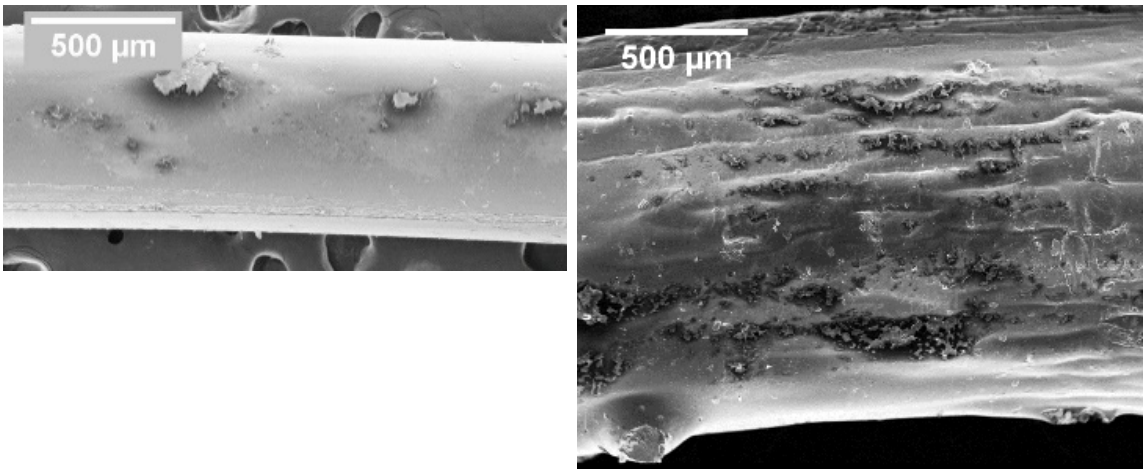

Figure 44. PA12 filament before (left) and after soak-polymerize procedure

The blend was then subject to a foaming procedure at a temperature of 190°C for a duration of one hour. The final diameter of the composite foam was observed to be close to 2400 microns with a density of 0.3g/cc. The strips of PET films were placed in test tubes along with styrene and initiator, and the soak-polymerize procedure and foam procedure were performed. An example of what the final blend foam looks like is shown in Figure 45. The final foam has the same rectangular initial shape as the PET film template. However, the change in dimensions indicate a highly anisotropic nature of swelling, with a substantial change in height by a factor of 25 in the case of the foam in Figure 45. Polymeric films are usually processed by blow molding, and high biaxial stretching and anisotropy are introduced into the film in the length and width direction. Thus, once the polymer is raised above its glass transition or melting temperature, it tends to relax in the thickness direction, potentially giving greater mobility and ability to expand in that direction.

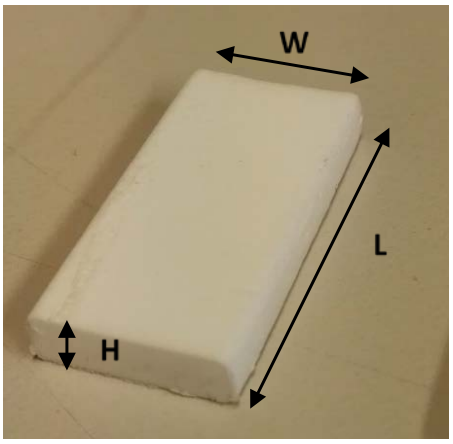

	Change in Dimension (α)
α_W (Width)	2.4
α_L (Length)	1.2
α_H (Height)	25

Figure 45. PET-PS composite, change in dimensions

By controlling the amount of styrene available in the reactor, different ratios of swelling were achieved. For each of these composites, the greater the swelling in the thickness direction, the lower is the density. Therefore, if the density vs dimension change α, a linear trend is observed as shown in Figure 46.

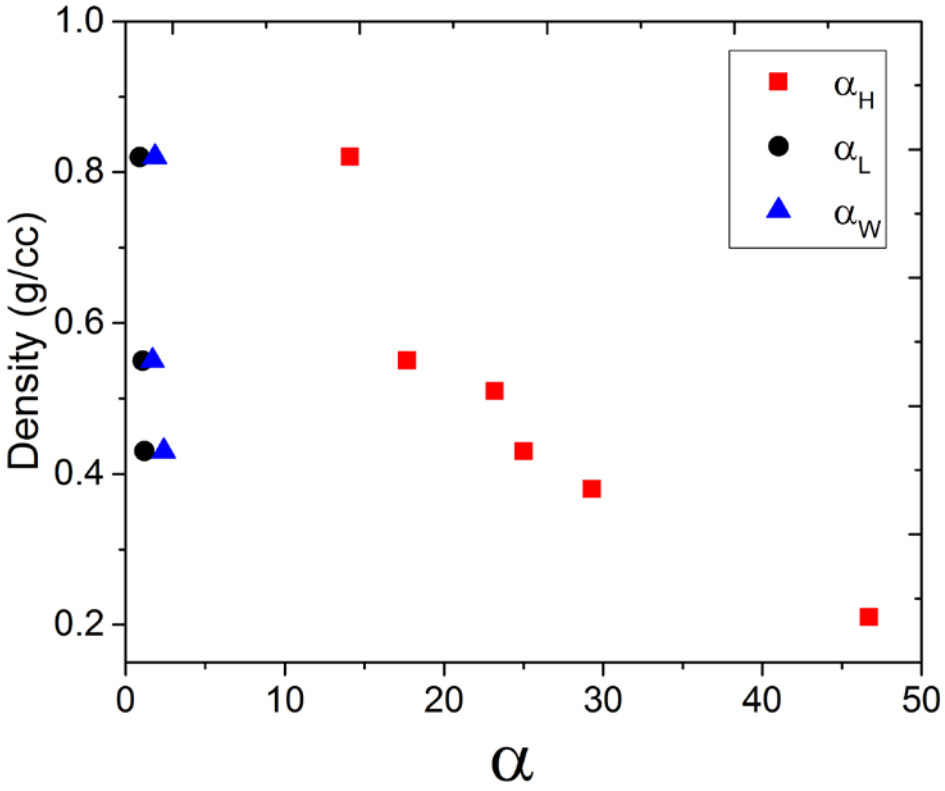

Figure 46 . α vs density

The changes in other dimensions stayed approximately the same.

4.4.Characterization

4.4.1. Cell Morphology and Orientation

A transverse cross section was taken and observed under the SEM. The images revealed a unique radial gradient in cell morphology (Figure 47).

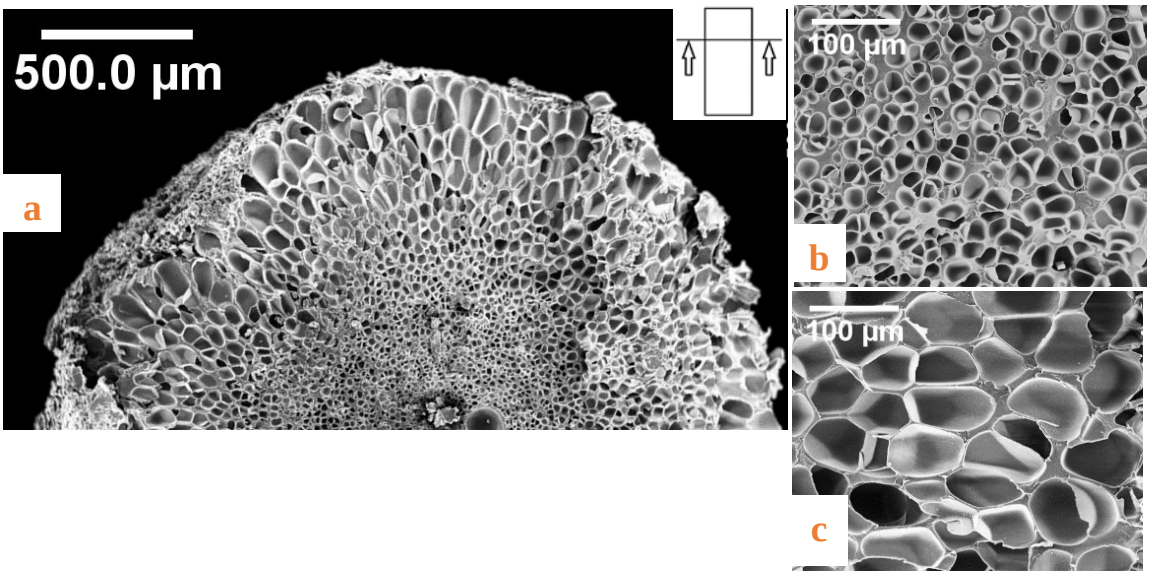

Figure 47.a) Gradient foam of PA-12-PS composite with b) smaller cells in the core leading to c) larger cells in the periphery

The core of the composite has a cell size of around 25 microns which is similar to the cells observed in the neat PA12 filament in Figure 43, whereas the periphery shows much larger cells averaging 80 microns in diameter. The cause for this morphology could be linked to the swelling procedure. Since the filament is cylindrical in shape, the styrene and initiator diffuse radially inward from the surface. If the soak time is shorter than the time required for complete saturation of the filament, incomplete diffusion would occur. Polymerization, hence would lead to a gradient in concentration, with a higher mole fraction of polystyrene at the periphery and a higher mole fraction of PA12 in the core. This is evident from the Fourier transform infra-red spectroscopy studies discussed later. The PET-PS composites, however show a homogenous and isotropic cell morphology as evident from the longitudinal and transverse cross sections in (Figure 48).

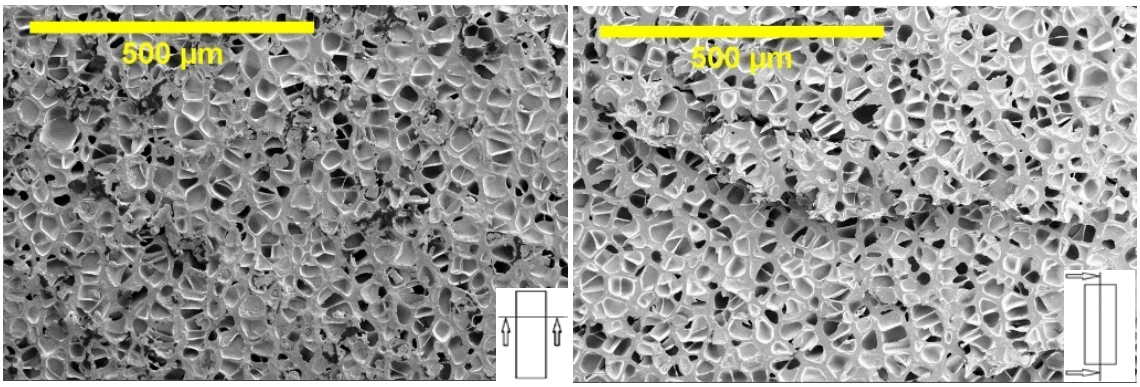

Figure 48. SEM of PET-PS foam, transverse(left) and longitudinal cross sections

Thus, although the expansion of the foam is highly anisotropic, the cell morphology observed is isotropic. Since both the soaking and polymerizing procedure are carried out above the glass transition temperature of PET, leading to a relaxation in a direction perpendicular to the orientation, i.e. in the height direction. The mobility of the polymer chains is high, and the crystallites thus are unable to orient the cells during nucleation and growth. However, the polymer chains are strong enough to maintain the integrity and shape of the final composite.

To study the effect of the procedure on the molecular orientation of the filament, wide angle x-ray scattering (WAXS) was performed on control templates as well as the composites. For the PA12 system, the results are shown in Figure 49. The images observed are typical for oriented systems such as filaments, with high intensity lobes appearing opposite to each other. A Cinader and Burghardt approach was used to calculate an orientation parameter[44], wherein a value of 0 indicates no orientation or perfect isotropy and a value of 1 indicates perfect anisotropy. A value of 0.51 was obtained for the control PA12 filament indicating that the crystal fraction is anisotropic while diffuse halo indicates the presence of an isotropic amorphous fraction.

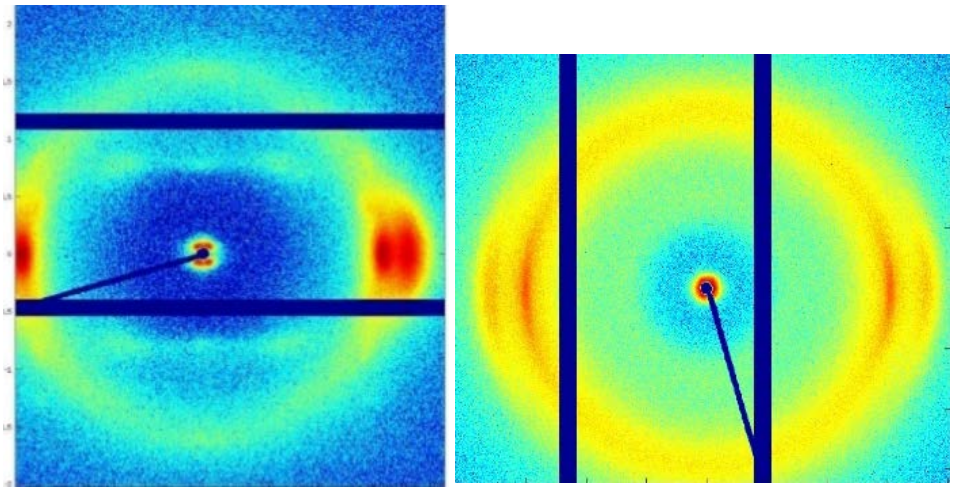

Figure 49. WAXS of a) PA12 filament with high intensity lobes in red, and b) PA12-PS composite the amorphous 'diffuse' component in yellow

An orientation factor of 0.16 was obtained for the composite. A relaxation of oriented polymer chains in the radial direction due to swelling and the presence of amorphous polystyrene led to a more intense amorphous halo and a reduction in the anisotropic elements in the scattering pattern, though some anisotropy is still evident from the higher intensity spots in red.

For the PET film, WAXS was performed on control films both in the transverse and head-on direction (Figure 50). The transverse scan shows orientation a value of 0.36, while normal to the plane of the film gave a value of 0.16 and a four-way symmetry of high intensity spots, which one can expect from a biaxially stretched film. However, scans on the composite show a complete loss of orientation, with an orientation parameter close to 0. In both cases, relaxation in a direction opposite the initial direction of anisotropy leads to a loss of orientation during the composite synthesis process.

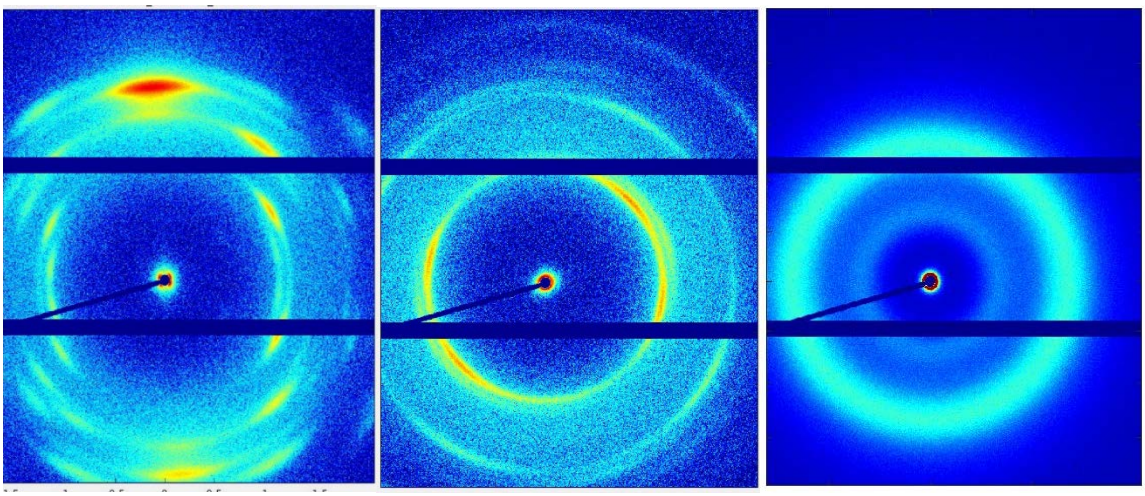

Figure 50. WAXS of PET film a) transverse and b) perpendicular the plane vs c) PET-PS blend

4.4.2. Thermal analysis and Composition

In a DSC analysis, both the blends show a single glass transition temperature in between the two glass transitions of the individual components which is consistent with the facts subsequently discussed. (Figure 51). This suggests molecular level blending leading to the formation of a kinetically trapped blend, with the presence of only one glass transition temperature.

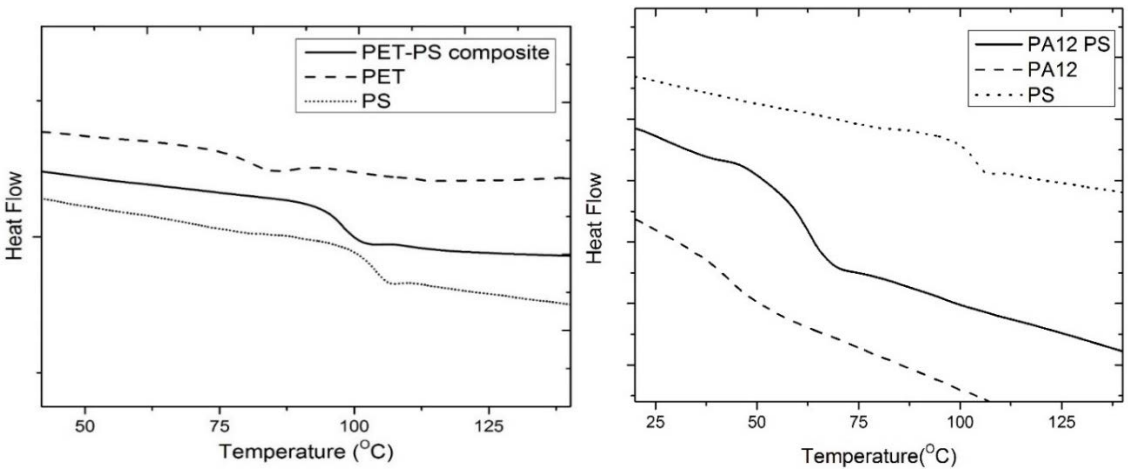

Figure 51. Tg of PET-PS blend(left) and PA12-PS blend

Comparing the first and second cycles of the two blends (Figure 52), we see that on the second heat cycle, the individual glass transition temperature of polystyrene is recovered. If we compare the solubility parameters of the individual components *(Table 6)*

Table 6. Solubility parameters of components

Polymer	$\boldsymbol{Solubility\ Parameter\ \delta\ (MPa^{\frac{1}{2}})}$
Polystyrene (PS)	18.6
Poly ethylene terephthalate (PET)	21.2
Polyamide 12 (PA12)	19

the difference causes the two components in the blend to be in a state of non-equilibrium. Due to the unfavorable interactions between the two components, heating it to an elevated temperature causes the components to phase separate, which leads to the discernable glass transition temperature of polystyrene on the second heating cycle. The relatively small difference in the solubility parameters between PA12 and PS was evidently sufficient to

lead to a phase separation as seen in Figure 52. This indicates that kinetically-trapped blends are synthesized using this process, despite their thermodynamic incompatibility.

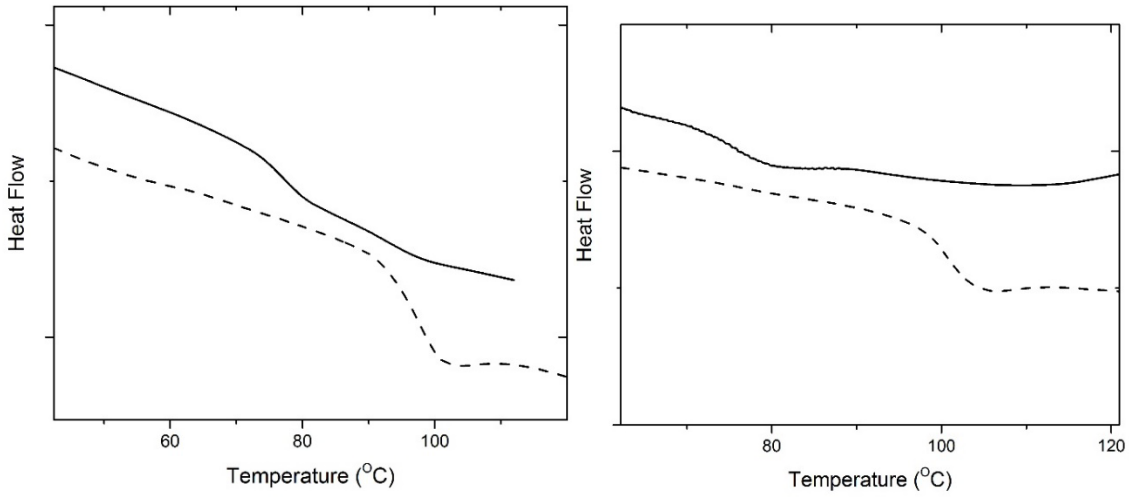

Figure 52. Tg of Polystyrene evident on second heat cycle in PA12-PS (left) and PET-PS blends

The DSC analysis also reveals a drop in the melting enthalpy of the composites. Assuming the crystallites stay intact during the synthesis of blends, we can use the ratio of melting enthalpies to calculate the mass fraction of the individual components in the composite. Calculating the fraction of PA12 to polystyrene in the composite by the ratio of the enthalpy of melting, a PA12 content of 27% w/w was observed (Figure 53).

The mass fraction of PET in the sample was determined using three different techniques, by comparing 1) Melting enthalpies 2) mass uptake and 3) residue values from TGA. The three techniques agreed well with each other, so mass uptake method was subsequently used here for its relative ease. Remarkably, the fraction of PET in the composite in each case was found to be not more than 4% w/w (Table 7). Despite the low concentration of PET in the composite, the film had the ability to template the final macroscopic shape of the composite.

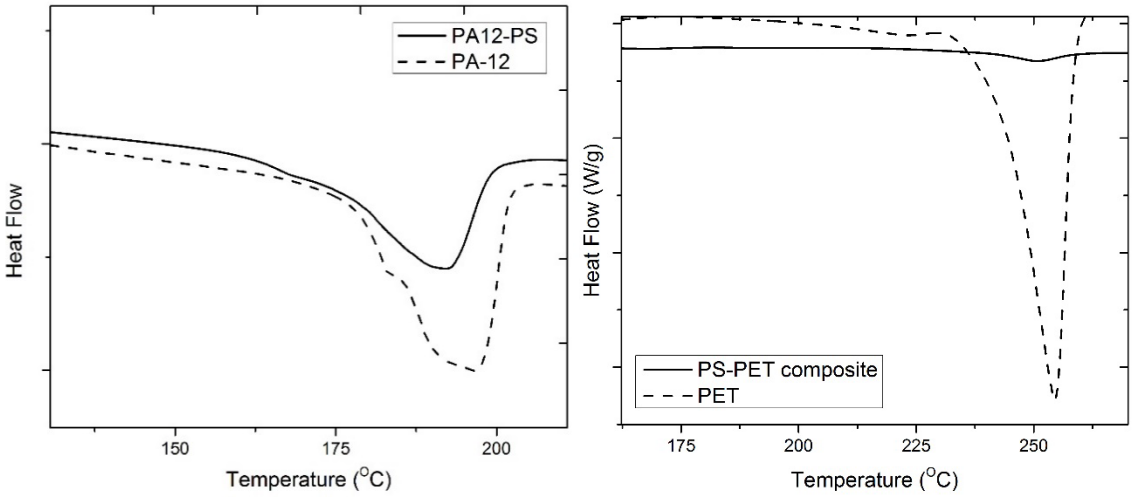

Figure 53. Melting endotherms of PA12-PS (left) and PET-PS blends

Table 7. Composition of PET-PS blends

	Stretch ratios, length/width/height	**wt% PET (mass)**	**wt% PET (DSC)**	**wt% PET (TGA)**
1	1.18/2.40/25	3.12 %	3.24 %	2.61 %
2	1.08/1.77/17.7	3.96 %		
3	0.88/1.83/14.1	2.80 %		

4.4.3. Fourier Transform Infrared Spectroscopy (FTIR)

Reflectance mode was used for the FTIR and specimens for observation were obtained both from the core and the surface of the composite.

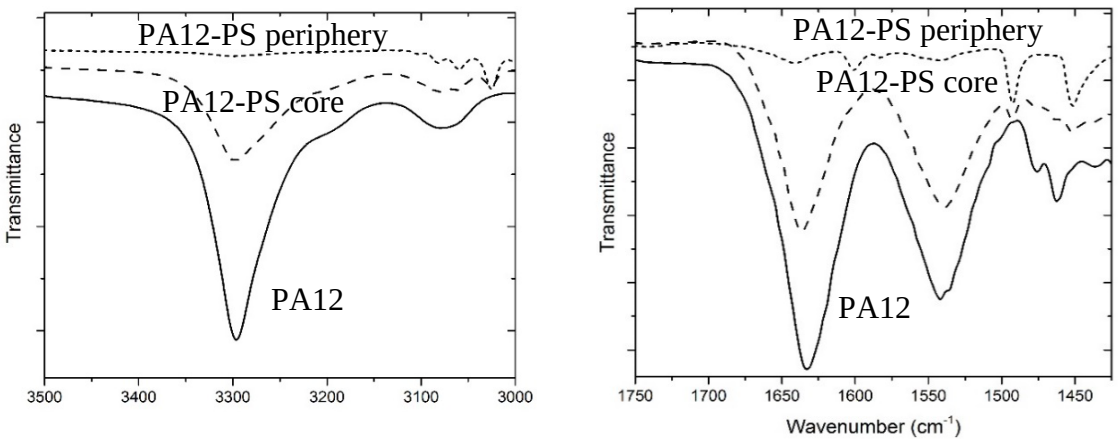

Figure 54. FTIR of PA12-PS composite at the core and periphery

Pure PET film, PA12 filament and polystyrene polymerized from styrene and TBPB in an oven at 100ºC for 24 hours were used as standards for comparison. For the PA12-PS composite, the core showed strong N-H bending and stretch signals at 1530 cm^{-1} and 3300 cm^{-1} respectively, and C=O stretch signal at around 1630 cm^{-1} corresponding to amide groups (Figure 54). The periphery, however showed a much weaker amide presence again suggesting that the gradient cellular structure was formed due to the gradient in concentration of polystyrene from the periphery to the core.

The PET-PS composite foam showed peaks at frequencies of 1734 and 1257 cm^{-1} indicating the presence of the C=O and C-O bonds, respectively, which are also observed in the pure PET film spectrum (Figure 55). Specimens from both the surface and the core showed similar spectra, indicating that the composition was homogenous through the cross section of the sample.

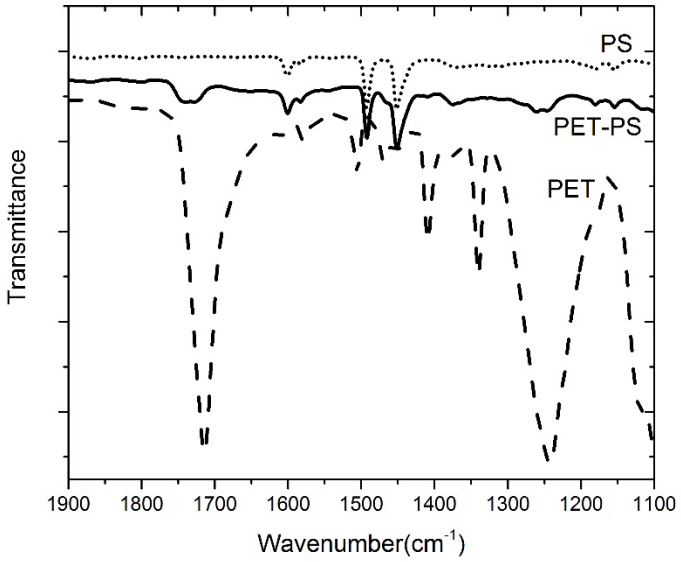

Figure 55. FTIR of PET-PS composite vs PET and PS

4.4.4. Mechanical Testing

The mechanical properties of the PET-PS composites were evaluated using a four-point bend apparatus. This method has the advantage of subjecting the composite to both compression and tension. Also, this method is superior to a three-point bend since the three-point bend setup has a higher stress concentration at the point of loading, which might lead to a premature failure. In a four-point bend setup, the load is uniformly distributed between the two inner loading pins, thus mitigating this premature failure. For the test, the rectangular composite was placed between the two supports such that $b>h$ (Figure 56).

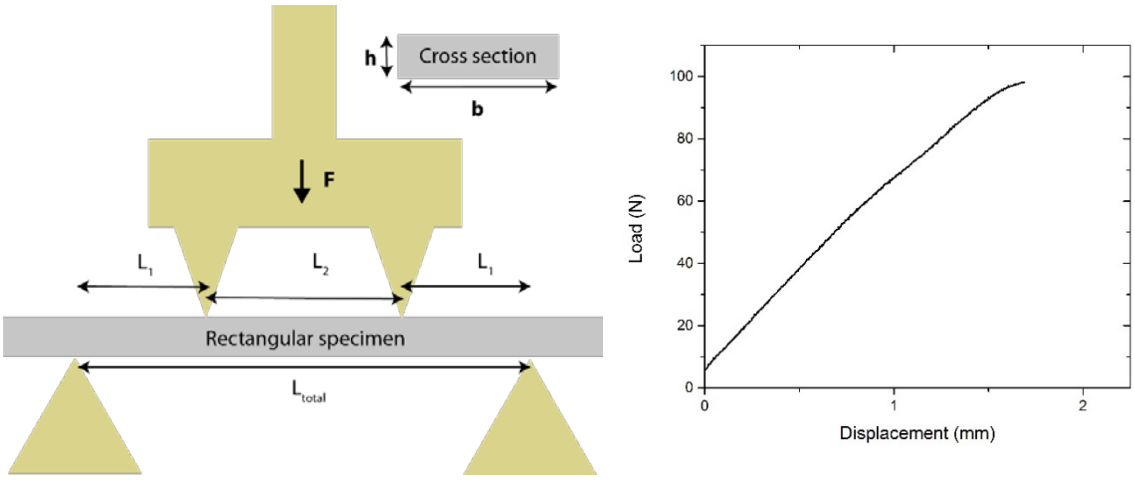

Figure 56. Schematic of four-point bend setup (left) and a typical load displacement curve.

Bending was carried out to failure at a rate of 1mm/minute. The modulus was determined by using the slope of the initial part of the load displacement curve for the value of $\frac{F}{\delta}$ and substituting that value in Equation 3.

$$\left(E = \frac{FL_1(3L_{total}^2 - 4L_1^2)}{24I\delta}\right) \tag{3}$$

Where *I* is the second moment of inertia calculated for a beam by the Equation 4.

$$I = \frac{bh^3}{12} \tag{4}$$

The flexural strength *σ(MPa)* was determined by Equation 5, using the maximum load of the force displacement curve where *M (N-m)* is the moment applied to the composite and *y=h/2*, the distance of the foam core to the surface. The moment increases linearly from the outer supports and becomes a constant value of FL_1 between the upper inner supports.

$$\sigma = \frac{My}{I} \tag{5}$$

The specific strength and the specific modulus was plotted to better gauge the material properties of the system (Figure 57).

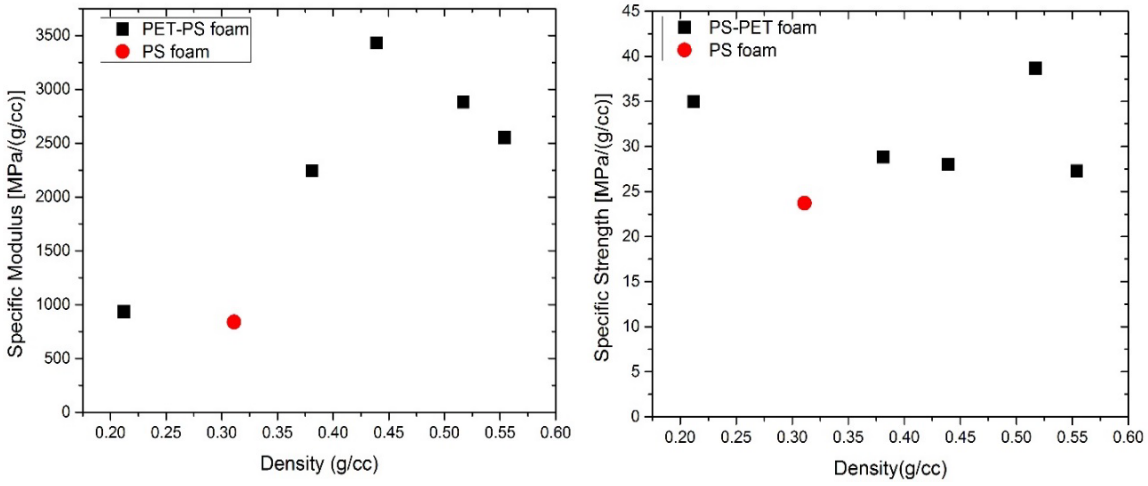

Figure 57. Specific strength and specific modulus of PET-PS composite

The foams were found to fail between the two upper supports where the moment is uniform and maximum. No buckling was observed on the upper surface of the foams indicating that the foams failed in tension in a brittle manner. Both the specific modulus and strength show an improvement, despite the low concentrations of PET in them.

4.4.5. External confinement

Since the change in dimension observed was greatest in the height direction, confinement in this direction could introduce anisotropy into the composite system. Two types of confinement were used as described in Figure 58, Confinement 1 and Confinement 2. In Confinement 1, the PET film was placed between two rectangular strips of aluminum of dimensions approximately 10 by 100mm. The strips were separated by aluminum spacers and the system was tied together by Kevlar® fibers to hold the spacers in place and provide confinement. This setup was then placed in the test tube and the soak-polymerize procedure

was carried out. In Confinement 2, the PET film was confined within the test tube itself using two rigid cylinders to provide a gradient in confinement.

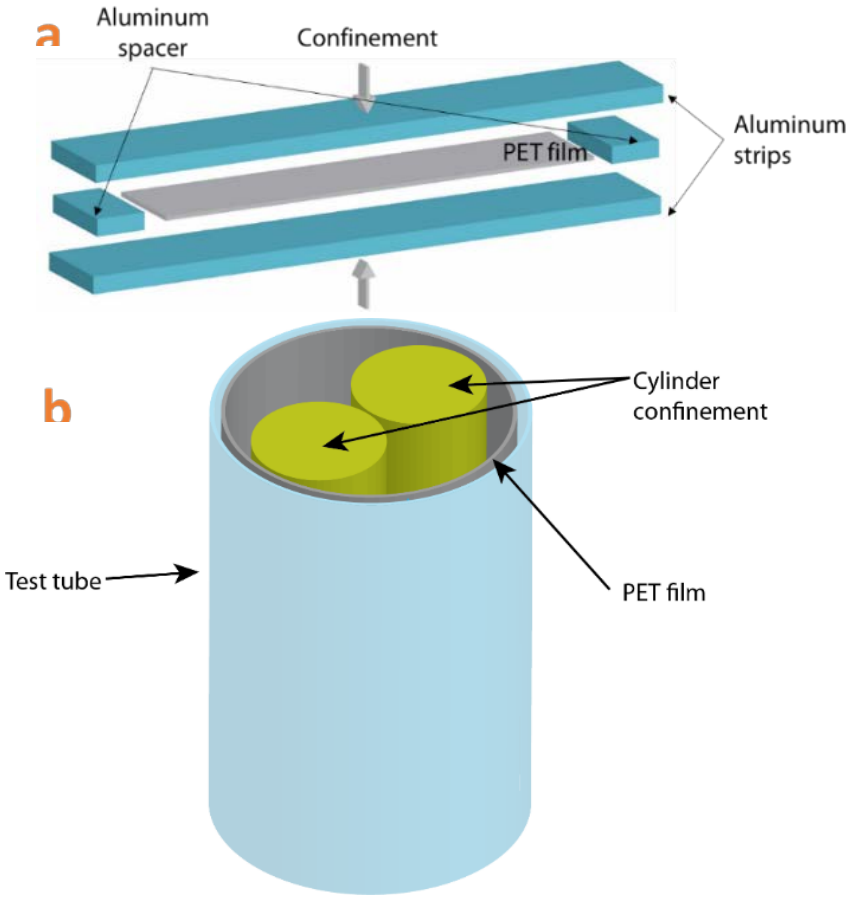

Figure 58. a). Confinement 1 and b). Confinement 2

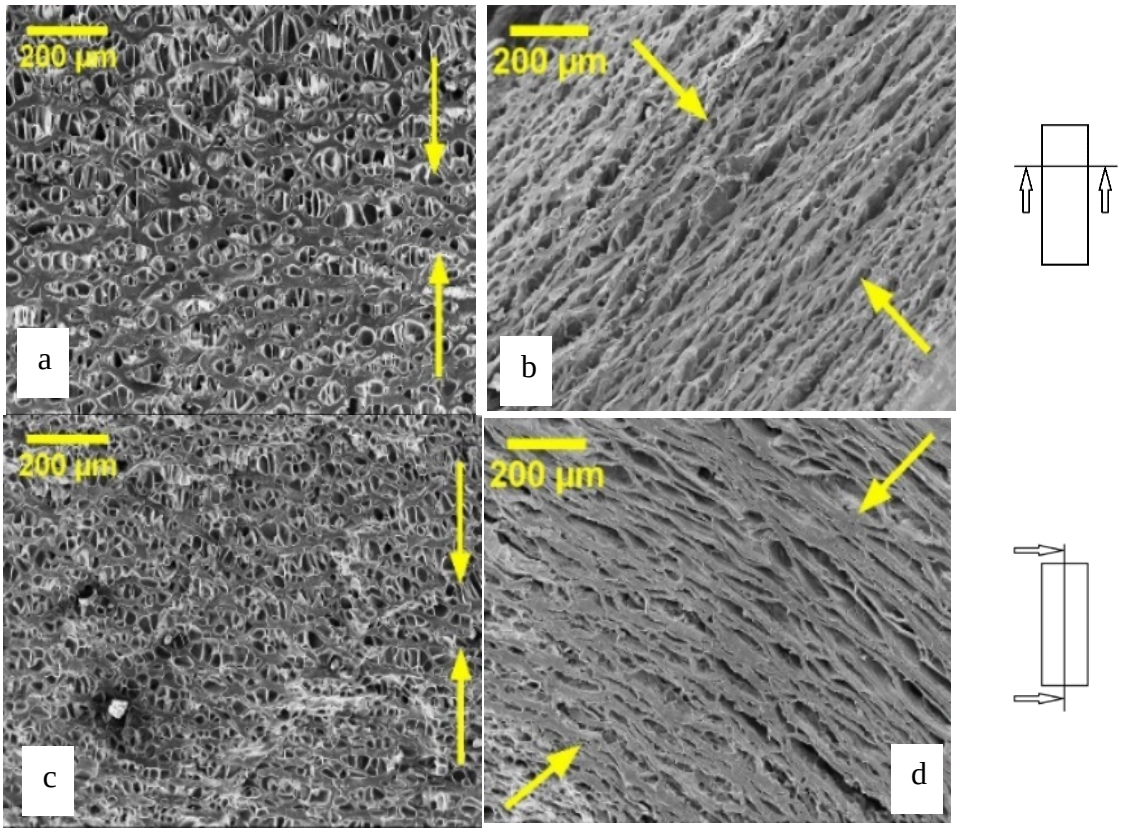

Figure 59. Anisotropic cells due to Confinement 1 (a and c) and Confinement 2 (b and d). Transverse sections (a and b) and longitudinal sections (c and d). Yellow arrows indicate direction of confinement.

These different approaches led to various levels of anisotropy in the layer or sheet like morphologies observed in Figure 59. Figure 59.a and Figure 59.b show the longitudinal and transverse cross sections of the composites subjected to Confinement 1 respectively, whereas Figure 59.c and Figure 59.d show the longitudinal and transverse cross sections of the composites subjected to Confinement 2. The greater level of confinement that was made possible in the second setup led to a much more apparent sheet-like or lamellar morphology of cells as compared to the first setup. This morphology could not only provide interesting anisotropic mechanical properties, but also be used for applications such as unidirectional transport or filtration.

4.5. Alternate Strategies to Synthesize Foams

4.5.1. Foaming Elastomeric Thin Films

In this section $scCO_2$ and environmentally benign solvents were utilized to process foams from elastomeric thin films for applications such as membranes or insulation. The limitations for foaming elastomeric films are twofold. Firstly, foaming thin films is challenging because the process is diffusion dominated. Gas diffuses rapidly out of the film on depressurization, and this occurs before nucleation and growth can occur. Thus, the concentration of gas is too low in the bulk to form a cellular structure. Secondly, since the films are elastomeric, depressurization leads to complete relaxation and collapse of the cell structure at room temperature, since the low modulus of the elastomers at these temperatures fail to lock in the porous structure. The films used for these experiments were styrene-butadiene block co-polymer (SBS), 100 microns in thickness, provided by Rogers Corporation. NMR analysis was performed by dissolving the block copolymer in chloroform. Quantitative analysis of the spectrum revealed a polystyrene fraction of around 16%, shown in Figure 60. A heat-cool-heat cycle was performed on the film at a rate of 10°C/minute. The DSC thermogram reveals a glass transition temperature of around 5°C (Figure 61). TGA shows a two-stage degradation, as can be seen from the first derivative of the weight loss vs temperature (Figure 62). The first stage has been attributed to the degradation of the aliphatic butadiene phase, which has a lower Tg and hence is more penetrable by oxygen[104–106], whereas the styrenic phase degrades at a higher temperature. Foaming the films at a temperature of 70°C and 4000psi for a period of one hour revealed a microcellular structure with homogenous cell size distribution when observed under the

scanning electron microscope. The 16% styrenic fraction could be a contributor to the cells being intact even after the foaming procedure.

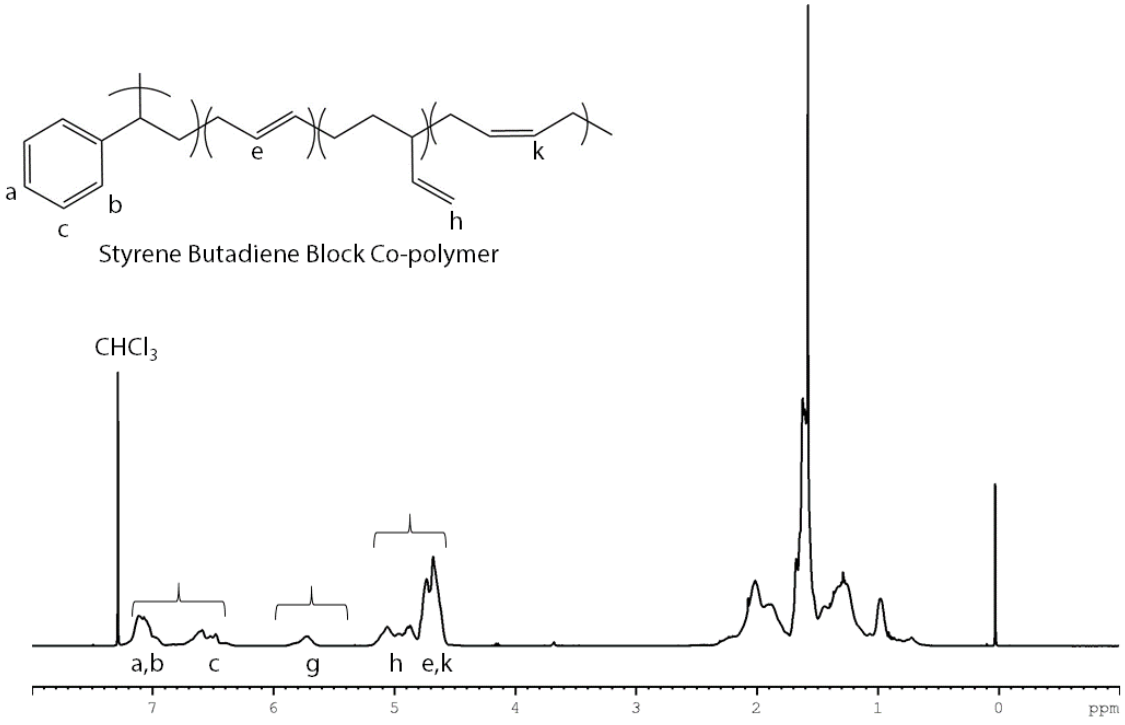

Figure 60. NMR of SBC, showing a styrenic fraction of 16%.

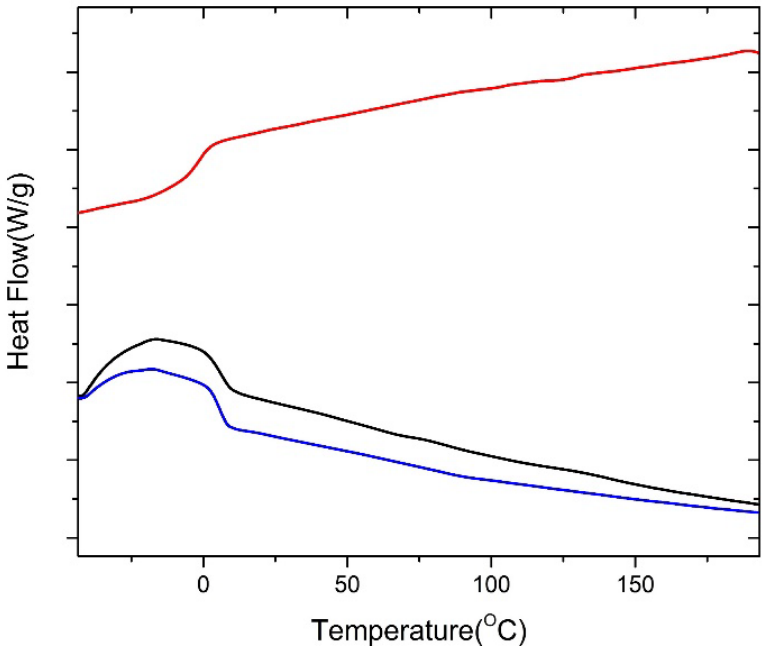

Figure 61. DSC of SBC, (black-first heat cycle, red-first cool cycle, blue-second heat cycle) showing a single glass transition temperature of around 5°C

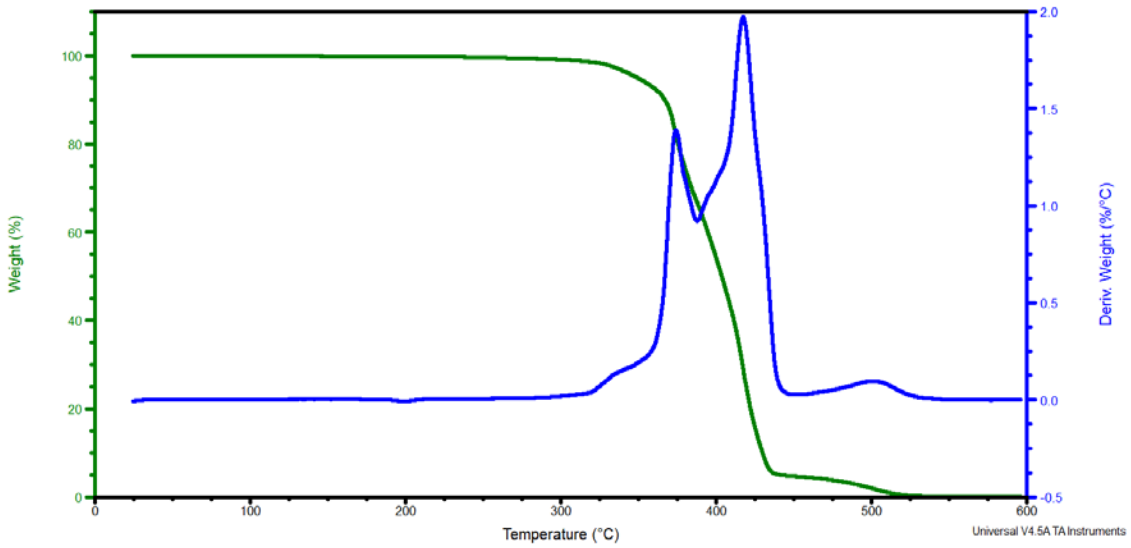

Figure 62. TGA of SBC, showing a two-stage degradation process (blue-derivative of wt% *vs* temp)

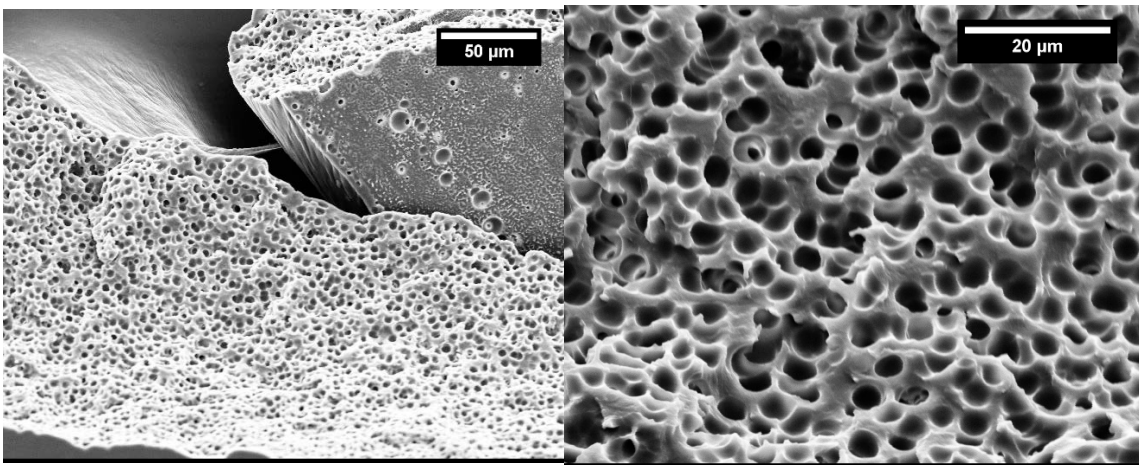

Figure 63. Foaming SBCs with $scCO_2$ showed a microcellular morphology

Using superheated water at elevated temperatures of 120°C led to larger cell sizes, as might be expected with a foaming process at a higher temperature (Figure 64). However, an interesting feature of using superheated water as a processing aid was the presence of surface porosity, that was not obtained otherwise, shown comparatively in Figure 65. Looking more closely, there might be an indication that the surface pores are interconnected, creating an open cell structure that might be useful for its transport properties and filtration.

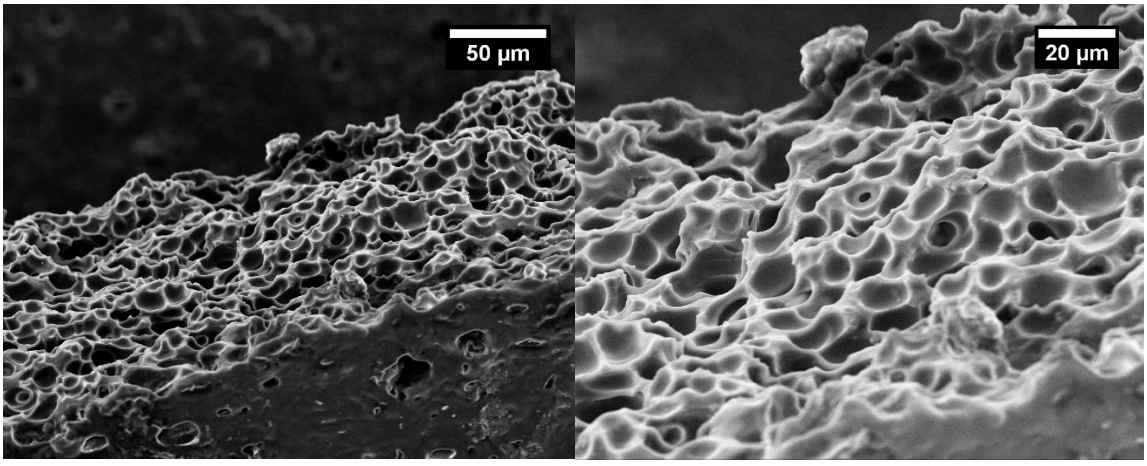

Figure 64. SBCs processed with superheated water showing larger cells than those processed without

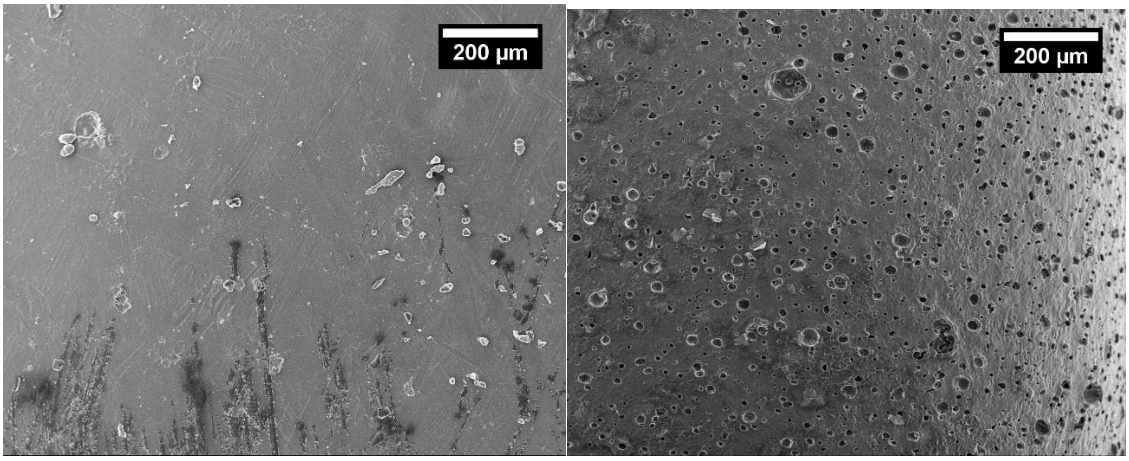

Figure 65. SBC foam processed without superheated water (left) and with superheated water, showing surface porosity.

One can tune the processing parameters and create interesting cell morphologies; for example, a step depressurization procedure can be implemented to create a bimodal distribution of cell morphologies (Figure 66). This could be used for enhanced selectivity in applications such as filtration.

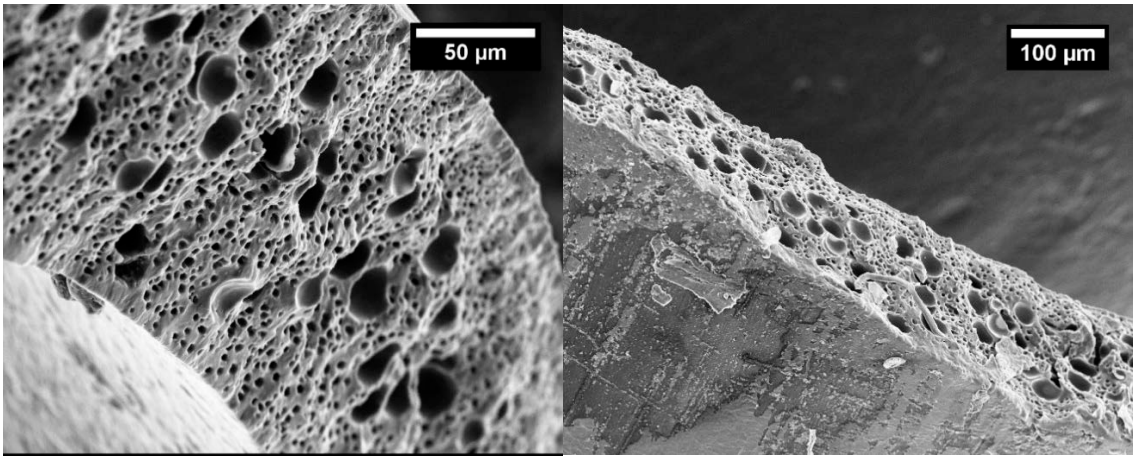

Figure 66. Bimodal cell size distribution

4.6.Conclusions

The effect of molecular anisotropy on foams was studied, to see if anisotropy in the crystalline region can template cell structure. Anisotropic semi-crystalline polymers such as films and filaments were used as templates to create kinetically trapped composite foams. PET films and polyamide filaments were soaked in styrene and subsequently polymerized to create miscible blends with polystyrene that are kinetically trapped, as evidenced by single glass transition temperatures. These were then foamed to create microcellular porous structures. In both the cases, the final shape of the composite foams was templated by the initial shape of the substrate. However, the crystalline anisotropy present in the substrate was lost due to rapid relaxation mechanisms of polymer chains above their glass transition temperatures. In the case of PA12-PS, a radial gradient in cell size was observed, with smaller cells at the core and larger cells at the periphery. In case of the PET-PS composites, the rectangular shape of the PET film is retained despite the low concentration of PET in the composite. The expansion during foaming occurs in a highly anisotropic fashion; the foams expand an order of magnitude more in height than in length and width. Cell structure, however was observed to be isotropic. Anisotropic cells were obtained by limiting the expansion of the foam in the height direction using unusual ways for confinement. Four-point bending tests indicate that the composite foams show improved stiffness and strength.

Foaming of elastomeric thin films using $scCO_2$ and superheated water was achieved, which was unexpected based on conventional knowledge of foaming thin film elastomers. The high polystyrene content may have played a role in maintaining the cell structure after depressurization. We also achieved surface porosity with possible open or interconnected

cell morphologies, with potentially exploitable transport properties. A bimodal cell size distribution was obtained with a step depressurization profile which could help enhance selectivity.

Funding Sources

I am grateful to the following agencies for their funding that made all this work possible:

- The U.S. Army Natick Soldier Research, Development and Engineering Center (NSRDEC)
- Bridgestone of Americas
- BASF Corporation
- Rogers Corporation
- CUMIRP Cluster-M

BIBLIOGRAPHY

1. So, Y.-H. et al. Study of the mechanism for poly(p-phenylene)benzoxazole polymerization. A remarkable reaction pathway to make rigid-rod polymers. Macromolecules 31, 5229–5239 (1998).

2. Kim, Y. J. Synthesis of High Molecular Weight Polybenzoxazoles in Polyphosphoric Acid and Investigation of their Hydrolytic Stability under Acidic Conditions. *High Perform. Polym.* **17,** 377–401 (2005).

3. Choe, E. W. & Kim, S. N. Synthesis, Spinning, and Fiber Mechanical Properties of Poly(p-phenylenebenzobisoxazole). *Macromolecules* **14,** 920–924 (1981).

4. Wolfe, J. F. & Arnold, F. E. Rigid-Rod Polymers. 1. Synthesis and Thermal Properties of Para-Aromatic Polymers with 2,6-Benzobisoxazole Units in the Main Chain. *Macromolecules* **14,** 909–915 (1981).

5. Wolfe, J. F., Loo, B. H. & E, A. F. Rigid-Rod Polymers. 2. Synthesis and Thermal Properties of Para-Aromatic Polymers with 2,6-Benzobisthiazole Units in the Main Chain. *Macromolecules* **14,** 915–920 (1981).

6. Chae, H. G. & Kumar, S. Rigid-rod polymeric fibers. *J. Appl. Polym. Sci.* **100,** 791–802 (2006).

7. Krause, S. J. *et al.* Morphology and properties of rigid-rod poly(p-phenylene benzobisoxazole) (PBO) and stiff-chain poly(2,5(6)-benzoxazole) (ABPBO) fibres. *Polymer (Guildf).* **29,** 1354–1364 (1988).

8. Cohen, Y. & Thomas, E. L. Microfibrillar network of a rigid rod polymer. 1. Visualization by electron microscopy. *Macromolecules* **21,** 433–435 (1988).

9. Cohen, Y. & Thomas, E. L. Microfibrillar network of a rigid rod polymer. 2. Small-angle x-ray scattering. *Macromolecules* **21,** 436–441 (1988).

10. Kitagawa, T., Murase, H. & Yabuki, K. Morphological Study on Poly(p-phenylenebenzobisoxazole) (PBO) Fiber. *J. Polym. Sci. Part B Polym. Phys.* **36,** 39–48 (1998).

11. Herrera-Franco, P. J. & Drzal, L. T. Comparison of methods for the measurement of fibre/matrix adhesion in composites. *Composites* **23,** 2–27 (1992).

12. Colton, J. S. The Nucleation of Microcellular Foams in Semi-Crystalline Thermoplastics. *Mater. Manuf. Process.* **4,** 253–262 (1989).

13. Baldwin, D. F., Park, C. B. & Suh, N. P. A microcellular processing study of poly(ethylene terephthalate) in the amorphous and semicrystalline states. Part I: Microcell nucleation. *Polym. Eng. Sci.* **36,** 1437–1445 (1996).

14. Doroudiani, S., Park, C. B. & Kortschot, M. T. Effect of the crystallinity and morphology on the microcellular foam structure of semicrystalline polymers. *Polym. Eng. Sci.* **36,** 2645–2662 (1996).

15. Evans, G. C. & Lesser, A. J. Polymeric solutions, methods of manufacture thereof and articles manufactured therefrom. (2015).

16. Properties | ZYLON (PBO Fiber) Toyobo. (2005). Available at: http://www.toyobo-global.com/seihin/kc/pbo/zylon_bussei.html. (Accessed: 14th October 2016)

17. Cheng, M., Chen, W. & Weerasooriya, T. Mechanical Properties of Kevlar® KM2 Single Fiber. *J. Eng. Mater. Technol.* **127,** 197 (2005).

18. Roitman, D. & McAdon, M. Persistence length of the 'rodlike' molecule poly (p-phenylene-trans-benzobisthiazole) revisited. *Macromolecules* **26,** 4381–4383 (1993).

19. Roitman, D. B., Wessling, R. A. & McAlister, J. Characterization of poly(p-phenylene-cis-benzobisoxazole) in methanesulfonic acid. *Macromolecules* **26,** 5174–5184 (1993).

20. Zhang, R. & Mattice, W. L. Evaluation of the persistence length of the rigid-rod polymers poly(benzobisoxazole) and poly(benzobisthiazole) using molecular-dynamics simulations. *Macromolecules* **25,** 4937–4941 (1992).

21. Holmes, G. A. *et al.* The effect of environmental and mechanical mechanisms on the performance of soft body armor. *17th Int. Conf. Compos. Mater.* (2009).

22. Holmes, G. A., Rice, K. & Snyder, C. R. Ballistic fibers: A review of the thermal, ultraviolet and hydrolytic stability of the benzoxazole ring structure. *J. Mater. Sci.* **41,** 4105–4116 (2006).

23. Chin, J. *et al.* Temperature and humidity aging of poly(p-phenylene-2,6-benzobisoxazole) fibers: Chemical and physical characterization. *Polym. Degrad. Stab.* **92,** 1234–1246 (2007).

24. Tanner, D., Fitzgerald, J. a & Phillips, B. R. The Kevlar Story -- an Advanced Materials Case Study. *Angew. Chemie Int. Ed.* **28,** 649–654 (1989).

25. Orndoff, E. Development and evaluation of polybenzoxazole fibrous structures. *Tech. Memo. 104814, NASA Tech. Reports* (1995).

26. Jackson, P. F., Morgan, K. J. & Turner, A. M. Studies in Heterocyclic Chemistry. Part IV. Kinetics and Mechanisms for the Hydrolysis of Benzoxazoles. *J. Chem. Soc. Perkin Trans.* **2,** 1582–1587 (1972).

27. Forster, A. L. *et al.* Hydrolytic stability of polybenzobisoxazole and polyterephthalamide body armor. *Polym. Degrad. Stab.* **96,** 247–254 (2011).

28. So, Y.-H., Martin, S. J., Owen, K., Smith, P. B. & Karas, C. L. A study of benzobisoxazole and benzobisthiazole compounds and polymers under hydrolytic conditions. *J. Polym. Sci. Part A Polym. Chem.* **37,** 2637–2643 (1999).

29. Walsh, P. J., Hu, X., Cunniff, P. & Lesser, A. J. Environmental effects on poly-p-phenylenebenzobisoxazole fibers. I. Mechanisms of degradation. *J. Appl. Polym. Sci.* **102,** 3517–3525 (2006).

30. Walsh, P. J., Hu, X., Cunniff, P. & Lesser, A. J. Environmental effects on poly-p-phenylenebenzobisoxazole fibers. II. Attempts at stabilization. *J. Appl. Polym. Sci.* **102,** 3819–3829 (2006).

31. Kitagawa, T. & Yabuki, K. An analysis of capillary water behavior in poly-p-phenylenebenzobisoxazole fiber. *J. Appl. Polym. Sci.* **80,** 1030–1036 (2001).

32. Greenspan, L. Humidity fixed points of binary saturated aqueous solutions. *J. Res. Natl. Bur. Stand. Sect. A Phys. Chem.* **81A,** 89 (1977).

33. Torchia, D. A. *Measurement of Proton-Enhanced C-13 T1 Values By a Method Which Suppresses Artifacts*. *J. Magn. Res.* **30,** (Academic Press, 1978).

34. Masson, J. F. Brief review of the chemistry of polyphosphoric acid (PPA) and bitumen. *Energy and Fuels* **22,** 2637–2640 (2008).

35. Kanbargi, N., Hu, W. & Lesser, A. J. Degradation mechanism of poly(p-phenylene-2,6-benzobisoxazole) fibers by 31P solid-state NMR. *Polym. Degrad. Stab.* **136,** 131–138 (2017).

36. Dobb, M. G., Johnson, D. J. & Saville, B. P. Supramolecular structure of a high-modulus polyaromatic fiber (Kevlar 49). *J. Polym. Sci. Polym. Phys. Ed.* **15,** 2201–2211 (1977).

37. Dobb, M. G., Johnson, D. J. & Saville, B. P. Direct observation of structure in high-modulus aromatic fibers. *J. Polym. Sci. Polym. Symp.* **58,** 237–251 (1977).

38. Li, S. F. Y., McGhie, A. J. & Tang, S. L. Internal structure of Kevlar® fibres by atomic force microscopy. *Polymer (Guildf).* **34,** 4573–4575 (1993).

39. Dobb, M. G., Hindeleh, A. M., Johnson, D. J. & Saville, B. P. Lattice resolution in an electron-beam sensitive polymer. *Nature* **253,** 189–190 (1975).

40. Panar, M. *et al.* Morphology of poly(p-phenylene terephthalamide) fibers. *J. Polym. Sci. Polym. Phys. Ed.* **21,** 1955–1969 (1983).

41. Drzal, L. T., Rich, M. J. & Lloyd, P. F. Adhesion of Graphite Fibers to Epoxy Matrices: I. The Role of Fiber Surface Treatment. *J. Adhes.* **16,** 1–30 (1983).

42. Drzal, L. T., Rich, M. J., Koenig, M. F. & Lloyd, P. F. Adhesion of Graphite Fibers to Epoxy Matrices: II. The Effect of Fiber Finish. *J. Adhes.* **16,** 133–152 (1983).

43. Theocaris, P. *The mesophase concept in composites*. (2012).

44. Hongladarom, K. *et al.* Birefringence, X-ray Scattering, and Neutron Scattering Measurements of Molecular Orientation in Sheared Liquid Crystal Polymer Solutions. *Macromolecules* **29,** 5346–5355 (1996).

45. Benrashid, R. & Tesoro, G. C. Effect of Surface-Limited Reactions on the Properties of Kevlar(R) Fibers. *Text. Res. J.* **60,** 334–344 (1990).

46. Yue, C. Y. Y. & Padmanabhan, K. Interfacial studies on surface modified Kevlar fibre/epoxy matrix composites. *Compos. Part B Eng.* **30,** 205–217 (1999).

47. Takayanagi, M., Ueta, S., Lei, W.-Y. & Koga, K. A New Chemical Method of Surface-Treatment of Kevlar Fiber for Composites with Epoxy Resin. *Polym. J.* **19,** 467–474 (1987).

48. Takayanagi, M., Kajiyama, T. & Katayose, T. Surface-modified kevlar fiber-reinforced polyethylene and ionomer. *J. Appl. Polym. Sci.* **27,** 3903–3917 (1982).

49. Chen, M.-L., Ueta, S. & Takayanagi, M. Improvement of Adhesion of Kevlar Fiber to Poly(methyl methacrylate). *Polym. J.* **20,** 673–677 (1988).

50. Wertheimer, M. R. & Schreiber, H. P. Surface property modification of aromatic polyamides by microwave plasmas. *J. Appl. Polym. Sci.* **26,** 2087–2096 (1981).

51. Wu, G. . M. Oxygen plasma treatment of high performance fibers for composites. *Mater. Chem. Phys.* **85,** 81–87 (2004).

52. Park, J.-M., Kim, D.-S. & Kim, S.-R. Improvement of interfacial adhesion and nondestructive damage evaluation for plasma-treated PBO and Kevlar fibers/epoxy composites using micromechanical techniques and surface wettability. *J. Colloid Interface Sci.* **264,** 431–45 (2003).

53. Lin, J. S. Effect of surface modification by bromination and metalation on Kevlar fibre-epoxy adhesion. *Eur. Polym. J.* **38,** 79–86 (2002).

54. Iyengar, Y. Adhesion of kevlar aramid cords to rubber. *J. Appl. Polym. Sci.* **22,** 801–812 (1978).

55. Kalantar, J. & Drzal, L. T. The bonding mechanism of aramid fibres to epoxy matrices. *J. Mater. Sci.* **25,** 4186–4193 (1990).

56. Kanbargi, N., Lesser, A. J., Zhao, W., Agarwal, S. P. & Rackaitis, M. Methods of Modification of Aramid Fibers. (2017).

57. Deteresa, S. J., Allen, S. R., Farris, R. J. & Porter, R. S. Compressive and torsional behaviour of Kevlar 49 fibre. *J. Mater. Sci.* **19,** 57–72 (1984).

58. Greenwood, J. H. & Rose, P. G. Compressive behaviour of Kevlar 49 fibres and composites. *J. Mater. Sci.* **9,** 1809–1814 (1974).

59. Sinclair, D. A bending method for measurement of the tensile strength and young's modulus of glass fibers. *J. Appl. Phys.* **21,** 380–386 (1950).

60. Drzal, L. & Fukushima, H. Expanded graphite and products produced therefrom. *US Pat. App. 10/659,577* (2003).

61. Northolt, M. G. X-ray diffraction study of poly(p-phenylene terephthalamide) fibres. *Eur. Polym. J.* **10,** 799–804 (1974).

62. Dobb, M. G., Johnson, D. J., Majeed, A. & Saville, B. P. Microvoids in aramid-type fibrous polymers. *Polymer (Guildf).* **20,** 1284–1288 (1979).

63. Fournet, G. & Guinier, A. *Small angle scattering of X-rays*. *eng.uc.edu* (1955).

64. Chaikumpollert, O., Yamamoto, Y., Suchiva, K. & Kawahara, S. Mechanical properties and cross-linking structure of cross-linked natural rubber. *Polym. J.* **44,** 772–777 (2012).

65. Akiba, M. Vulcanization and crosslinking in elastomers. *Prog. Polym. Sci.* **22,** 475–521 (1997).

66. Merker, R. L. & Scott, M. J. The copolymerization of cyclic siloxanes. *J. Polym. Sci.* **43,** 297–310 (1960).

67. Wiley, R. H. Crosslinked styrene/divinylbenzene network systems. *Pure Appl. Chem.* **43,** 57–75 (1975).

68. Qunjie Wang, Huashi Zhang, G. K. Surya Prakash, *, Thieo E. Hogen-Esch, and & Olah*, G. A. Cationic Ring-Opening Polymerization of Cyclosiloxanes Initiated by Electron-Deficient Organosilicon Reagents1a. (1996). doi:10.1021/MA960602W

69. Boileau, S. Ring opening polymerization of cyclic organosilicon compounds: Recent progress. *Makromol. Chemie. Macromol. Symp.* **73,** 177–181 (1993).

70. Eastman, S. A., Lesser, A. J. & McCarthy, T. J. Supercritical CO2-assisted, silicone-modified wood for enhanced fire resistance. *J. Mater. Sci.* **44,** 1275–1282 (2009).

71. Eastman, S. A., Lesser, A. J. & McCarthy, T. J. Bamboo is a suitable template for polymerizations. *J. Appl. Polym. Sci.* **109,** 3961–3967 (2008).

72. Kelly, A. & Tyson, W. R. Tensile properties of fibre-reinforced metals: Copper/tungsten and copper/molybdenum. *J. Mech. Phys. Solids* **13,** 329–350 (1965).

73. Cox, H. L. The elasticity and strength of paper and other fibrous materials. *Br. J. Appl. Phys.* **3,** 72–79 (1952).

74. Lawrence, P. Some theoretical considerations of fibre pull-out from an elastic matrix. *J. Mater. Sci.* **7,** 1–6 (1972).

75. Greszczuk, L. B. in *Interfaces in Composites* 42-42–17 (ASTM International, 1969). doi:10.1520/STP44699S

76. Takaku, a & Arridge, R. G. C. The effect of interfacial radial and shear stress on fibre pull-out in composite materials. *J. Phys. D. Appl. Phys.* **6,** 2038–2047 (2002).

77. Fukuda, H. & Chou, T.-W. An Advanced Shear-Lag Model Applicable to Discontinuous Fiber Composites. *J. Compos. Mater.* **15,** 79–91 (1981).

78. Nairn, J. A. Fracture Mechanics of Unidirectional Composites Using the Shear-Lag Model I: Theory. *J. Compos. Mater.* **22,** 561–588 (1988).

79. Chen, Z. & Yan, W. A shear-lag model with a cohesive fibre–matrix interface for analysis of fibre pull-out. *Mech. Mater.* **91,** 119–135 (2015).

80. Nairn, J. A. On the use of shear-lag methods for analysis of stress transfer in unidirectional composites. *Mech. Mater.* **26,** 63–80 (1997).

81. Kanbargi, N. & Lesser, A. J. A. J. Improving adhesion between aramid fibers and natural rubber through morphological and synthetic modification of the fibers. *J. Appl. Polym. Sci.* 45520 (2017). doi:10.1002/app.45520

82. Gibson, L. J. & Ashby, M. F. *Cellular solids : structure and properties*. (Cambridge University Press, 1997).

83. Da Silva, A. & Kyriakides, S. Compressive response and failure of balsa wood. *Int. J. Solids Struct.* **44,** 8685–8717 (2007).

84. Taki, K., Nitta, K., Kihara, S.-I. & Ohshima, M. CO2 foaming of poly(ethylene glycol)/polystyrene blends: Relationship of the blend morphology, CO2 mass transfer, and cellular structure. *J. Appl. Polym. Sci.* **97,** 1899–1906 (2005).

85. Doroudiani, S., Park, C. B. & Kortschot, M. T. Processing and characterization of microcellular foamed high-density polythylene/isotactic polypropylene blends. *Polym. Eng. Sci.* **38,** 1205–1215 (1998).

86. Siripurapu, S. *et al.* Generation of microcellular foams of PVDF and its blends using supercritical carbon dioxide in a continuous process. *Polymer (Guildf).* **43,** 5511–5520 (2002).

87. Kung, E., Lesser, A. J. & Mccarthy, T. J. Morphology and Mechanical Performance of Polystyrene / Polyethylene Composites Prepared in Supercritical Carbon Dioxide. **9297,** 4160–4169 (1998).

88. Caskey, T. C., Lesser, A. J. & McCarthy, T. J. In situ polymerization and nano-templating phenomenon in Nylon fiber/PMMA composite laminates. *J. Appl. Polym. Sci.* **88,** 1600–1607 (2003).

89. Cooper, A. I. Polymer synthesis and processing using supercritical carbon dioxide. *J. Mater. Chem.* **10,** 207–234 (2000).

90. Cooper, A. I., Hems, W. P. & Holmes, A. B. Synthesis of cross-linked polymer microspheres in supercritical carbon dioxide. *Macromol. Rapid Commun.* **19,** 353–357 (1998).

91. Kendall, J. L., Canelas, D. A., Young, J. L. & DeSimone, J. M. Polymerizations in Supercritical Carbon Dioxide. *Chem. Rev.* **99,** 543–564 (1999).

92. Desimone, J. M., Guan, Z. & Elsbernd, C. S. Synthesis of fluoropolymers in supercritical carbon dioxide. *Science* **257,** 945–7 (1992).

93. Canelas, D. a., Betts, D. E. & DeSimone, J. M. Dispersion Polymerization of Styrene in Supercritical Carbon Dioxide: Importance of Effective Surfactants. *Macromolecules* **29,** 2818–2821 (1996).

94. Jonathan L. Kendall, †, Dorian A. Canelas, †, Jennifer L. Young, and & DeSimone*, J. M. Polymerizations in Supercritical Carbon Dioxide. (1999). doi:10.1021/CR9700336

95. Goel, S. K. & Beckman, E. J. Generation of microcellular polymeric foams using supercritical carbon dioxide. II: Cell growth and skin formation. *Polym. Eng. Sci.* **34,** 1148–1156 (1994).

96. Goel, S. K. & Beckman, E. J. Generation of microcellular polymeric foams using supercritical carbon dioxide. I: Effect of pressure and temperature on nucleation. *Polym. Eng. Sci.* **34,** 1137–1147 (1994).

97. Neavor, K. a., Lesser, A. J. & McCarthy, T. J. Preparation and characterization of microcellular polystyrene foams processed in supercritical CO2. *Am. Chem. Soc. Polym. Prepr. Div. Polym. Chem.* **38,** 446–447 (1997).

98. Gogolewski, S., Czerntawska, K. & Gastorek, M. Effect of annealing on thermal properties and crystalline structure of polyamides. Nylon 12 (polylaurolactam). *Colloid Polym. Sci.* **258,** 1130–1136 (1980).

99. Akzo Nobel. Initiators for high polymers.

100. Sheppard, C. S. & Kamath, V. R. The selection and use of free radical initiators. *Polym. Eng. Sci.* **19,** 597–606 (1979).

101. Chiou, J. S., Barlow, J. W. & Paul, D. R. Plasticization of glassy polymers by CO2. *J. Appl. Polym. Sci.* **30,** 2633–2642 (1985).

102. Ramesh, N. S., Rasmussen, D. H. & Campbell, G. A. Numerical and experimental studies of bubble growth during the microcellular foaming process. *Polym. Eng. Sci.* **31,** 1657–1664 (1991).

103. Neavor, K. A., Lesser, A. J. & McCarthy, T. J. Preparation and characterization of microcellular polystyrene foams processed in supercritical CO2. *Am. Chem. Soc. Polym. Prepr. Div. Polym. Chem.* **38,** 446–447 (1997).

104. Allen, N. S. *et al.* Degradation and stabilisation of styrene–ethylene–butadiene–styrene (SEBS) block copolymer. *Polym. Degrad. Stab.* **71,** 113–122 (2000).

105. Zhang, J., Li, L., Boonkerd, K., Zhang, Z. & Kim, J. K. Formation of bio-based elastomer from styrene-butadiene copolymer and epoxidized soybean oil. *J. Polym. Res.* **21,** 404 (2014).

106. Lu, L., Zhou, Z., Zhang, Y., Wang, S. & Zhang, Y. Reinforcement of styrene-butadiene-styrene tri-block copolymer by multi-walled carbon nanotubes via melt mixing. *Carbon N. Y.* **45,** 2621–2627 (2007).